FINAL REPORT

Fate and Transport of Colloidal Energetic Residues

SERDP Project ER-1689

JULY 2015

Mark E. Fuller
CB&I Federal Services

SERDP
DOD ▪ EPA ▪ DOE

REPORT DOCUMENTATION PAGE

Form Approved
OMB No. 0704-0188

1. REPORT DATE *(DD-MM-YYYY)*	2. REPORT TYPE	3. DATES COVERED *(From - To)*
07/01/2015	Technical	May 2009 - June 2015

4. TITLE AND SUBTITLE
Fate and Transport of Colloidal Energetic Residues

5a. CONTRACT NUMBER
W912HQ-09-C-0012

5b. GRANT NUMBER

5c. PROGRAM ELEMENT NUMBER

6. AUTHOR(S)
Fuller, Mark E.

5d. PROJECT NUMBER
ER-1689

5e. TASK NUMBER

5f. WORK UNIT NUMBER

7. PERFORMING ORGANIZATION NAME(S) AND ADDRESS(ES)
CB&I Federal Services
17 Princess Road
Lawrenceville, NJ 08648

8. PERFORMING ORGANIZATION REPORT NUMBER
ER-1689

9. SPONSORING/MONITORING AGENCY NAME(S) AND ADDRESS(ES)
Strategic Environmental Research and Development Program
4800 Mark Center Drive, Suite 17D08
Alexandria, VA 22350-3605

10. SPONSOR/MONITOR'S ACRONYM(S)
SERDP

11. SPONSOR/MONITOR'S REPORT NUMBER(S)

12. DISTRIBUTION/AVAILABILITY STATEMENT
Approved for public release; distribution is unlimited.

13. SUPPLEMENTARY NOTES

14. ABSTRACT
The key objectives of this project are to (1) assess the formation of these small-sized MC residues during controlled detonations and during weathering of larger residue particles and (2) measure and model the transport (infiltration and surface runoff) and dissolution of these particles.

15. SUBJECT TERMS

16. SECURITY CLASSIFICATION OF:			17. LIMITATION OF ABSTRACT	18. NUMBER OF PAGES	19a. NAME OF RESPONSIBLE PERSON
a. REPORT	b. ABSTRACT	c. THIS PAGE		111	Mark E. Fuller
					19b. TELEPHONE NUMBER *(Include area code)* 609-895-5348

TABLE OF CONTENTS

LIST OF TABLES

LIST OF FIGURES

ACRONYM LIST

ARW	artificial rainwater
°C	degree Celsius
cm	centimeter
d	day
DNX	hexahydro-1,3-dinitroso-5-nitro-1,3,5-triazine
DoD	Department of Defence
EPA	Environmental Protection Agency
ESTCP	Environmental Security Technology Certification Program
ft	foot or feet
g	gram
g	gravity
GMF	glass microfiber
h	hour
HDPE	high density polyethylene
HMX	octahydro-1,3,5,7-tetranitro-1,3,5,7-tetrazocine
HPLC	high performance liquid chromatography
k	kilo
L	liter
µ	micro
m	milli or meter
M	molar
MC	munitions constituent
min	minute
mL	milliliter
mm	millimeter
MNX	hexahydro-1-nitroso-3,5-dinitro-1,3,5-triazine
mol	mole
mV	millivolt
n	nano
NAVAIR	Naval Air Warfare Weapons Division, China Lake, CA
NSWC	Naval Surface Warfare Center
NXs	combined nitroso metabolites of RDX
ORP	oxidation-reduction potential
PDA	photodiode array
PV	pore volume
RDX	hexahydro-1,3,5-trinitro-1,3,5-triazine
rpm	revolutions per minute
SERDP	Strategic Environmental Research and Development Program
SPE	solid phase extraction
TFA	trifluoroacetic acid

TNX	hexahydro-1,3,5-trinitroso-1,3,5-triazine
TOC	total organic carbon
UV	ultraviolet
wt	weight

ACKNOWLEDGEMENTS

This SERDP Project was a collaborative effort among Dr. Yan Jin at the University of Delaware, Dr. Steve Fallis at the Naval Air Warfare Center Weapons Division, China Lake and Dr. Charles E. Schaefer and Dr Mark E. Fuller of CB&I Federal Services, LLC. We wish to acknowledge all of the collaborators for their significant contributions to the success of this research project.

We extend our thanks Dr. Susan Taylor, U.S. Army Corps of Engineers Engineer Research and Development Center/ColdRegions Research and Engineering Laboratory, for supplying detonation residues for some of the expleriments performed.

We wish to acknowledge Dr. Volha Lazouskaya. Dr. Chao Wang, Christina Andaya, and Stan Whitehead for their important technical contributions to this project.

We gratefully acknowledge SERDP for their financial support, and Dr. Andrea Leeson, the Environmental Restoration Program Manager at SERDP, for her guidance. Finally, we wish to acknowledge the DoD facilities and program managers that provided site access and samples for the research conducted herein.

SF296

REPORT DOCUMENTATION PAGE	Form Approved OMB No. 0704-0188

PLEASE DO NOT RETURN YOUR FORM TO THE ABOVE ORGANIZATION.

1. REPORT DATE (DD-MM-YYYY)	2. REPORT TYPE	3. DATES COVERED (From - To)
07-15-2015	Final	May 2008 - July 2015

4. TITLE AND SUBTITLE
Fate and Transport of Colloidal Energetic Residues

5a. CONTRACT NUMBER
W912HQ-09-C-0012

5b. GRANT NUMBER
NA

5c. PROGRAM ELEMENT NUMBER
NA

6. AUTHOR(S)
Fuller, Mark E., Ph.D.

5d. PROJECT NUMBER
ER-1689

5e. TASK NUMBER
NA

5f. WORK UNIT NUMBER
NA

7. PERFORMING ORGANIZATION NAME(S) AND ADDRESS(ES)
CB&I Federal Services. LLC
17 Princess Road
Lawrenceville, NJ 08648

8. PERFORMING ORGANIZATION REPORT NUMBER
NA

9. SPONSORING/MONITORING AGENCY NAME(S) AND ADDRESS(ES)
Strategic Environmental Research and Development Program
4800 Mark Center Drive, Suite 17D08
Alexandria, VA 22350-3600

10. SPONSOR/MONITOR'S ACRONYM(S)
SERDP

11. SPONSOR/MONITOR'S REPORT NUMBER(S)
NA

12. DISTRIBUTION/AVAILABILITY STATEMENT
Distribution Statement A: Approved for Public Release, Distribution is Unlimited

13. SUPPLEMENTARY NOTES
None

14. ABSTRACT

The primary goal of this SERDP project was to evaluate the production and fate of microscale energetic particles. Composition B was used as the model energetic material for the majority of this research. Microscale particulates were observed to be produced during weathering of cm-sized chunks of Composition B under realistic simulated precipitation, with a large release of particles with the first flush of water, followed by a slowly declining production rate as time increased. The mass flux of explosives eluting from microscale Composition B particles during dissolution was similar to that of macroscale particles when values were normalized by surface area. Dissolution of microscale particles was directly visualized and modeled using a newly discovered autofluorescence property of explosive compounds. Microscale particulates transported vertically into porous media by artificial precipitation more than mm-sized residues, thereby increasing their effective contact time with percolating water and increasing the flux of dissolved explosives in the pore water. Horizontal transport of explosives was also detected in surface runoff at an active DoD facility.

15. SUBJECT TERMS
TNT, 2.4.6-trinitrotoluene, RDX, hexahydro-1,3,5-trinitro-1,3,5-triazine, Composition B, explosive, dissolution, transport, microscale, colloid, residue, range, weathering, fate, surface runoff

16. SECURITY CLASSIFICATION OF:			17. LIMITATION OF ABSTRACT	18. NUMBER OF PAGES	19a. NAME OF RESPONSIBLE PERSON
a. REPORT	b. ABSTRACT	c. THIS PAGE			Dr. Mark E. Fuller
U	U	U	UU	100	19b. TELEPHONE NUMBER (Include area code) 609-895-5348

Reset

Standard Form 298 (Rev. 8/98)
Prescribed by ANSI Std. Z39.18

ABSTRACT

Objectives: The key objective of this project was to assess the formation of microscale munition constituents (MC) residues during detonations and weathering of larger detonation residues, and to determine the dissolution and transport properties of these microscale residues as they relate to their fate on testing and trainig ranges.

Technical Approach: The objectives of the project were achieved by a variety of laboratory experiments and some limited field sampling. Composition B (Comp B) was used as the model MC for this research, given its widespread use and that it contains the widely detected explosive compounds TNT and RDX (and HMX present as a co-product from RDX manufacture). Residues from controlled detonations of Comp B (both standard and tagged) were collected and characterized, with special attention given to the size distribution of microscale particles <250 μm. The dissolution of Comp B residues ranging in size from 20 μm to 1 mm to was examined in batch experiments under continous flow conditions, and dissolution of microscale Comp B was also visualized using spectral confocal microscopy using glass micromodels. Compbined transport and dissolution experiments with mm-sized and microscale residues was examined in vertical sand columns under unsaturated flow conditions. The production of microscale particulates from cm-sized Comp B chunks under realistic simulated precipitation was evaluated. Surface runoff was collected over a 1.5 years from an east coast DoD facility and analyzed for dissolved and particulate explosives.

Results:

Glass micromodel experiments. This work discovered that TNT, RDX, and HMX autofluoresce under 405 nm laser illumination, and utilized this property to visualize and quantify the dissolution of microscale Comp B residues in saturated glass bead micromodels. The results demonstrated that within a given Comp B particles, TNT dissolved preferentially over RDX/HMX, and the mass ratio of RDX/HMX to TNT initially increased by >5.3 times. The particles dissolved in a stepwise fashion, with >72% of particle volume reduction in <36 min. Moreover, the results suggested that the particle shape factor was relatively stable, and the particles retained their highly irregular shape throughout the dissolution processes. This is the first work to demonstrate application of spectral confocal microscopy for visualizing and quantifying the behavior of energetic residues at the pore-scale.

Batch dissolution experiments. The dissolution of microscale Comp B particles (<250 μm) was compared to dissolution from macroscopic particles (>0.5 mm), and dissolution of detonation soot was also examined. The measured mass transfer coefficients for the microscale particles were one to two orders of magnitude greater than the macroscopic particles. When normalized to particle surface area, mass transfer coefficients of microscale and macroscale particles were similar, indicating that the bulk dissolution processes were similar throughout the examined size

range. However, an inverse relationship was observed between the particle diameter and the RDX:TNT mass transfer rate coefficient ratio for dry-attritted particles, which suggests that RDX may be more readily dissolved (relative to TNT) in microscale particles compared to macroscale particles. Aqueous weathering of larger Composition B residues generated particles that possessed mass transfer coefficients that were on the order of 5- to 20-fold higher than dry-attritted particles of all sizes, even when normalized to particle surface area. These aqueous weathered particles also possessed a four-fold lower absolute zeta-potential than dry-attritted particles, which is indicative that they were less hydrophobic (and hence, more wettable) than dry-attritted particles. The increased wettability of these particles provides a plausible explanation for the observed enhanced dissolution.

Unsaturated sand column experiments. Under a continuous application of artificial rainwater, greater dissolved effluent concentrations of TNT and RDX (5- and 10-fold, respectively) were observed for sand columns amended with microscale residues than for the columns amended with the mm-sized residues. The increased dissolution could not be completely explained by simple mass transfer differences based on particle size. Elution of particulate Comp B from the columns, based on the difference between total and dissolved explosives concentrations in column effluent, indicated higher and more frequent detections of particulate explosives in the columns amended with microscale Comp B than the columns amended with mm-sized Comp B. Examination of the vertical profiles of explosives in sand indicated that particulate residues had migrated into the sand, with a greater particulate mass observed in the columns which had received the microscale Comp B compared to those which received the mm-sized Comp B. This particulate transport increases the effective contact time between residues and infiltrating rainwater, leading to overall increases in the dissolved mass contaminant flux.

Residue aging experiments. Initial experiments, in which artificial rainwater was applied drip-wise to single chunks of Composition B detonation residues from multiple heights, confirmed that microscale particles were produced during precipitation-driven aging, with 30% of the explosive mass collected detected as particulate Composition B (e.g., particles >0.45 μm in diameter). Follow-on experiments, during which multiple cm-sized residue chunks were subjected to realistic simulated precipitation, demonstrated an initial large pulse of particulate Composition B, followed by sustained production of microscale particles that represented 15% to 20% of recovered explosives.

Field surface runoff sampling. Surface runoff sampling was performed at the active explosives testing area of an east coast DoD facility. Sampling over the course of 1.5 years detected low concentrations of dissolved perchlorate, RDX, and HMX, but no confirmed detections of particulate explosives. Sporadic detections of the RDX breakdown products MNX and TNX were also observed. No clear temporal correlation between range activities and the occurance of the target compounds was detected.

Benefits: This research has provide data that can be used to allow the mass loading of explosive residues at active training ranges to be more accurately estimated, as the impact of microscale MC migration and dissolution was quantified. Preliminary survey data of surface runoff from an active explosive testing area has also indicated that more research into this pathway of explosive compound migration would aid in refining site specific fate and transport models used for range management.

1.0 PROJECT BACKGROUND and OBJECTIVES

DoD Significance

The SERDP Statement of Need ERSON-09-04 stated the need for improved understanding of munition constituent (MC) transport at live fire ranges. Additionally, a 2007 report from the "SERDP and ESTCP Technical Exchange Meeting on DoD Operational Range Assessment and Management Approaches" (47) cited the importance of understanding the fate and transport properties of particulate (vs. soluble) MC, as well as the fate and transport of munition-relevant MC mixtures (i.e., intact Comp B vs. pure RDX or TNT).

Despite the importance of these colloid processes in the fate and transport of energetic compounds, qualitative and quantitative understanding of the fundamental mechanisms associated with MC colloid processes is limited, thereby limiting the ability to accurately describe and predict the global fate and transport of MCs at operational ranges.

This project addressed these need by providing fundamental information on the transport and fate of colloid-sized (or "microscale') munition constituents. This size fraction of residues had not been studied in any detail, yet it represents the most mobile and most rapidly dissolving portions of residual MC generated on operation ranges during live fire training activities. This research addressed several fundamental questions, including:

1) What is the nature of microscale MC particles?
2) What are the mechanisms controlling MC colloid migration into soils?
3) How are MC colloids transported during surface run-off events?
4) How does microscale MC contribute to overall energetic compound dissolution?
5) What is the overall impact of miscroscale MC on ground and surface water quality?

Background

A significant amount of information has been collected regarding the types and amounts of residual munitions constituents (MCs) generated from different live fire training exercises at operation ranges. It has become clear that the most frequent source of MCs on ranges result from low-order detonations of mortars, bombs, and rockets, as well as disposal and blow-in-place UXO operations (47). However, some SERDP-funded studies demonstrated a significant amount of explosive residues are generated even when munitions perform as expected and detonate high-order.

For instance, Taylor et al. found that up to 2% of the initial mass of TNT in a 155-mm round (=135 g) remained after a higher-order detonation (50). Most of this material was <1 mm in size, and particles <53 μm (the smallest sieve size used in the study) were detected. Size fraction

analysis for detonations of munitions containing Composition B have also been performed, although the lower cut-off for characterization of particle size distribution was <250 µm (49). Taylor et al. (2006) also noted that the larger particles of TNT (generated by both high-order and low-order detonations) are friable and give rise to small sized fractions. SEM photographs taken by Phelan et al. (2003) (38) showed that colloidal-sized (~2 µm) Composition B particles are present on larger-sized particles (Figure 1-1), which (as proposed by Taylor et al. (2006)) may have resulted in initially high dissolution rates. Another recent report indicated that munition detonations produced sub-micron soot, and postulated that explosive compounds may be associated with these particles as well (36).

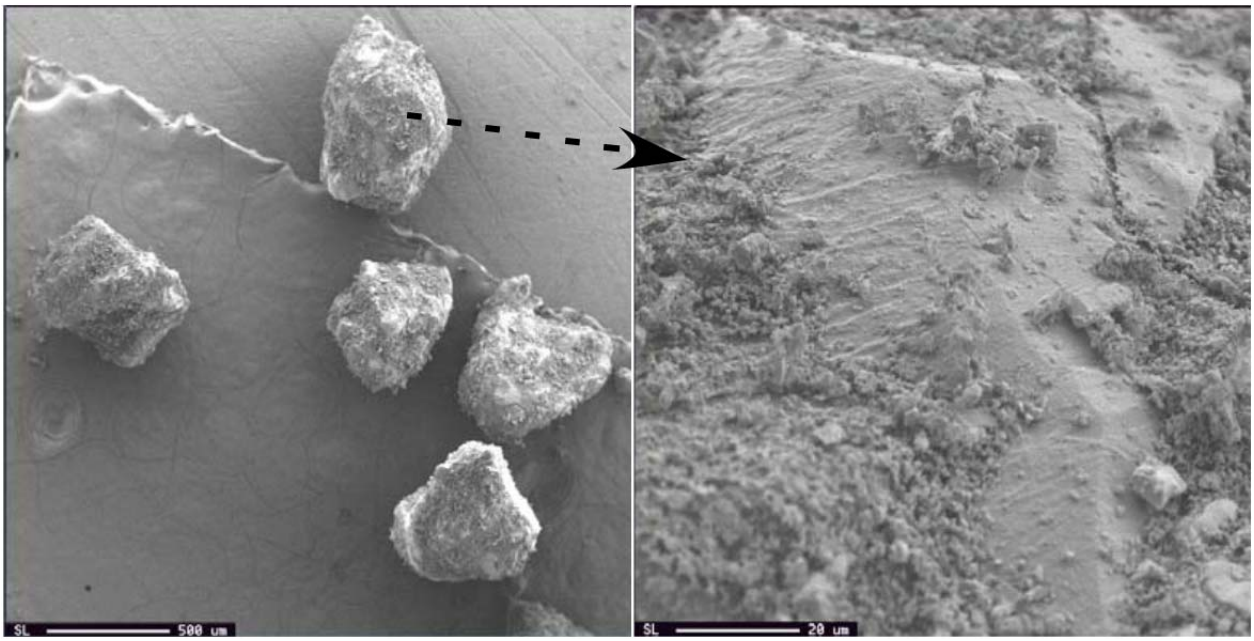

Figure 1-1. SEM Photograph of 500 to 600 µm size fraction of attrited Composition B (from ref (38)). Bar is 20 µm in right photograph and 500 µm in left photograph.

Preliminary experiments conducted before this project began, in which accelerated "aging" of Composition B residues from a 155-mm round was performed by mixing larger particles in water. After 24 h, the solution remained cloudy even several hours after mixing was stopped (Figure 1-2). Microscopic inspection of the solution revealed micron-sized particles, and aggregates of various size particles were observed microscopically (Figure 1-3). These results, coupled with those presented in the previous paragraph, indicate that colloid-sized MC particles are likely derived from both high- and low-order detonations, as well as by natural weathering process. In addition, subsequent detonations of munitions near existing MC on operational

ranges likely result in the generation of smaller and smaller MC, eventually reaching colloid sizes.

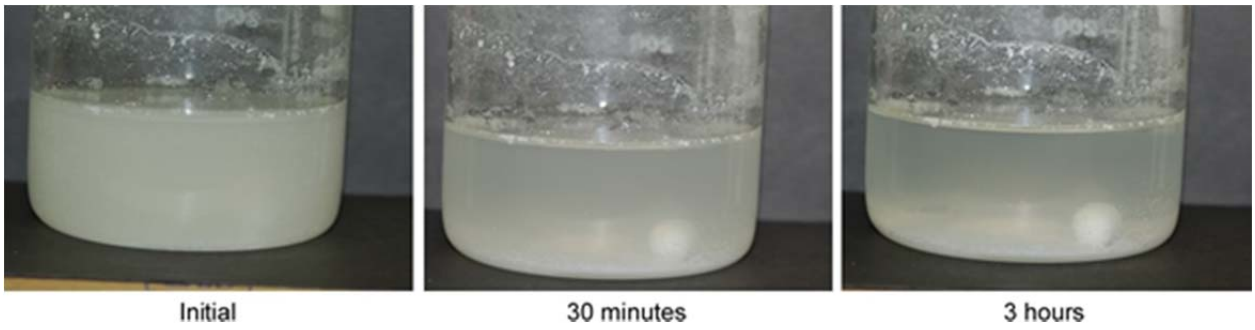

Figure 1-2. Photographs of suspended colloidal Composition B in water after 30 minutes and 3 hours of settling time.

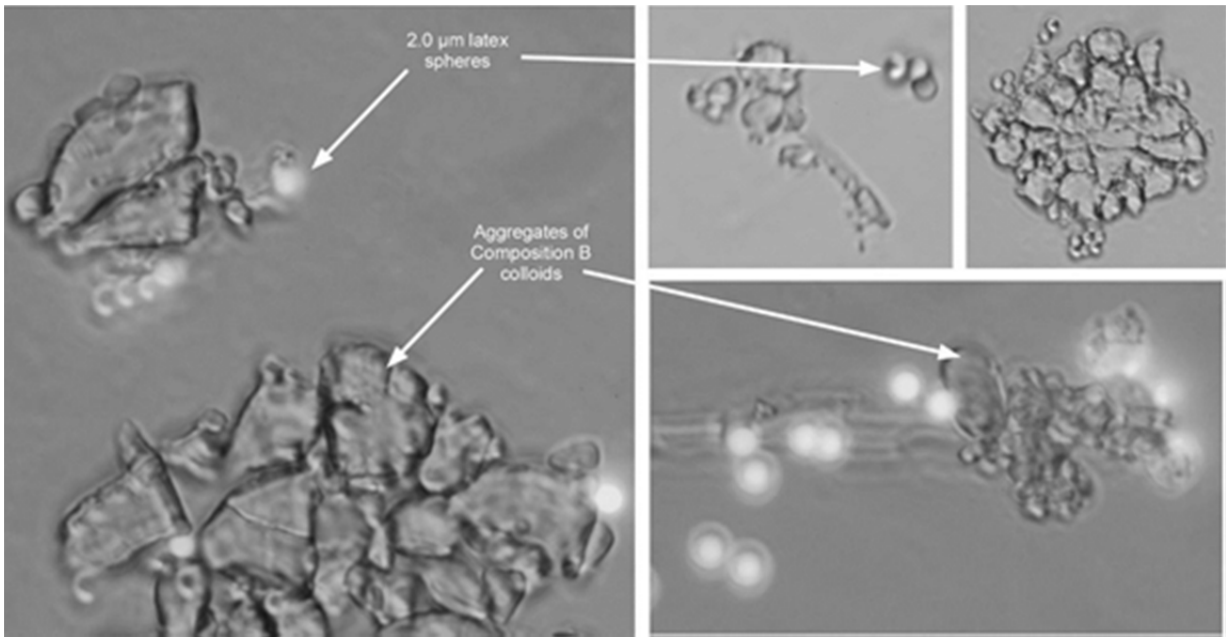

Figure 1-3. Photomicrographs of colloidal Composition B in water. Spherical particles are 2.0 µm fluorescent latex beads.

Colloidal Transport of MCs

Once the residues reach the size range of colloids (<1 micron to a few 10's of microns), they can be transported vertically through the vadose zone with infiltrating precipitation, as well as by

overland flow via surface runoff. A conceptual model incorporating the generation, transport, and dissolution of colloidal MC is presented in Figure 1-4.

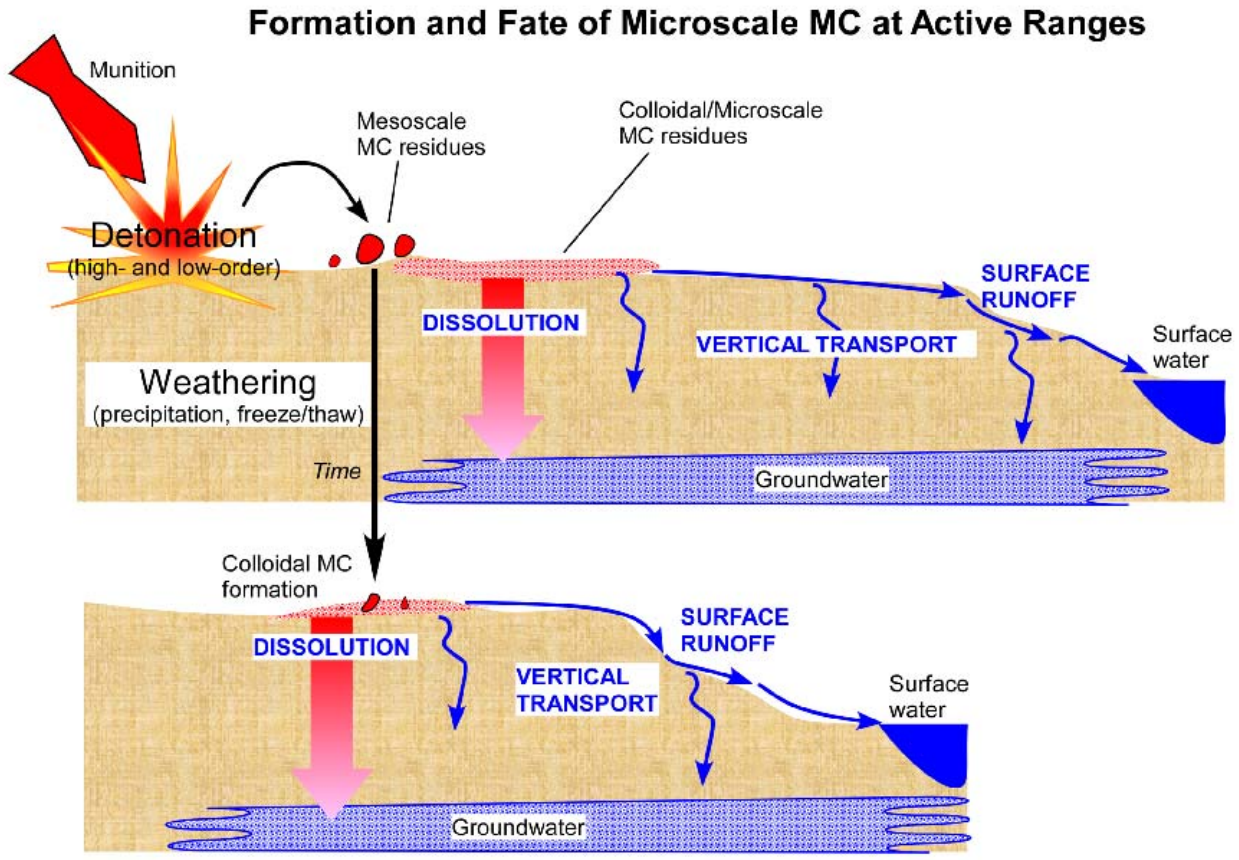

Figure 1-4. Formation and fate of microscale MC at active ranges.

Vertical and horizontal migration of colloids (e.g., bacterial cells, natural organic matter) has been widely studied (see reviews in refs (9, 46)), and is controlled by straining/filtration processes, aggregation, buoyancy, flow velocity, aqueous geochemistry, and particle (soil and colloid) surface properties. However, the migration of microscale MC has not been well studied. MC particles are heterogeneous mixtures of primary explosives (TNT, RDX, HMX) and stabilizing waxes that can dissolve and degrade as they are transported, thereby resulting in physical and chemical changes to the particles themselves. To the best of our knowledge, before our project, no studies had been performed to evaluate the transport (infiltration or surface run-off) of these colloidal particles, or their impact to ground and surface water quality.

While infiltration of microscale MCs into unsaturated soil has not been studied, the migration of colloidal pathogens (such as *E. coli* and *Cryptosporidium* oocysts) into unsaturated soils has been extensively studied (7, 17, 43). These studies demonstrate that colloid-sized pathogens

originating from fertilizers and animal wastes can migrate through soil due to rainfall, thereby serving as potential non-point sources to underlying groundwater. Although clearly not a direct analogue to MC migration through soils, these agricultural pathogen studies show that surface-applied colloidal contaminants can enter the vadose zone and impact groundwater. Dontsova et al. (2007) (12) showed that natural mineral colloids can enhance transport of RDX and TNT by up to 15% and 20%, respectively. RDX and TNT attachment to natural colloids facilitated their transport through soils. However, this study did not consider the presence of actual MC micro-particulates, as RDX and TNT were present only in the dissolved and adsorbed phases. Depending on the concentration and migration of miscroscale MC, their contribution to overall MC transport could be several times greater than via dissolved or natural colloid-bound transport alone.

In addition to infiltration into soil, miscroscale MC can potentially migrate horizontally via surface run-off processes. The issue of non-point source pollution and contaminated runoff has gained attention recently, especially in regards to agricultural land use (pesticides, nutrients, soil erosion, microorganisms, etc. (4, 18, 42, 59)), and urban and highway runoff (petroleum products, heavy metals, etc.(2, 8, 40, 41). Surface run-off issues related to colloidal pathogens has also been examined (35, 48, 53), so many of the factors controlling surface runoff have been investigated previously. However, the specific issue of MC contamination of surface runoff from DoD facilities, and the movement of colloidal MC in runoff, has not been addressed in the published literature.

The major landscape features influencing surface runoff include soil type, land use, slope, and vegetative coverage. A site with sandy soil will generally produce less runoff than a silty/clay soil under similar rainfall conditions. A site with steeper slopes, such as a hillside, will produce more runoff than a flat plain area. Additionally, vegetation usually reduces the amount of runoff leaving the area, a fact which has been used with some success to reduce surface runoff transport of nutrients, soil, and pesticides from agricultural fields (3, 19, 54). The possibility of surface runoff transport of MC (as either dissolved or colloidal material) at training ranges has been discussed (47), especially as it relates to stormwater management. Given that most high use target areas are sparsely vegetated, and that targets are often on the "high ground" at operational ranges, there is an increased probability that colloid-sized MCs are being transported by surface runoff processes.

Dissolution of MC Colloids

In addition to the potential migration of microscale MCs, retention of these particulates in surface (or, near-surface) soils likely contributes substantially to dissolved phase flux, as small particles dissolve more rapidly due to their increased surface area per unit mass (38, 50). The vertical and horizontal dispersion of these colloids, even if limited, can also enhance dissolution

by creating a larger "source" zone and increasing the contact time between flowing water and the solid particles. For the case of vertical MC transport, the movement of microscale MCs even a few centimeters into a permeable soil can have a substantial impact on contact time and ultimately dissolved MC concentrations migrating through the vadose zone. Similarly, horizontal colloid migration can increase the areal extent of the contamination zone, resulting in greater dissolved concentrations in surface run-off, and greater impact to surface receptors.

Microscale MCs, based on their large surface area:mass ratio, were expected to have much higher dissolution kinetics compared to particles 1 mm in size or larger. A preliminary test was performed before this project started using the MC particulates we prepared and observed in our laboratory. The colloidal MC solution, which contained approximately 0.3 mg of Composition B particulates per milliliter, was passed through a glass microfiber filter unit (0.45 μm pore size) to collect the colloids and allowed to dry. Another filter was loaded with dry Composition B particles that were between 0.5 and 1.0 mm in diameter. Each filter contained the same mass of Composition B. A flow of artificial rainwater (~1.5 ml/h) was then passed through the filters, and the effluent was collected using a fraction collector at 1 hour intervals. The effluent was analyzed for dissolved explosive concentrations using HPLC. The results from this experiment are presented in Figure 1-5.

The cumulative mass of HMX and RDX that dissolved and was eluted (relative to the initial mass on the filters) from the microscale Composition B was on the order of 5 to 8 times greater than from the 0.5-1.0 mm particles. These results of our preliminary laboratory testing clearly indicated that microscale MCs generate a much larger flux of dissolved explosives compared to larger residue particles. Thus, understanding the extent of microscale particulate migration near MC source area, and their subsequent fate, transport, and dissolution properties is critical for determining overall energetic compound flux to ground and surface waters.

In summary, microscale MC can be created via detonation and/or weathering processes. Once formed, these MC particles have the potential to migrate downwards through the vadose zone and potentially into underlying groundwater, and/or horizontally via surface run-off processes. These colloidal transport processes can facilitate dispersion of energetic compound sources (e.g., undissolved TNT, RDX, and HMX), as well as enhance the overall dissolved contaminant flux to groundwater and surface water receptors.

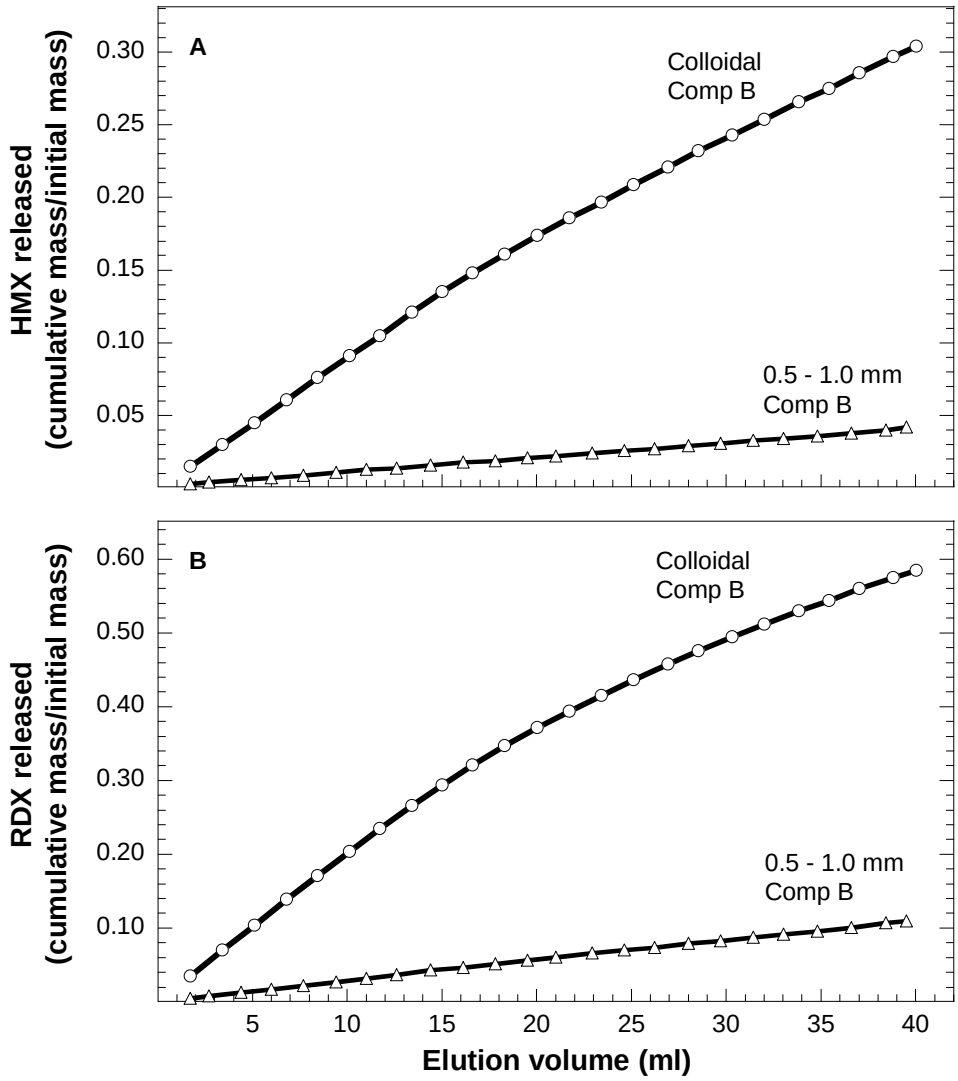

Figure 1-5. Comparison of dissolution kinetics of 0.5-1.0 mm and colloidal/microscale Composition B residues.

Project Objectives

In light of the state of the science, and the research needs identifed, when this project was envisioned, the overall objective was to generate fundamental information regarding the generation, transport, and dissolution of microscale MC, and make this information available for use during environmental risk assessments and other range assessments, leading to improved estimates of MC loadings at operational ranges.

The specific goals of this project contributing to the overall objective were as follows:

a) Characterize the microscale MC particles in residues from detonations and from weathering of residues.
b) Identify the mechanisms controlling the transport, retention, and dissolution of colloidal MCs by visualizing microscale MC in glass micromodels.

c) Examine the comparative dissolution kinetics of miscroscale and mm-sized MCs in under constant saturated flow conditions.

d) Compare the vertical transport and dissolution of microscale and mm-seized MCs in laboratory sand columns under unsaturated flow conditions.

e) Characterize the production of microscale MCs during realistic precipitation-driven weathering of cm-sized detonation residues.

f) Perform an initial survey to characterize the presence of dissolved and microscale MC in surface runoff from and active range.

2.0 PROJECT TASKS

2.1 Task 1 – Microscale Composition B Residue Dissolution in Glass Micromodels

The results summarized in this section here have been published:

> Wang, C., M. E. Fuller, V. Lazouskaya, J. Caplan, C. E. Schaefer, and Y. Jin. 2011. Dissolution of microscale energetic residues in saturated porous media: Visualization and quantification at the pore-scale by spectral confocal microscopy. Environmental Science and Technology 49(19): 8352–8358.
>
> Wang, C., M. E. Fuller, C. E. Schaefer, J. Caplan, and Y. Jin. 2012. Dissolution of explosive compounds TNT, RDX, and HMX under continuous flow conditions. Journal of Hazardous Materials 217-218: :187–193.
>
> Wang, C., M. E. Fuller, C. E. Schaefer, D. Fu, and Y. Jin. 2012. Modeling the dissolution of various types of mixed energetic residues under different flow conditions. Journal of Hazardous Materials 235-236: 138-143.

2.1.1 Goal

The goal of this task was to develop a method to visualize microscale MC and to apply the method to measure the dissolution kinetics of MC residues at the microscopic level in glass micromodels under saturated flow conditions.

2.1.2 Introduction

Both drop-wise (25, 33, 52) and column flow (13, 16, 34) experiments have been performed to investigate the dissolution of energetic residues to better understand their behavior in the environment. Lever et al. (25) and Taylor et al.(52) mimicked the precipitation-induced dissolution of energetic residues placed on glass holders frits and concluded that the lower-solubility of RDX controlled the dissolution of both RDX and TNT in formulations containing a mixture of both compounds. Monteil-Rivera et al.(33) determined that the dissolution rate of particles was governed by the slower dissolving compound(s), e.g. HMX in the particles of both octol (HMX/TNT: 70/30) and GIM (Greener Insensitive Material) [HMX/TNT/ETPE (energetic thermoplastic elastomer): 51/41/8] particles. Morley et al.(34) investigated the dissolution of energetic residues in a saturated sandy soil column and found that the particles readily dissolved and the higher flow velocity yielded higher dissolution rates. These previous studies examined cm- to mm-sized energetic residues, whereas sub-mm energetic residues, which are more mobile and also have higher surface-to-volume ratios (and, hence, higher theoretical dissolution rates)

than larger sized particles, have not been well studied. Moreover, direct observation of the dissolution of energetic residues at the pore-scale has not been reported, but is of great importance considering that pore-scale observations usually provided valuable mechanistic insights, leading to potential improvement of conceptual and mathematical models (44, 45).

This task investigated pore-scale dissolution of microscale energetic residues in saturated porous media, focusing on visualization and quantification of dissolution process. The particles examined were derived from detonation residues of the widely used explosive Composition B (a mixture of TNT, RDX, and HMX), so it was essential to have a method allowing visual identification of the major components, in addition to being able to observe the whole particle.

To achieve this, spectral imaging based on laser confocal microscopy was developed and evaluated. Spectral imaging has been applied widely for chromosome karyotype analysis (61), as well as for imaging of fluorescently-labeled live cells (63). The applicability of spectral imaging for explosive compounds (and specifically for visualizing and quantifying their dissolution) has not been previously reported.

2.1.3 Methods

Solution Chemistry. An artificial rainwater (ARW) was prepared and used in all experiments. The solution was composed of (mg L^{-1} deionized water): $NaHCO_3$, 2.75; HNO_3, 1.75; $MgSO_4 \cdot 7H_2O$, 2.50; $MgCl_2 \cdot 6H_2O$, 0.15; $CaCl_2 \cdot 2H_2O$, 0.20; KCl, 0.04; $(NH_4)_2SO_4$, 0.75; NH_4OH, 1.00; $CaSO_4 \cdot 2H_2O$, 5.00; and KOH, 0.40. The resultant solution ionic strength was ~0.3 mM and the pH was 5 S.U.

Energetic Residue Preparation. Composition B is a melt-cast explosive, in which crystalline RDX (with comingled HMX, the result of the RDX synthesis process) is mixed into molten TNT and cast in a variety of shapes. Thus, the RDX is embedded in a matrix of TNT once the material cools and hardens. Composition B residues were composed of TNT, RDX, and HMX (36: 57: 7 wt%) with a small fraction of stabilizing wax (usually ~1% by weight).

Microscale energetic residues were prepared from larger pieces of detonated Composition B provided by the Naval Explosive Ordnance Disposal Technology Division (Blossom Point, MD). Large cm-sized pieces were broken into mm-sized particles, attrited by grinding, then size-separated by sieving, following a previously published method (31), with minor modifications. Briefly, ~5 g of mm-sized energetic residues were placed in a small glass jar along with solvent-cleaned stainless steel cylinders (10 × 16 mm or 13 × 13 mm). The jar was shaken on an orbital shaker at 260 rpm for 3 h. The resulting material was sieved using the US standard sieves #35 (500 μm), #60 (250 μm), #120 (125 μm), #325 (45 μm), and #635 (20 μm). The size fraction passing through the #325 but retained on the #635 (20 to 45 μm) was collected and used for the

present study. Particles of neat TNT (linear crystals, 100 to 1000 μm), RDX (oblong crystals, 10 to100 μm), and HMX (oblong crystals, 5 to 50 μm) were also prepared by recrystallization from saturated solvent solutions prepared with 99% pure compounds. Representative transmission light (bright field) images of TNT, RDX, and HMX crystals are shown in Figure 2.1-1.

Energetic Residue Characterization. To measure the size of the microscale energetic residues, scanning electron microscopy (SEM) and transmission light images of dry and wet energetic residues were captured. Samples of dry particles were sputter-coated (Denton bench top turbo III sputter coater) with a gold/platinum mixture and were scanned with a field emission scanning electron microscopy (FE-SEM) (Hitachi 4700) at 3.0 kV. Samples of wet energetic residues in the ARW were observed with the transmission light under a Zeiss LSM 510 Meta confocal microscopy immediately after they were prepared.

The electrophoretic mobility of the microscale energetic residues was measured using a Zetasizer Nano ZS (Malvern Instruments) at 25 ± 0.5 °C. Residues were added to the experimental solution at 0.75% (w:v) concentration and measurements were made for duplicates with three cycles for each analysis. The measured electrophoretic mobility was used to calculate the zeta-potential according to the Smoluchowski equation. (20).

The contact angle of the energetic residues was measured by preparing a suspension of the residues and applying it drop-wise to a clean glass slide, allowing the liquid to evaporate to form a uniform layer. A water drop of 3 μL was placed on the dried layer and high resolution digital photographs from three separate drops were captured. The contact angle was measured from the digital images using ImageJ 1.42q software (1).

Micromodel Preparation and Operation. Soda-lime glass beads (180 to 250 μm) (Mo-Sci Corporation, Rolla, MO) were chosen as the model porous media. The glass beads were thoroughly cleaned to remove grease and other impurities, as follows: soaking in 2% Extran MA02 surfactant solution (EM Science, Gibbstown, NJ) for 1 h; repeatedly rinsed with deionized (DI) water; sonicated for 15 min in 2% RBS35 detergent solution (Pierce Biotechnology Inc., Rockford, IL); rinsed thoroughly with DI water; soaked for 24 h in a solution containing sulfuric acid and NOCHROMIX (Godax Laboratories, Inc., TakomaPark, MD); rinsed repeatedly with DI water; and dried overnight at 105°C.

The micromodel experiments were conducted with an uncoated, sterile IBIDI μ-slide VI glass chamber which had six microchannels (AutoMate Scientific, Inc., Berkeley, CA). Clean glass beads were packed into the channels, creating a well-defined porous media system (Figure 2.1-2), with each channel having a pore volume (PV) of 12.8 μL.

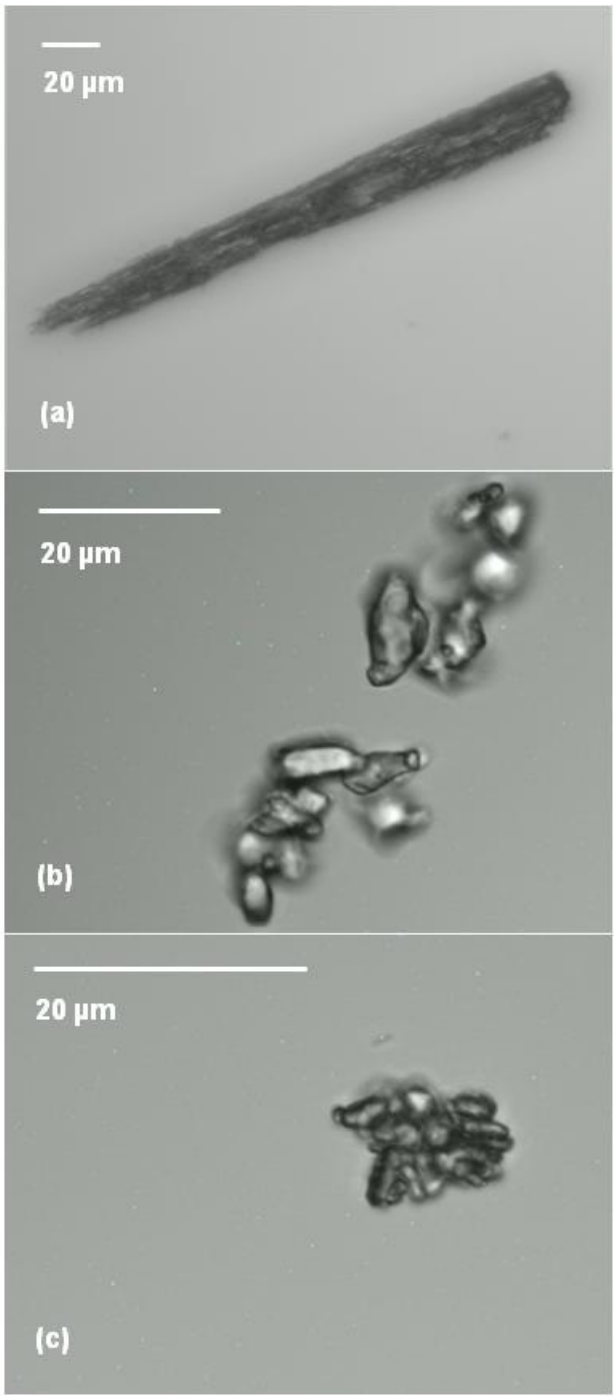

Figure 2.1-1. Representative transmission light (bright field) images of (a) linear TNT crystals, (b) oblong RDX crystals, and (c) oblong HMX crystals..

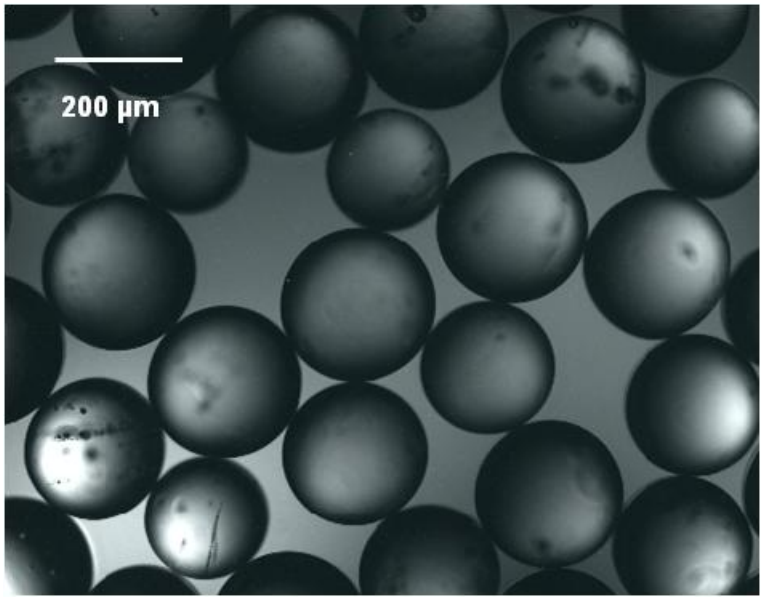

Figure 2.1-2. Bright field image of the packed glass beads in a micromodel channel.

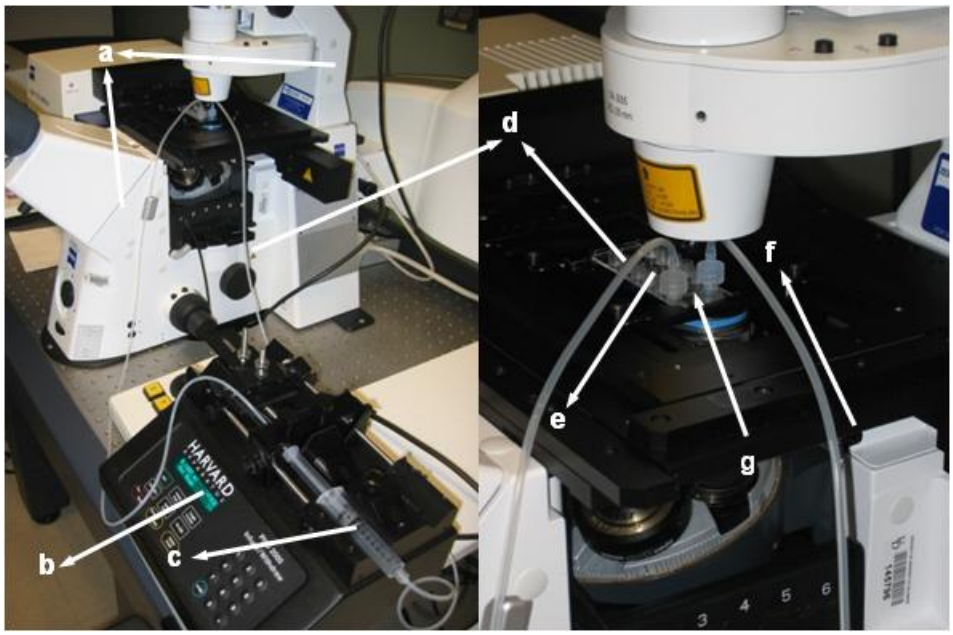

Figure 2.1-3. Experimental setup of the micromodel experiments: (a) confocal microscopy, (b) syringe pump, (c) syringe, (d) silicon tubing, (e) effluent, (f) influent, (g) micromodel channel..

The experimental setup of the micromodel experiments is illustrated in Figure 2.1-3. The channel was initially flushed several times with ARW. An aliquot (20 μL) of the microscale energetic residues suspension in ARW (0.75% wt:vol of residues; ~240 particles μL^{-1}) was injected into the channel, followed by a continous flow of ARW at a flow of 60 μL min^{-1} (4.7 PV min^{-1}) using a Harvard PHD 2000 syringe pump.

To document dissolution, selected residue particles were properly focused under the confocal microscopy and spectral images were captured underduring water flow conditions. Each dissolution experiment was repeated a minimum of three times. Spectral imageswere acquired by using the 405 nm laser light to excite the microscale particle in the field of view, followed by scanning in lambda mode. Images were captured in 3-D over time (4-D) using Zeiss LSM 510 confocal software (Version 4.2). A summary of the representative parameters and instrumental settings is given in Table 2.1-1.

parameter[a]	lambda mode
scan mode	plane
scam zoom	0.7 ~ 2.0
scan speed	8
resolution	800 × 800
objective (lens)	C-Apochromat 40x/1.20 water
average	line 2
pinhole	ChS: 444 μm
filters	ChS: 411 - 754 μm, 20 nm interval
beam splitters	MBS: HFT 405/514/633
	DBS1: none
	DBS3: none
	FW1: none
wavelength	405 nm, 6.0%

[a] Time delay of 4.5 minutes was set after each z-stack scanning.

Table 2.1-1. Summary of the representative parameters and instrumental settings for the Zeiss LSM 510 Meta confocal microscopy.

Spectral images, which captured a full emission spectrum (i.e., emission intensity at various wavelengths from 411 to 754 nm in this case) at every pixel, were processed using the LSM 510 confocal software with the linear unmixing method (61), which is the most useful approach for

decomposing spectral images (62). The spectra of individual TNT, RDX, and HMX were acquired under identical conditions beforehand and were used as reference spectra (or spectral signatures) during the linear unmixing step. The processed images were reconstructed into 3-D images, and were analyzed to quantify particle volume (μm^3) and surface area (μm^2) using the Volocity image analysis software (Version 4.1.0).

2.1.4 Results and Discussion

Characterization of Microscale Energetic Residues. Particle size, shape, and surface potential are of interest in this study because they impact the behavior of microscale energetic residues in subsurface environments.

Figure 2.1-4(a) shows that microscale dry physically attrited energetic residues were composed of larger particles of irregular polyhedral shape with some adhering colloidal-sized particles (<4 μm). These results were similar to a previous observation reported by Webb et al. (58) that showed colloidal-sized (~2 μm) particles aggregate onto larger particles when Composition B was dry attrited. The sizes of the microscale dry energetic residues averaged 34 ± 12 μm × 26 ± 10 μm (Table 2.1-2). Similar morphological features were observed when the energetic residues were placed in water [Figure 2.1-4].

The measured electrophoretic mobility of the microscale energetic residues was -3.45 ± 0.23 (μm·cm)/(V·s) (Table 2.1-2) and correspondingly the calculated zeta-potential was -44.1 ± 2.9 mV, indicating that the surface of the residues was negatively charged. Additionally, the average contact angle of microscale energetic residues was 109 ± 4°, confirming that the explosive residues were moderately hydrophobic (60).

parameter	value	unit
dry size	(34 ± 12) × (26 ± 10), n = 84	μm
wet size	(38 ± 11) × (27 ± 8), n = 96	μm
electrophoretic mobility	-3.45 ± 0.23	(μm·cm)/(V·s)
zeta-potential	-44.1 ± 2.9	mV
contact angle	109 ± 4	degree
mass ratio of TNT/RDX/HMX	36%: 57%: 7%	dimensionless

Table 2.1-2. Characterization parameters of microscale energetic residues.

Spectral Signatures of Explosive Compounds. Reference spectra of TNT, RDX, and HMX were acquired at the excitation wavelength of 405 nm in order to identify them from their mixture such as Composition B particles.

Figures 2.1-5(a1) and 5(a2) show that TNT autofluoresced green, with emission peak split at 514 nm and 633 nm. The two peaks resulted from the beam splitters (514 nm and 633 nm) in the confocal instrument causing the fluorescent signal at both wavelengths to be attenuated. Further, Figures 2.1-5(b1), 5(b2), 5(c1), and 5(c2) demonstrate that RDX and HMX have similar blue and red fluorescence with almost identical spectral signatures. Figures 2.1-5(b1) and 5(c1) show that the red emission peak of RDX/HMX occurred in the range of >700 nm and was not fully acquired due to limitations of the confocal microscope (signal cutoff at 754 nm).

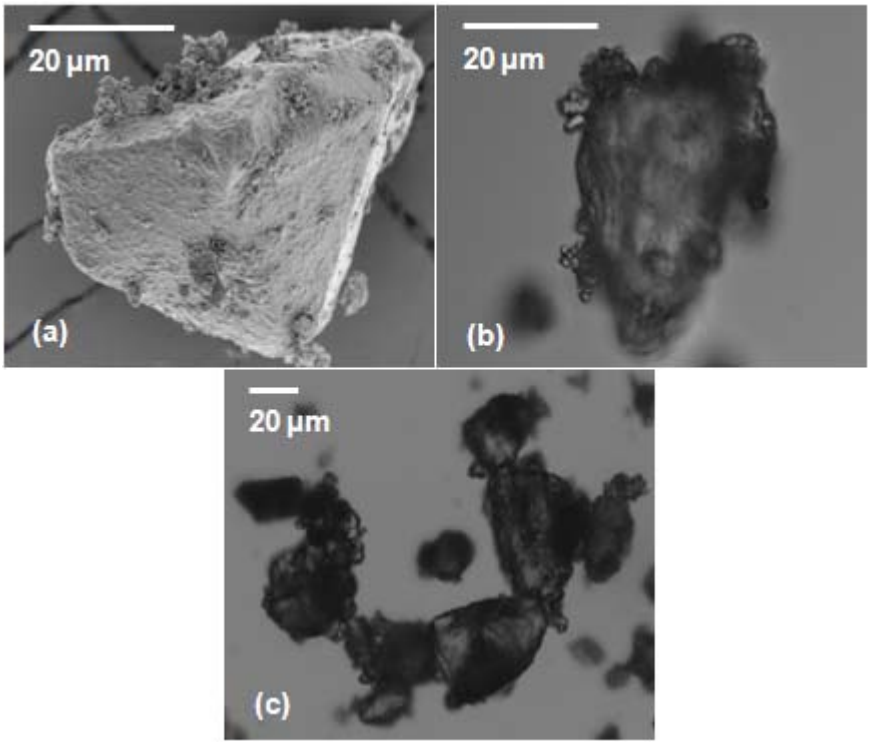

Figure 2.1-4. Morphology of microscale energetic residues: (a) representative SEM image of a dry particle; representative transmission light (bright field) images of (b) a single and (c) an aggregated particle in the experimental solution.

Because of the nearly identical spectral signatures of RDX and HMX, the blue and red RDX signatures were used to identify the mixture of RDX and HMX, which is referred to as "RDX/HMX". The spectral signatures of TNT and RDX were used to visually identify TNT and RDX/HMX regions in actual energetic residues. Figures 2.1-6 demonstrate the validity of the

method and show that the green TNT was easily distinguished from the blue and red RDX/HMX regions in a representative Composition B particle.

These are the first results indicating that the components of a common explosive formulation (e.g., Comp B) can be detected by visible light autofluorescensce. Previous literature has shown weak autofluorescence under UV illumination (30, 39), but the current findings are in contrast with the previous knowledge that these explosive compounds are not inherently florescent at the excitation wavelengths of visible light (380 to 750 nm). (32). The reasons might be that the intensity of the light source to excite samples in this study was stronger than used in previous studies, as well as a more sensitive photodetector.

Visualization of Dissolution Process. The spectral analysis method described above was applied for visualization of dissolution of TNT and RDX/HMX from physically attrited microscale Composition B residues in the micromodel over a period of ~2.0 h. Throughout the dissolution process, the experimental solution was flowing through the channel from right to left in Figures 2.1-7(a) to 7(h) at a rate of 60 μL min^{-1} (or 24 cm h^{-1}). This is higher than the infiltration rate through porous media expected from a typical rainfall rate of 0.06 to 4 cm h^{-1}, but allowed particle dissolution to be observed within a reasonable timeframe. Figure 2.1-7(a) shows that at the beginning (t = 0 min) the green TNT was conspicuous. As time elapsed, the green TNT became less prominent (Figures 2.1-7(a) to 7(c)), indicating that TNT was dissolving in the flowing water. Meanwhile, the red area of RDX/HMX became more visible, which was because TNT was dissolving faster than the red RDX/HMX. As the process continued further, the red area of RDX/HMX became gradually invisible (Figures 2.1-7(c) to 7(h)), indicating the ongoing dissolution of RDX/HMX. Meanwhile, it can be seen from Figures 2.1-7(a) to 7(h) that as the dissolution continued, the size of the energetic residue decreased from ~38 × 35 μm to ~29 × 17 μm. Overall, the spectral imaging vividly demonstrated the dissolution of single microscale Comp B residues, as well as the differential dissolution of the individual explosive components, under flow conditions.

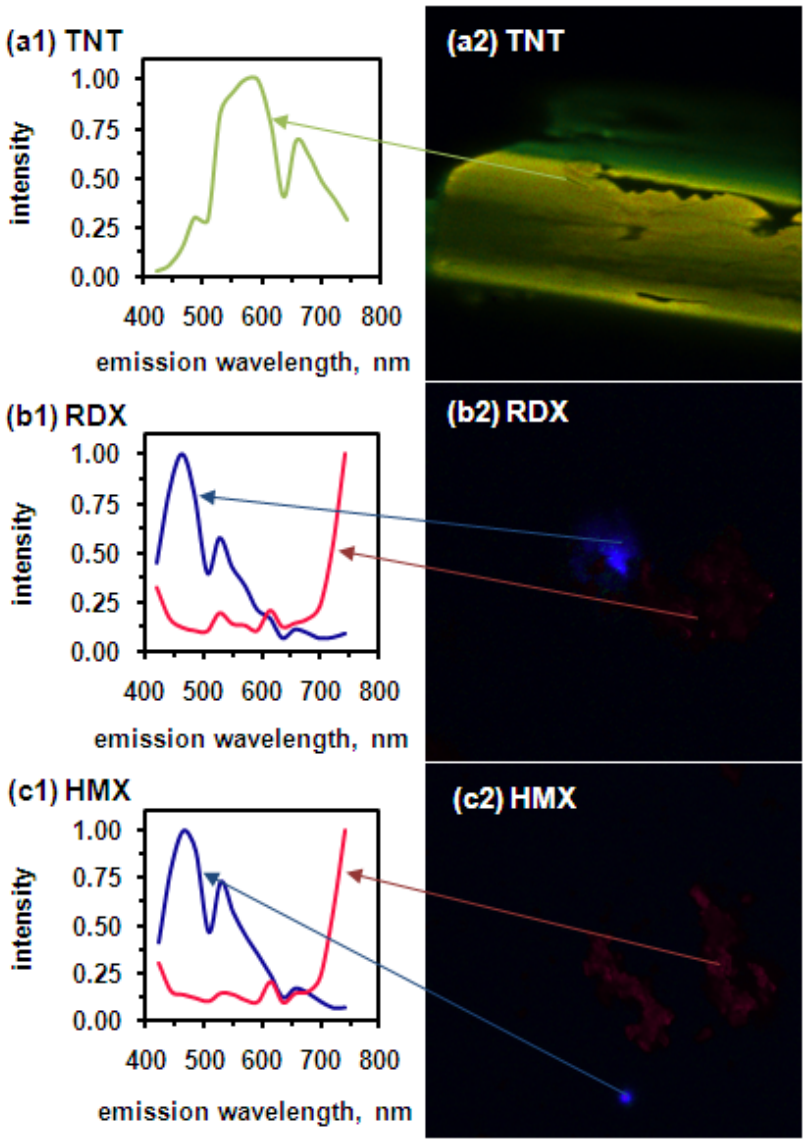

Figure 2.1-5. Representative spectral signatures of (a1) TNT, (b1) RDX, and (c1) HMX with their respective spectral images of (a2) TNT, (b2) RDX, and (c2) HMX upon excitation at 405 nm.

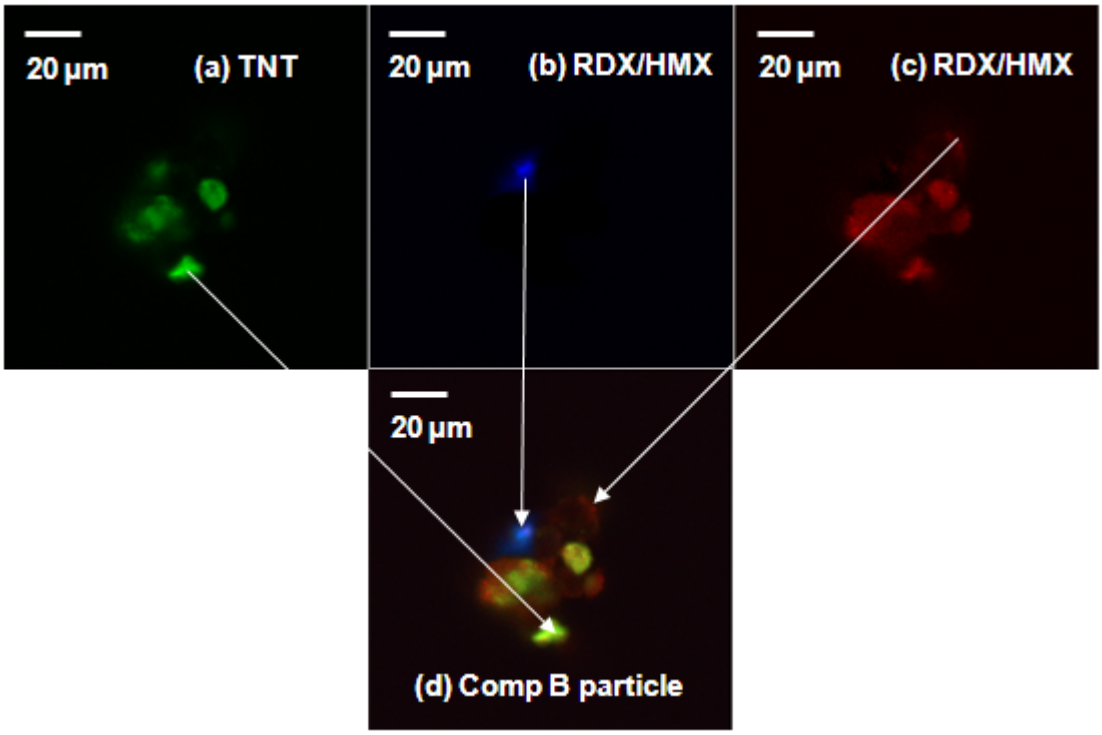

Figure 2.1-6. Processed images of a microscale energetic residue: (a) green, TNT; (b) blue, RDX/HMX; (c) red, RDX/HMX; and (d) Composition B particle.

Quantification of Dissolution Process. To obtain quantitative information and mechanistic insights, the dissolution images were processed using Volocity (Version 4.1.0) to analyze the evolution of the following parameters: particle volume, mass, surface area, shape factor, specific surface area, and dissolution rate and flux (see the definition and calculation in the Supporting Information). The shape factor is defined as the inverse ratio of the surface area of a microscale energetic residue to that of a perfect sphere that has the same volume (37). If the residue were a perfect sphere, the shape factor would be 1. The shape factor decreased as the residue became more irregular. The potential evolution of the shape factor is further illustrated in Figure S7.

The measured parameters based on three replicate particles are presented in Figures 2.1-8. Figures 2.1-8(a1) and 8(a2) show that the volume, surface area, mass, and dissolution rate and flux of the Comp B particles decreased quickly initially, slowing down thereafter. There was a slight increase in the shape factor of the Composition B particles over the observation period (Figure 2.1-8(a3)); the specific surface area increased initially and was then slightly decreased (Figure 2.1-8(a4)). The changing trends of volume, surface area, shape factor, specific surface area, mass, and dissolution rate and flux of the pure compounds TNT and RDX/HMX followed those described for the Composition B residues (Figures 2.1-8(b1) to 8(b4), 2.1-8(c1) to 8(c4)).

The increase in the shape factor of the Composition B particles is so small that it could be regarded as stable (Figure 2.1-8(a3)). In addition, the values of the shape factors are much less than 1, suggesting that the shapes of the Comp B particles, TNT, and RDX/HMX were very irregular and far deviated from a perfect sphere. Accordingly, the assumption of spherical energetic residues in some dissolution models (29, 33) can be eliminated by incorporating shape factors. The observation that the specific surface area initially increased and then slightly decreased (Figures 2.1-8(a4)) may be attributed to that, first, as the dissolution proceeded, the particle size decreased (Figures 2.1-8(a1)), which contributed to an increase in the specific surface area, and second, the dissolution slowed down at around t = 36 min and thereby the particle volume became stable, whereas the surface area of the particles was still decreasing slightly.

The observation that the dissolution of Comp B particles and their components (i.e. TNT and RDX/HMX) occurred quickly at the beginning and slowed thereafter (Figures 2.1-8(a1), 8(b1), and 8(c1)) are in good agreement with the previous research employing dripping water and in column flow experiments. Taylor et al. (2009), Lever et al. (2005) and Monteil-Rivera et al. (2010) previously simulated precipitation-driven dissolution of mm-sized energetic residues that were supported on glass frits, and observed that the mass-loss of TNT and RDX from Composition B particle or TNT and HMX from octol and GIM particles increased very quickly due to the fast initial dissolution and then decreased because of the slow dissolution thereafter. Furey et al. (2008) investigated the elution rates of TNT and RDX from Composition B using

accelerated solvent extractor cells packed with Ottawa sand and mm-sized energetic residues. They reported that the dissolved concentrations of TNT and RDX in the cell effluent increased quickly at beginning and slowed thereafter. Lever et al. (2005) also observed that for some types of energetic residues, the onset of the dissolution was delayed during drop-wise dissolution, which was attributed to reduced wetting due to surface texture or waxy deposits on the particle surfaces. This was not observed in the present study, likely due to the processing employed to generate the microscale particles from the macroscale detonation residues (eg., dry physical attrition). As such, the results presented here may be more representative of microscale explosive residues generated by physical attrition of larger particulate material as opposed to those formed directly from detonations. Further investigation of microscale residues generated directly from detonations, as well as those generated by aqueous weathering of larger residues, are warranted, as these particles may have a different distribution of waxy and/or sooty material that could affect the wetting and dissolution of the explosive compounds..

With respect to the rapid initial dissolution observed in the previous studies, it was concluded that the slow dissolution of RDX and HMX controlled the dissolution of Comp B (RDX/TNT: 60/39) and octol (HMX/TNT: 70/30) particles in the late stage, respectively, by limiting the exposed surface area of TNT. This mechanism could be responsible for the rapid initial dissolution of TNT observed in the present study, but it does not satisfactorily explain the initial fast dissolution of RDX/HMX (e.g., Figure 2.1-8(b1)). Dontsova et al. (2006) proposed that colloidal-sized Composition B particles attached to larger-sized particles might result in the initial high dissolution rate, considering that the attached colloidal-sized particles largely increased the overall apparent surface area available for dissolution. This scenario is plausible, but it does not explain the observation that the rapid dissolution continued until the majority (72%) of the particles dissolved (Figure 2.1-8(a1)), long after any small attached particles would have ceased to exist. Based on results from the present study, we propose that the large initial surface area facilitated rapid initial dissolution, and that the considerable reduction in the available surface area was responsible for the subsequent slow dissolution phase. Lynch et al. (27) and Morley et al. (2006) observed that the dissolution rate increased with the particle surface area, which to our understanding was because the large surface area favored the mass transfer of TNT, RDX, and HMX from the particle to the water. In the present case, the surface area of the Composition B particles was initially large, promoting fast dissolution, then decreased significantly (Figure 2.1-8(a2)), resulting in a reduced rate of particle dissolution.

Figure 2.1-9 shows that the mass ratio of RDX/HMX to TNT increased from 1.38 at t = 0 min to the maximum of 7.26 at t = 36 min, indicating that TNT dissolved preferentially over RDX/HMX at the early stage. This is consistent with the visual observation (Figures 2.1-7(a) to 7(h)) that the conspicuous green TNT became less prominent quickly as the dissolution continued. The preferential dissolution of TNT is a direct result of the fast volume reduction of TNT (Figure 2.1-8(b1)) in comparison to the relatively slow decrease of that of RDX/HMX in

the period from 0 to 36 min (Figure 2.1-8(c1)). These results are consistent with the literature reports (25, 52). The reasons for the preferential dissolution of TNT over RDX/HMX in this stage are likely as follows. First, since RDX/HMX was embedded in a matrix of TNT upon the manufacturing process, TNT in energetic residues mostly had a larger initially exposed surface area than the encapsulated RDX/HMX (25, 28, 29, 52). Second, TNT has much higher solubility than RDX/HMX in water, and thereby it has a stronger tendency to dissolve.

2.1.4 Conclusions

This task found that TNT, RDX, and HMX autofluoresced at different wavelengths under 405 nm laser light excitation, likely due to their different crystal states. Further investigation would be required, however, to determine why HMX and RDX emitted both blue and red autofluorescence. These two compounds are structurally similar nitramine explosives, but they are different in both their molecular formula and the expected conformation of their central heterocyclic rings.

The findings were successfully employed to visualize microscale physically attrited energetic residues using spectral confocal microscopy. The methodology allowed a quantitative analysis of the dissolution of microscale Composition B residues in saturated porous media. TNT dissolved preferentially over RDX/HMX at early times, and the Composition B residues dissolved quickly initially, slowing thereafter. Throughout the dissolution process, the shape factor of the residues was relatively stable. Thus, the assumption of spherical particles in some dissolution models may be eliminated by incorporating actual shape factors. We anticipate that the method developed can also be applied to other types of explosive residues that contain TNT, RDX, and HMX.

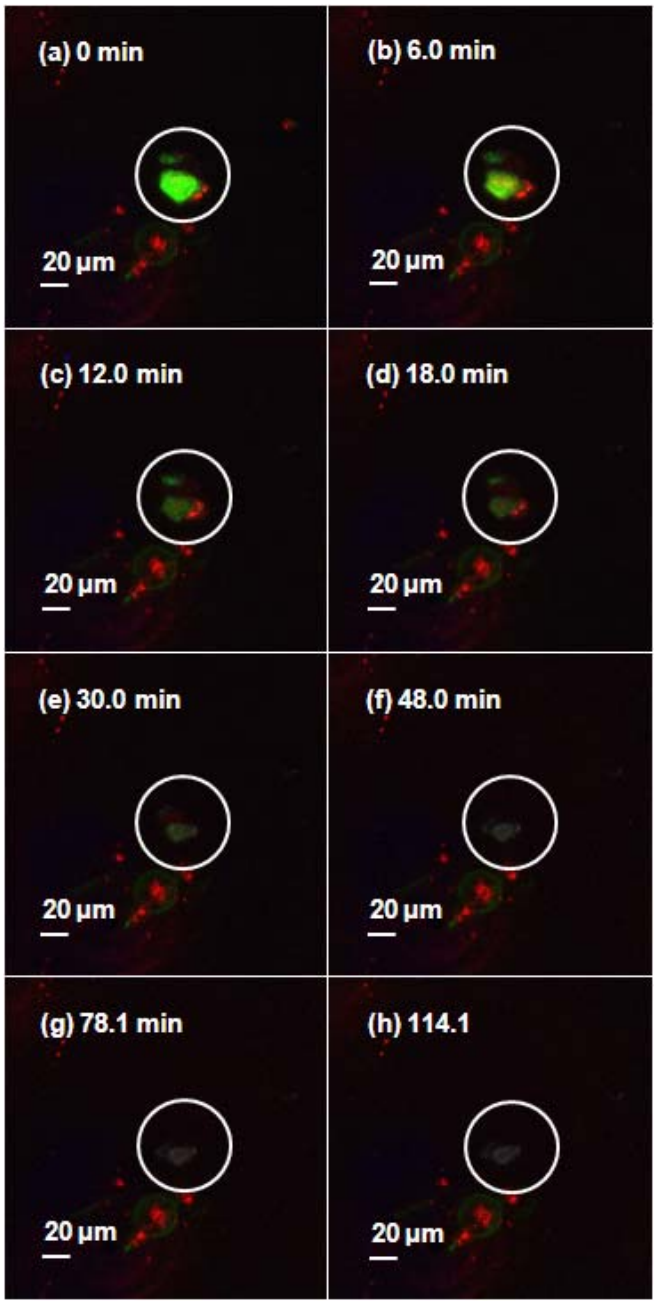

Figure 2.1-7. Visualization of the dissolution of a microscale energetic residue in saturated porous media.
Sequential plain views at (a) 0 min, (b) 6.0 min, (c) 12.0 min, (d) 18.0 min, (e) 30.0 min, (f) 48.0 min, (g) 78.1 min, and (h) 114.1 min. Water was flowing from right to left. The white circles in the images highlight the target energetic residue.

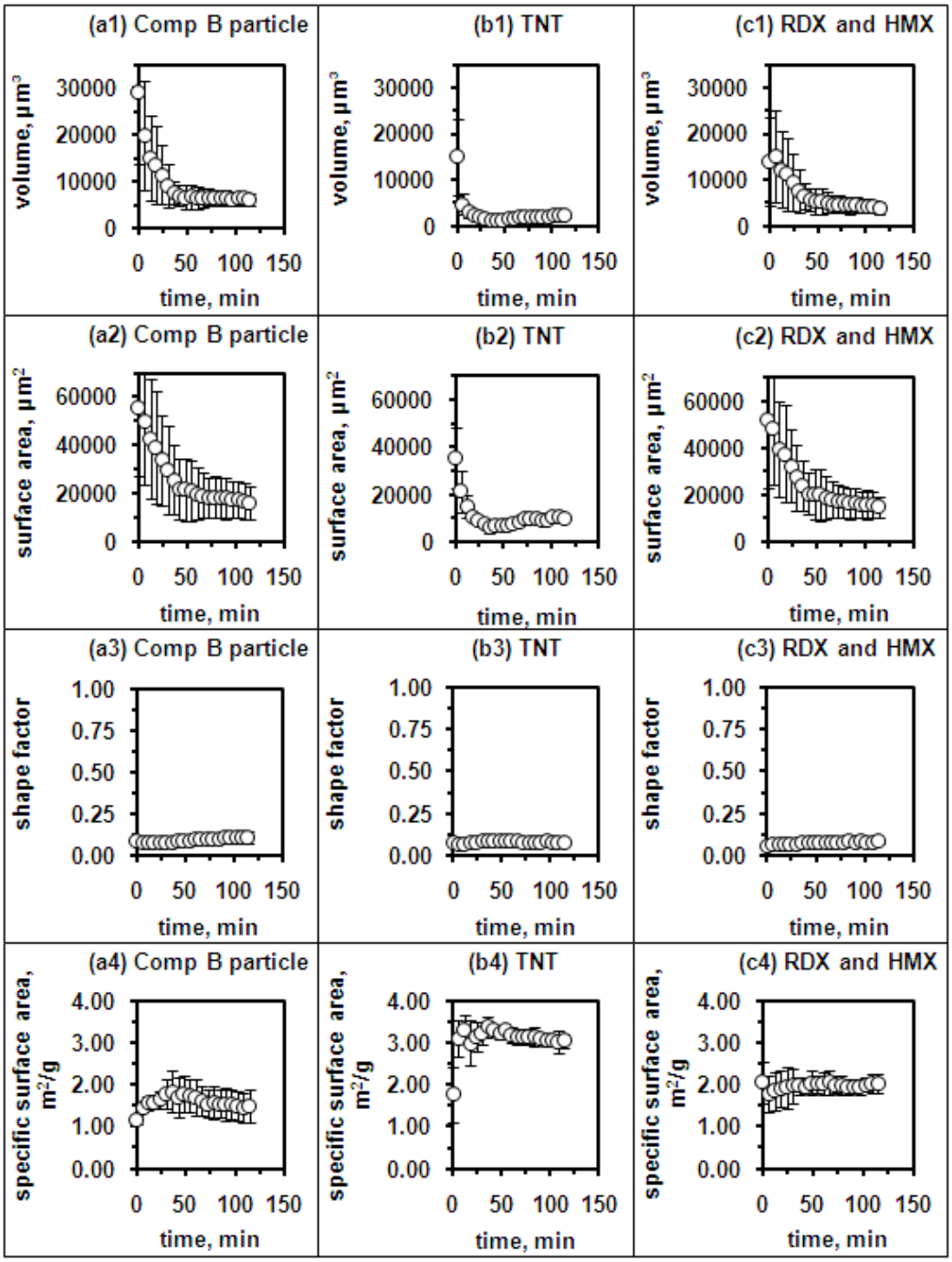

Figure 2.1-8. Quantitative analysis of dissolution of a microscale energetic residue in saturated porous media under continuous flow.

Evolution of Composition B particle, TNT, and RDX/HMX in regards to their respective (a1) to (c1) volume, (a2) to (c2) surface area, (a3) to (c3) shape factor, and (a4) to (c4) specific surface area. Data points are the average of triplicate measurements and error bars represent the standard deviation.

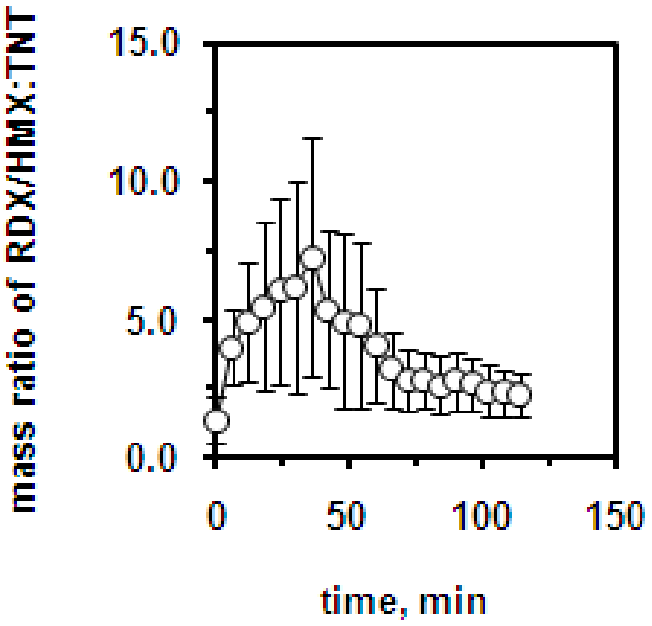

Figure 2.1-9. Mass ratio of RDX/HMX to TNT during dissolution of microscale energetic residues.

Data points represent the average of triplicate measurements and error bars denote the standard deviation.

2.2 Task 2 – Comparative Dissolution of mm-Sized and Microscale Composition B Residues

The results summarized in this section here have been published:

> Fuller, M. E., C. E. Schaefer, C. Andaya, V. Lazouskaya, S. Fallis, C. Wang, and Y. Jin. 2012. Dissolution kinetics of sub-millimeter Composition B detonation residues: Role of particle size and surface wetting. Chemosphere 88(5): 591-597.

2.2.1 Goal

The goal of this task was to systematically examine the dissolution kinetics of microscale Comp B detonation residues, and the compare the dissolution kinetics of mm-sized and microscale particles.

2.2.2 Introduction

Although material on the order of 50 μm in size was detected from some detonations (50), the properties of residues in the colloidal size range have not been extensively studied. These microscopic particles represent a very high surface area fraction, and as such, could contribute significantly to the mass flux of explosives at ranges. In addition, microscale residues could be more mobile than larger particles, resulting in spreading of the "source term" of explosives from the point of detonation both horizontally across the area and vertically into the soil profile. This task was undertaken to examine microscale particles of Comp B, with specific attention to their dissolution characteristics and explosive mass transfer kinetics.

2.2.3 Methods

Energetic Residues. The largest amount of Comp B detonation residues were provided by the Naval Explosive Ordnance Disposal Technology Division (EODTECHDIV, Blossom Point, MD). Residues 1 cm in size or greater were collected by hand from the blast area after low-order detonation of 81- and 155-mm mortar rounds using a plasma disruptor (est. 50-80% yield). Hand-sorted residues in the size range of 0.5 to 1 mm from blow-in-place detonation of a 55-mm mortar round were a gift from Dr. Susan Taylor at the U.S. Army Corp of Engineers Engineer Research and Development Center/Cold Regions Research and Engineering Laboratory. Additional residues, and soot from a high-order detonation, were generated by the Detonation Mechanics Laboratory at the Naval Air Warfare Center Weapons Division, China Lake via controlled detonation of blocks of Comp B. Briefly, the acceptor Comp B charge was suspended underwater inside a 20 L plastic bucket by copper wire. A donor charge (two 2.5 cm x 5.1 cm diameter Pentolite charges) was also suspended by copper wire at the correct standoff distance

from the Comp B. The bucket was placed in an open air detonation chamber and detonated remotely. Residue and soot were collected by hand from the floor of the chamber after each detonation. Undetonated Comp B was also supplied by China Lake.

Larger cm-sized pieces of EODTECHDIV Comp B were broken into sub mm-sized particles by three methods: physical attrition, milling, and aqueous weathering. Physical attrition consisted of grinding Comp B residues, followed by size-separation by sieving based on a previously published soil attrition method (31) with minor modifications. Briefly, about 5 g of mm-sized energetic residues were placed in a small glass jar along with solvent-cleaned stainless steel cylinders (10 × 16 mm or 13 × 13 mm). The jar was shaken on an orbital shaker at 260 rpm for 3 h. The resulting material was sieved using the US standard sieves #35 (500 μm), #60 (250 μm), #120 (125 μm), #325 (45 μm), and #635 (20 μm). The three smallest size fractions (20-45 μm, 45-125 μm, 125-250 μm) were collected and used for these studies. Milling was performed using a ceramic ball mill and ceramic stones. Small quantities of Comp B were added and milled at room temperature for 72 h. Both dry milling and wet milling [1:3 Comp B:water (w:w)] was performed, and undetonated Comp B was also milled for some studies. The term "wet-milled" is used here simply for convenience of distinguishing the various materials, and was in no real way similar to the process of aqueous weathering described next in terms of the Comp B: water ratio or the actual physical system.

Aqueous weathering was performed by manual size-reduction of residues through a 20 mesh steel screen (~800 μm opening), followed by mixing 1.5 g of Comp B with 1.8 L of purified water in a 2 L Bellco μ-Carrier spinner flask (Vineland, NJ, USA). Stirring speed averaged 250 rpm over the course of several weeks, generating a range of particle sizes through both dissolution and disintegration of the Comp B material. Based on the solubilities of the explosives and the proportions of the explosives in the Comp B, it was calculated that approximately 8% of the initial HMX and RDX, and 37% of the initial TNT, dissolved during the aqueous weathering process. Particles were concentrated from the mixing solution 40-fold by serial centrifugation (500 rpm, 25°C, 20 min) prior to use in dissolution experiments.

Particle analyses. Ratios of HMX, RDX, and TNT in the parent Comp B materials and the generated particles were measured by five replicate extractions of small subsamples (<5 mg) in acetonitrile for 18 h in a cooled ultrasonic bath, followed by HPLC analysis (see below).

Microscale Comp B particles were analyzed using a Elzone II 5390 particle size analyzer (Micrometritics Instrument Corporation, Norcross, GA, USA). Both 30 μm and 380 μm orifice tubes were used to allow a large range of sizes to be measured. Analyses were performed in a 1 to 2% NaCl solution saturated with HMX, RDX, and TNT to minimize particle dissolution during measurement (unless otherwise noted). A minimum of triplicate measurements were performed on each sample.

The zeta-potential and contact angle of a subset of the particle types was determined using procedures as described previously (56).

Effect of particle type and size on dissolution. Explosive dissolution from different types of microscale Comp B particles, as well as 0.5-1.0 mm residue particles for comparison, were performed by placing small amounts (~2 mg) of the material into the female luer inlet of a 13 mm glass microfiber syringe filter units (0.45 µm pore size; Whatman 6818-1304, GE Healthcare Biosciences, Pittsburgh, PA, USA). The male luer outlet of another syringe filter was then inserted, trapping the particles between the two filters. A flow of ARW (same composition as described in Task 1) was directed into the top filter unit at a rate of 1 mL h^{-1} (calculated linear velocity across the particles on the filter of 2.4 cm h^{-1}) using a syringe pump. Effluent from the filters passed through an 18 gauge stainless steel needle directly into a 2-mL vial (or a 20-mL vial during longer sampling intervals). Effluent volume was measured, and samples were analyzed for dissolved explosive concentrations by HPLC (see below). A minimum of triplicate dissolution experiments were performed with each particle type.

Explosives analysis. The concentrations of the explosives and their breakdown products were monitored during incubation using HPLC according to a modified EPA Method 8330 (www.epa.gov/epawaste/hazard/testmethods/sw846/pdfs/8330a.pdf) using a Dionex 3000 Ultimate HPLC with a Agilent Zorbax Bonus-RP column (4.6 x 75 mm, 3.5 µm particle diameter, 80 A pore diameter), variable wavelength detector (254 nm), and a photodiode array detector collecting peak spectral data. The Zorbax Bonus-RP stationary phase is composed of densely reacted, sterically protected diisopropyl-C14 groups bonded to an ultrapure SiO_2 support and triple endcapped. The mobile phase was 50:50 methanol:0.2% (v:v) trifluoroacetic acid in water at a flow rate of 1 mL min^{-1}. The column temperature was 33 °C. The practical quantitation limit was approximately 10 µg L^{-1}.

Mass Transfer Calculations. To facilitate comparison of mass transfer for the wide range of particle sizes tested, an approach to calculate an effective mass transfer coefficient for each experiment was employed. A simple conceptual model was employed to represent the dissolution process. The residence time (τ) of water flowing across the particles was defined as:

$$\tau = \frac{2r}{v} \qquad (1)$$

where r is the average particle radius and v is the average flow velocity. The particles were assumed spherical and present as a single layer on the filter support. While the single layer assumption is likely not entirely correct, we assume that the extent of any multi-layering among particle types is similar so that ultimately comparison of mass transfer coefficients among particle types is warranted (i.e., the contact time scales with the diameter of the particle). While

mass transfer coefficients were assessed for small times, where the mass loss of the particle was less than 15% for all experiments, the small changes in particle radius due to dissolution were calculated as follows:

$$r = \left[\left(\frac{\sum M_i X_i}{\sum M_{i,0} X_{i,0}}\right)\frac{3V_0}{4\pi}\right]^{\frac{1}{3}} \quad (2)$$

where r is the particle radius, V_0 is the initial particle volume, M_i is the mass of component i (where i is either TNT, RDX, or HMX), X_i is the mass fraction of component i, and the subscript 0 for the M and X terms denotes initial conditions.

The lumped mass transfer coefficient (κ_L), representing the product of the intrinsic mass transfer coefficient and the interfacial area per unit volume, for each explosive was derived from the explosive compound dissolution curves based on the following solution for dissolution of a bed of spherical particles (6)**:**

$$\frac{C}{C_{sat}} = 1 - e^{-\kappa_L \tau \frac{r^2}{{r_0}^2}} \quad (3)$$

where r_0 is the initial particle radius, C and C_{sat} are the effluent concentration and the aqueous solubility of the explosive, respectively. The ratio in the last term of the exponential accounts for the change in surface area of the particle during the dissolution, assuming a dissolving sphere model.

Equations 1 through 3 were solved for κ_L numerically in EXCEL using the SOLVER function. M_i and X_i for each timepoint were calculated based on the initial mass of the particle minus the measured dissolved mass that eluted from the residues.

2.2.4 Results and Discussion

The explosive composition of the materials used for this research are presented in Table 2.2-1. The percentage of each explosive compound were generally the same for all Comp B residue samples (HMX, 7 ± 1%; RDX, 58 ± 6%; TNT, 35 ± 6%) regardless of particle size or method used to generate microscale particles. The only exception would be the slightly lower fraction of RDX and higher fraction of TNT detected in the wet-milled material. The soot was composed predominantly of material that was insoluble in acetonitrile and/or not identifiable by HPLC, but also contained an unexpectedly high percentage of unreacted explosive compounds. Although present in these materials, the results with respect to HMX mass transfer kinetics were not examined in detail and are not presented.

The microscale particles smaller than 250 μm exhibited a sigmoidal cumulative volume percent vs. particle diameter size distribution (Figure 2.2-1). The smallest average size (defined as the size representing 50% of the cumulative volume) was observed for the Comp B detonation soot (24 μm). Wider size distributions were observed for the particles generated by dry physical attrition compared to those generated by aqueous weathering.

	Mean particle size (μm)[c]	Mass Fraction (%) [a,b]			Zeta-potential (ζ) (mV)
		HMX	RDX	TNT	
EODTECHDIV residues	NA[d]	0.08	0.52	0.40	ND[e]
Taylor residues	NA	0	0.59	0.41	ND
Dry-attritted residues					
20-45 μm	53 ± 9	0.08	0.62	0.30	-44.4 ± 2.9
45-125 μm	110 ± 5	0.07	0.60	0.33	ND
125-250 μm	155 ± 19	0.07	0.57	0.36	ND
Dry-milled undetonated Comp B	62 ± 29	0.05	0.58	0.37	-45.4 ± 0.7
Wet-milled residues	112 ± 46	0.06	0.47	0.47	-45.7 ± 4.5
Aqueous weathered residues	58 ± 12	0.07	0.63	0.30	-8.9 ± 6.6
Detonation soot[e]	24 ± 3	0.02	0.15	0.26	-24.7 ± 0.7

[a]Acetonitrile-insoluble material accounted for 1 to 2% of total mass extracted and was excluded when calculating explosive compound ratios except for detonation soot.
[b]Standard deviations were ± 3% of presented value (n=5).
[c]Particle size at which 50% of cumulative volume percent is reached based on Elzone particle size analyzer data from a minimum of five replicate analyses.
[d]NA, not applicable.
[e]ND, not determined.
[f]Residual 57% of mass was acetonitrile-insoluble matter.

Table 2.2-1. Mean size, explosive compound ratios, and zeta-potential of the Comp B materials used during this research.

Mass transfer coefficients for RDX, and TNT from the different Comp B materials are presented in Figure 2. The smaller sized materials possessed higher mass transfer coefficients for these compounds compared to the 1 mm sized residues (Figure 2.2-2A). These small particles clearly dissolved much faster than larger particles, and likely represent a source of rapid contaminant fluxes on ranges where they occur. Also insightful from Figure 2A is that the mass transfer coefficient for RDX is consistently greater than that of TNT, suggesting that RDX crystals within Comp B would dissolve more quickly than TNT even if both RDX and TNT had the same aqueous solubility. This result is likely due to the fact that RDX has a greater effective surface area for dissolution compared to TNT, as observed in our previous visualization studies Wang et al., (2011). However, TNT, due to its increased aqueous solubility, is more rapidly dissolved

from the particles, which is consistent with observations from previous dissolution studies (25, 52, 56). When data were normalized by the calculated surface area of each material (assuming a spherical geometry), the mass transfer coefficients of the microscale particles were not significantly different from those of the larger 1 mm particles (Figure 2B), with the exception of the aqueous weathered particles. Thus, the dissolution mechanisms for microscale particles appear similar to those observed for mm-sized particles, as the rate of dissolution scaled with the surface area of the particle. These results also are consistent with the visualization study of Wang et al. (2011), who observed that the microscale dissolution behavior of Comp B particles was similar to that of mm-sized Comp B particles. In this current work, we confirm these findings based on measured dissolved concentrations, which (to the best of our knowledge) is the first direct measurement of composition B microparticles. The mass transfer coefficients of physically attritted dry particles did not vary significantly when data were normalized for surface area, which indicates that the contribution of particle attributes such as roughness and shape factor can be considered minimal. Scaling of mass transfer parameters between particles of different sizes should be straightforward, which is also is consistent with our previous visualization study (Wang et al., 2011).

The notable exception to the dissolution behavior in Figure 2.2-2B is the aqueous weathered particles, which have mass transfer coefficients on the order of 5- to 20-fold higher than comparably sized particles. These data suggest that extended exposure to water prior to implementing the dissolution experiments may impact dissolution. The smaller particles (<45 μm) produced by dry-attrition methods were observed to clump together, and to float and resist wetting when added to aqueous solutions, indicating their surfaces were hydrophobic. This is in agreement with bulk analysis of Comp B, either recrystallized from acetone or prepared as a dried layer of colloids, indicated a hydrophobic surface with a contact angle of approximately 100° (56). The zeta-potential measurements presented in Table 1 indicate that the apparent absolute surface charge on the dry-attritted colloids was about 4-fold higher than that on the aqueous weathered colloids. The interpretation of zeta-potential measurements as they apply to hydrophobic, non-ionic surfaces was discussed by Joly et al. (2004) (21), and indicate that surfaces with higher absolute zeta-potential values are more hydrophobic (or more "non-wettable") than surfaces with lower absolute zeta-potential values. Applied to the current situation, this indicates that the dry-attritted particles were less wettable in comparison to the aqueous weathered particles, leading to lower mass transfer of the explosives from the particles during dissolution testing.

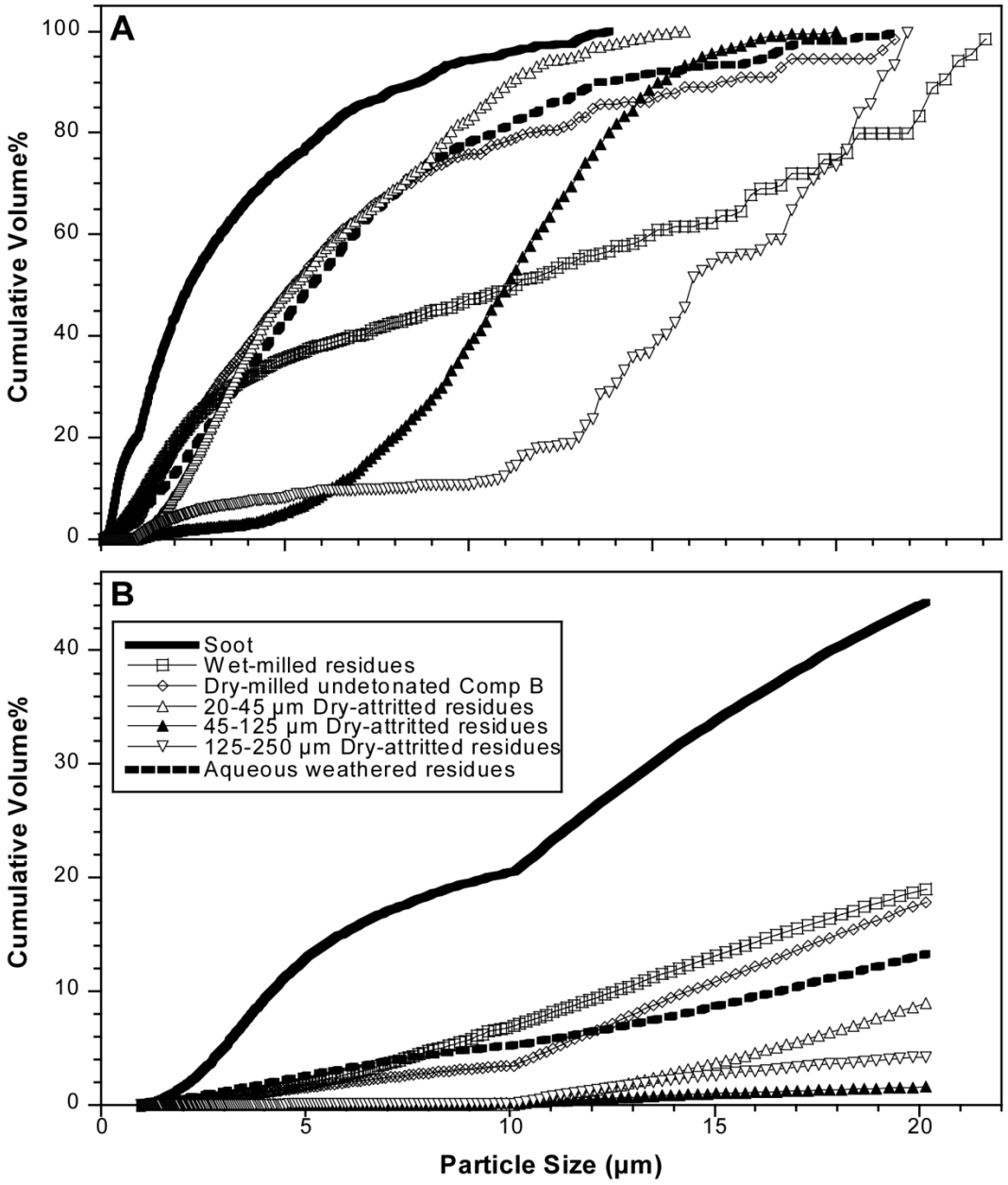

Figure 2.2-1. Cumulative volume percent vs. particle diameter of microscale Comp B materials used in this research.

Average values from a minimum of five replicate analyses shown, with an average relative standard deviation of ±35%. A) Full particle diameter range. B) Blow-up of diameter range 1 to 20 µm..

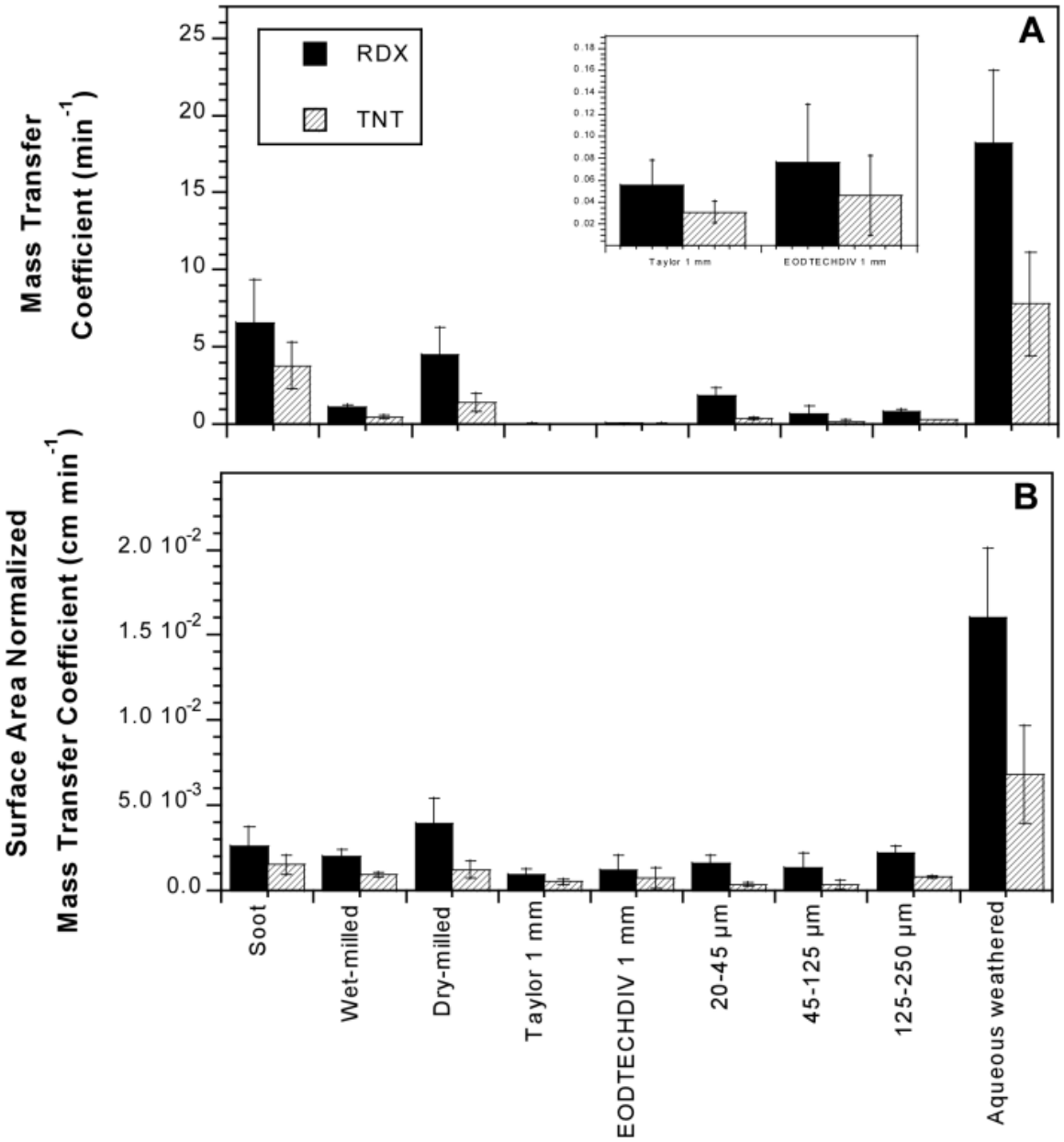

Figure 2.2-2. A) Mass transfer coefficients of microscale Comp B materials (blow-up of 1 mm data in inset). B) Surface area normalized mass transfer coefficients of microscale Comp B materials.

Extended dissolution testing performed on selected microparticles verified the conceptual model for longer times (Figure 2.2-3). The mass transfer coefficients obtained by regression to the short time (<600 minutes) dissolution data was used to extrapolate long time (1400 to 4500 min) dissolution data. It is noted that the model for the aqueous weathered particles did underpredict the data, particularly for RDX, at later times. A slight underprediction also was observed for the wet-milled particles. The substantial underprediction for the aqueous weathered particles was likely due to an underprediction of the mass transfer coefficient for the short time data, which may have been caused by the wettability issues described in the previous paragraph. The scatter in the data for the soot particles is likely due to the heterogeneity of these particles, as discussed in the following paragraph.

While the surface area-normalized mass transfer coefficients for a given explosive compound did not exhibit a significant relationship to particle size, the ratio of the RDX to TNT mass transfer rate constants did show evidence of size dependence, as shown for the dry attritted and dry milled Comp B detonation residues (solid symbols in Figure 2.2-4). The data in Figure 2.2-4 show that as the particle size decreases for dry attritted or milled particles, the mass transfer coefficient ratio for RDX to TNT increases (although overall TNT mass removal for a given particle remains greater than that of RDX for all particles examined). Implications of this finding suggest that the ratio of RDX:TNT dissolution in microscale particles is greater than that in comparable mm-sized particles, and that TNT may persist longer (relative to RDX) in microscale particles than in mm-sized particles. One plausible explanation for this observation is that the effective surface area for dissolution of RDX increases with decreasing particle size. This trend in mass transfer coefficient ratio was not observed for the soot particles, nor for the particles that were wet milled or aqueous weathered. Attempts to assess the TNT and RDX distribution in the soot particles using spectral imaging (56) indicated that there was likely unreacted intact Comp B comingled with the combustion products (data not shown), but it was also likely that TNT and RDX were also associated with the soot at a molecular level (e.g., adsorbed). The effects of particle wetting, as discussed previously for the aqueous weathered particles, is likely responsible for the absence of the trend observed in Figure 2.2-4 for these particles. The limited moisture associated with the wet milling process particles also may have altered the wettability or structure of the wet milled particles, subsequently impacting dissolution. A more complete explanation for these particles currently is not available.

These studies were performed with microscale Comp B particles produced by artificial means under controlled laboratory conditions. However, the observed results are expected to be relevant under field conditions. The dry-attritted particles are similar to what could reasonably be expected when incomplete low-order munition detonations occur, as well as when existing larger Comp B chunks are impacted by subsequent detonations (e.g., the chunks are either broken up by the shock wave, by shrapnel, or by contact with rocks and soil moved around in the secondary detonation). Over time, it can easily be seen that large chunks would be attritted to

sub-mm particles. Likewise, the aqueous weathered particles used in this research represent particles that would form over time when Comp B residues are in contact with water and agitated by some means (e.g., flow in a stream, wave action, detonations near a shallow puddle, etc.). Transport of Comp B residues during overland flow during heavy rainstorms likely generates microscale particles by a combination of processes.

2.2.4 Conclusions

In terms of the dissolution flux of the energetic particles, the results of this task suggest that microscale particles, in general, behave similarly to larger particles. One exception is that, compared to the dissolution of macroscale particles, the ratio of dissolved RDX to TNT flux is expected to increase as the particle size decreases. Also, the dissolution of microscale particles was shown to be very sensitive to wetting history, where microscale particles that are weathered under wetted conditions are expected to have a substantially greater dissolved flux of TNT and RDX compared to dry-attritted microscale particles and macroscale particles.

While the study of the formation and dynamics of microscale explosive residues is in its infancy, considerations of their contribution to the overall flux of contaminants on DoD training ranges should begin to be incorporated into fate and transport models. In a more general sense, this study indicates that the relative dryness of a range where detonation residues are being generated likely impacts mass transfer processes due to impacts on the surface wettability of microscale particles.

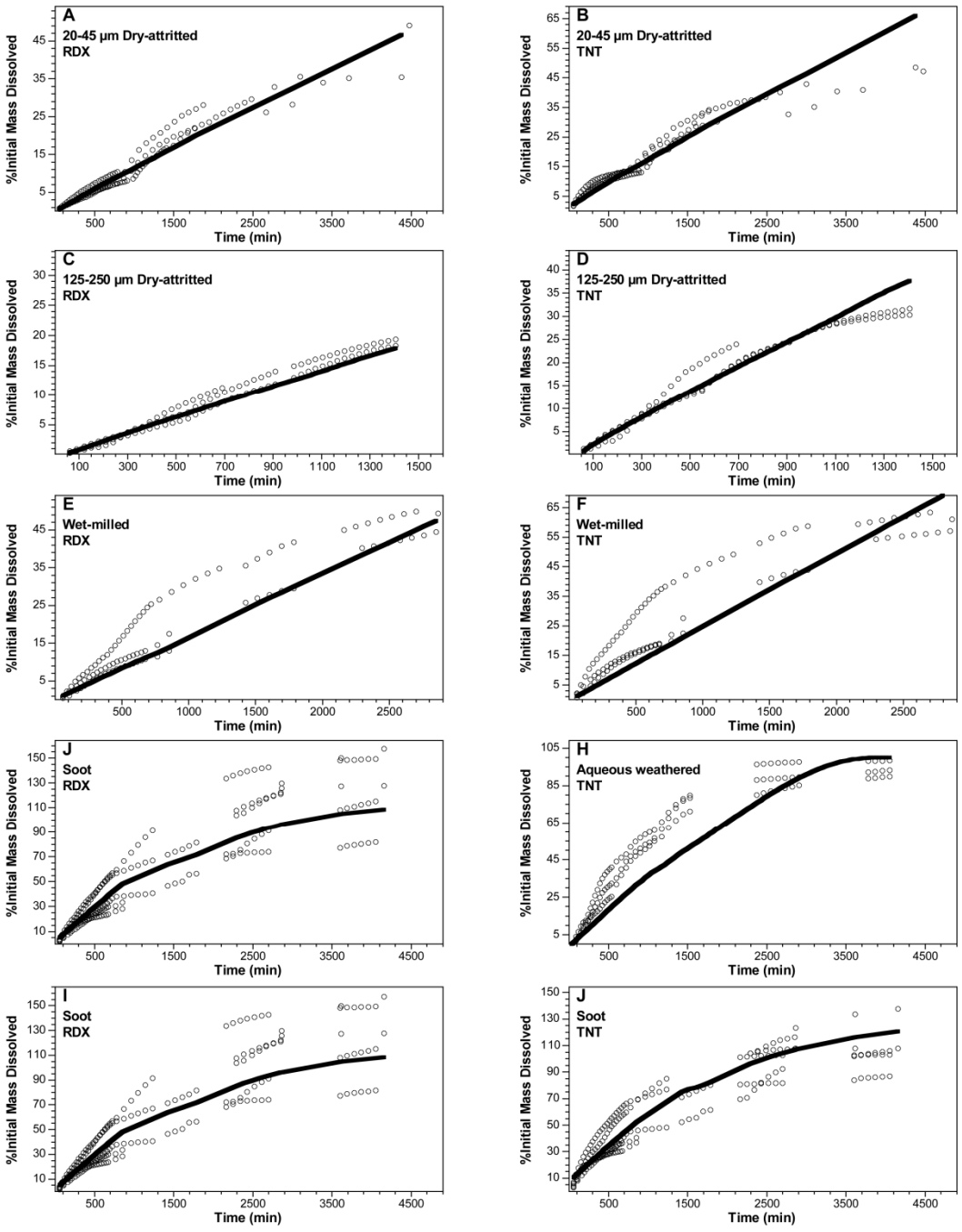

Figure 2.2-3. Experimental data (E) and model results (K) of dissolution of RDX and TNT from: (A, B) 20-45 µm dry-attritted; (C, D) 125-250 µm dry-attritted; (E, F) wet-milled; (G, H) soot; (I, J) aqueous weathered. Experiments were performed in duplicate or triplicate.

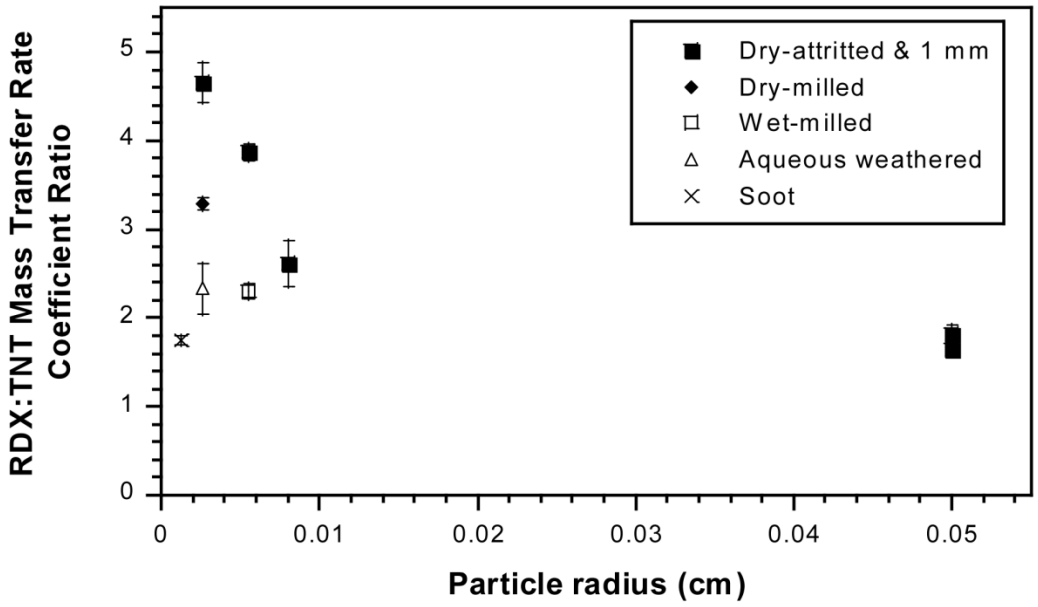

Figure 2.2-4. Ratio of TNT to RDX mass transfer rate coefficient for microscale Comp B materials as a function of particle size.

2.3 Task 3 – Transport of mm-Sized and Microscale Composition B Residues in Porous Media

The results summarized in this section here have been published:

> Fuller, M. E., C. E. Schaefer, C. Andaya, and S. Fallis. 2014. Transport and dissolution of particulate Composition B through porous media. Chemosphere 107: 400-406.

2.3.1 Goal

The goal of this task was to examine the transport and dissolution of microscale Comp B particles in porous media under unsaturated flow conditions, and to compare their behaviour with mm-sized residues.

2.3.2 Introduction

While a general understanding of the environmental fate and transport of explosives has evolved, there is a recognized need to better define the contaminant source terms and the transport processes by which detonation residues and component explosives are distributed in the environment (47). This is especially true regarding the generation and fate of microscale and/or colloidal particles, which may form an important link between larger surface detonation residues and dissolved explosives in groundwater. Our previous research using micro-scale Comp B particles demonstrated that these very small particles are likely a fast-dissolving source term on contaminated ranges, with RDX and TNT mass transfer coefficients being inversely related to particle diameter (15). Additionally, microscale particles derived from larger detonation residues through aqueous weathering exhibited mass transfer coefficients that were up to 20-fold higher than similarly sized particles derived through dry-attrition. The increased dissolution of the aqueous weathered residues was attributed to changes in the hydrophobicity (or wettability) of the particles after prolonged exposure to water, and may imply larger fluxes of dissolved explosives from small residues entrained in wet soil.

In an effort to more closely simulate the environmental fate of Comp B residues on ranges, the focus of this task was to examine the potential transport of microscale particles in unsaturated porous media, and the effects on dissolution.

2.3.3 Methods

Energetic Residues. Sources of Comp B residues, and the production and characterization of microscale Comp B is described in detail in Task 2. Briefly, large cm-sized residues were

manually reduced to mm-sized material, which then underwent further dry physical attrition and sieving processes to produce microscale particles in the range of 20 to 45 μm.

Transport and dissolution of microscale Comp B. Transport experiments were performed in small scale unsaturated sand columns. Columns were constructed using two polypropylene syringe barrels (26 mm inner diameter, Norm-Ject A50, Henke-Sass, Wolf GmbH, Tuttlingen, Germany) that were joined together. A stainless steel mesh was placed at the bottom of the column to retain the sand in the syringe (80 mesh, 180 μm opening). Columns were packed with approximately 188 g of play sand (>40 mesh, mean particle size 425 μm) to achieve a final sand depth of 22 cm with an approximate bulk density of 1.6 g cm^{-3}. A 16 gauge needle with the point removed was attached to the syringe outlet. The porosity was calculated at 38%, resulting in a column pore volume of approximately 50 ml, after taking into account the volume of the syringe below the mesh at the bottom of the syringe and the volume in the needle attached to the syringe outlet. Sorption of HMX, RDX, and TNT onto the sands was negligible (K_d <10^{-6} kg l^{-1}, data not shown).

Flow of ARW to the columns was provided using a programmable syringe pump (New Era Pump Systems, Model NE-1600, Wantagh, NY, USA). To allow for extended durations of continuous flow, three syringes were connected in parallel for each column. Influent lines were teflon, with an outer black covering to prevent any photodegradation. Columns were positioned above a Spectra/Chrom CF-2 Fraction Collector (Spectrum Chromatography, Houston, TX, USA) to allow collection of discrete effluent volumes.

An initial period of equilibration was performed, during which at least one pore-volume of ARW was passed through the columns at a rate of 5 ml h^{-1}, with the fraction collection at 60 min intervals. This flow rate was equivalent to precipitation falling at a rate of 0.94 cm h^{-1} (0.34 inches h^{-1}). After confirming steady-state flow (i.e., flow in = flow out), Comp B residues were applied evenly across the sand at the top of the column. The residues were then covered with 5 g of additional sand, and a glass microfiber filter (5 μm pore size) was placed on top of the sand to promote even distribution of solution. Flow remained at 5 ml h^{-1}, with fractions collected initially at 30 min intervals for the first few hours, then at 90 min intervals thereafter. The fraction collector was placed within a box to minimize both evaporative losses and any possible photodegradation.

Fractions were removed from the collector on a regular basis. Each fraction was labeled, then the weight was recorded in order to monitor effluent volume. After removal from the fraction collector, tubes were covered with parafilm and aluminum foil to prevent evaporation of effluent and photodegradation of explosives prior to processing. Effluent samples were analyzed for both total (particulate + dissolved) explosives and dissolved explosives compound concentrations. Soluble concentrations were measured after passage through a 0.45 μm glass microfiber syringe

filter, followed by HPLC analysis. Total concentrations were determined by mixing 500 µl of well-mixed, unfiltered sample with 500 µL of acetonitrile (to assure complete Comp B particle dissolution) in an HPLC vial and shaking for at least 18 h at room temperature (125 rpm) prior to HPLC analysis.

At the end of transport experiments, the sand was removed from the syringe casing in multiple mm intervals. Samples were transferred to septa cap glass jars (60 ml), weighed, and dried at 50°C overnight. After recording the dry weight, the sand was extracted for at least 18 h in acetonitrile using an ultrasonic water bath overnight. Samples were then shaken for several hours at room temperature. Extracts were settled then clarified by passage through a 0.45 µm Millex-LCR teflon syringe filter unit (Millipore, Bedford, MA, USA) prior to HPLC analysis (see below). Particulate concentrations of explosives in each interval (in units of mg kg^{-1}) were calculated according to Equation S1 in Supplemental Information, which takes into account any dissolved explosives that would have been present in the sand in the residual water that was present before the sand was sampled. This sampling also allowed for determination of the average moisture content and saturation of the column. To estimate the average saturation during flow, the volume of water that drained between the time the flow ceased and the column sand intervals were collected (5 mL) was added to the measured mass of water in the column, resulting in an average saturation of 60% during unsaturated flow.

Calculation of particulate explosive concentrations within the sand matrix.

Given the following:

M_i = mass of sand interval (kg)

W_i = volume of water in sand interval (l)

C_{eff} = explosive compound concentration in effluent at experiment termination (mg l^{-1})

C_{tot} = explosive compound concentration in sand interval (mg kg^{-1})

The particulate explosive concentration in a given sand interval, C_{part}, is calculated as:

$$C_{part} = [(C_{tot} \times M_i) - (C_{eff} \times W_i)]/M_i \quad (1)$$

2.3.4 Results and Discussion

Dissolved concentrations of HMX, RDX, and TNT eluting from microscale and mm-sized Comp B in the sand columns during column experiments are shown in Figure 2.3-1. Dissolved concentrations of explosives were significantly lower for the mm-sized residues than from the microscale residues. HMX and RDX exhibited similar behavior, therefore only the RDX and TNT results will be discussed in depth. Dissolved RDX concentrations emanating from the microscale Comp B sources were approximately 10-times greater than those from the mm-sized sources; for TNT, dissolved concentrations of TNT emanating for the microscale Comp B

sources were approximately 5-times greater than TNT concentrations emanating from the mm-sized Comp B sources.

Applying our previously developed particle dissolution model and numerical solution approach (Fuller et al., 2012) to the current dissolution data set, average lumped mass transfer coefficients for RDX and TNT in the microscale Comp B columns are 0.065 and 0.047 min^{-1}, respectively. In the mm-sized Comp B columns, the average lumped mass transfer coefficients for RDX and TNT are 0.00049 and 0.00055 min^{-1}, respectively. While differences in the experimental system and source emplacement between the current study described herein and our previous work (Fuller et al., 2012) make comparison of the absolute values of the intrinsic mass transfer coefficients of little value, valuable insight can be gained by comparing the dissolution behavior

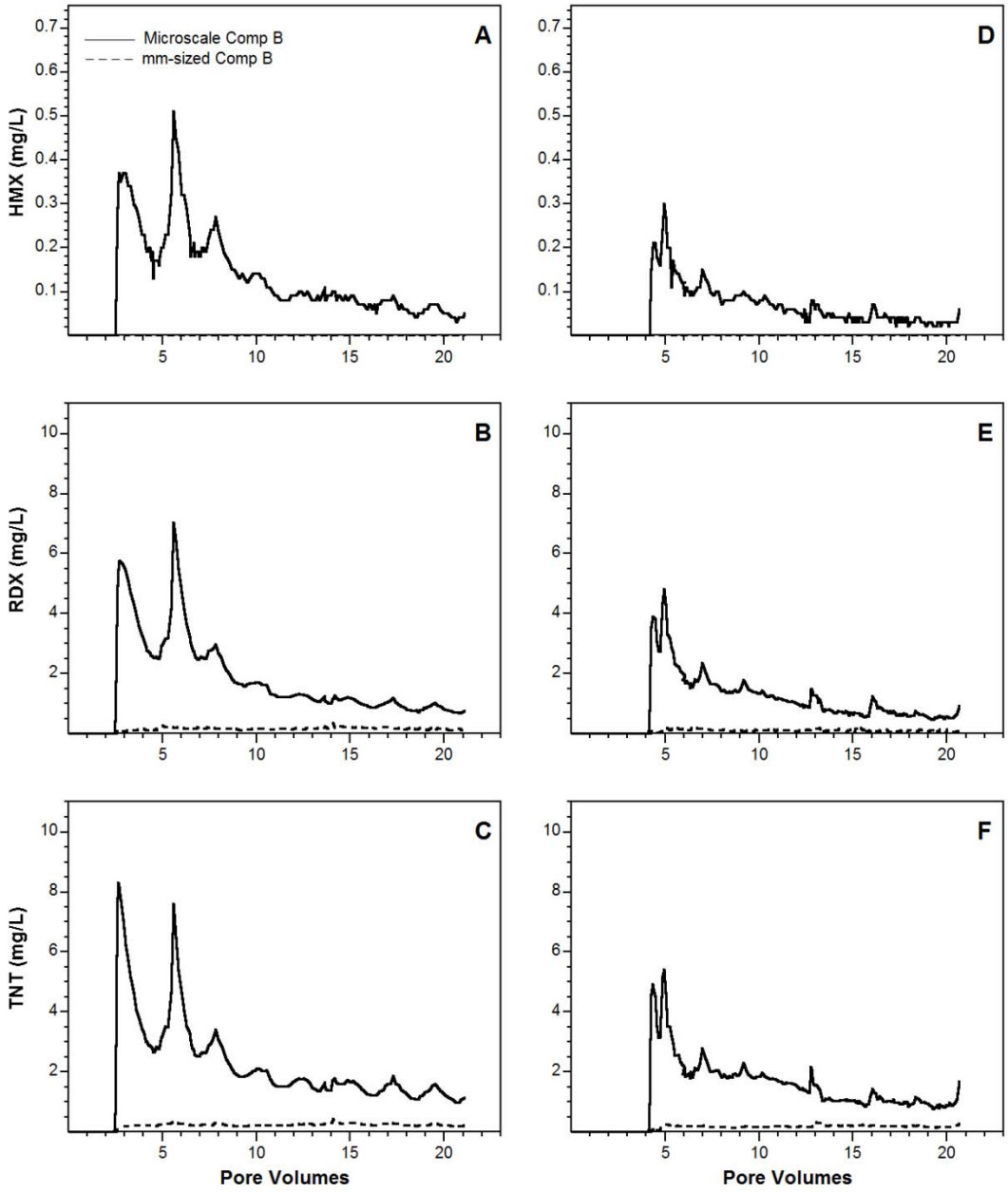

Figure 2.3-1. Dissolved concentrations of HMX (A, D), RDX (B, E), and TNT (C, F) during duplicate column experiments comparing microscale (□) and mm-sized (- - -) Comp B residues.

Residues were added to the first experiment at 2.1 pore volume and at 3.9 pore volumes for the second experiment.

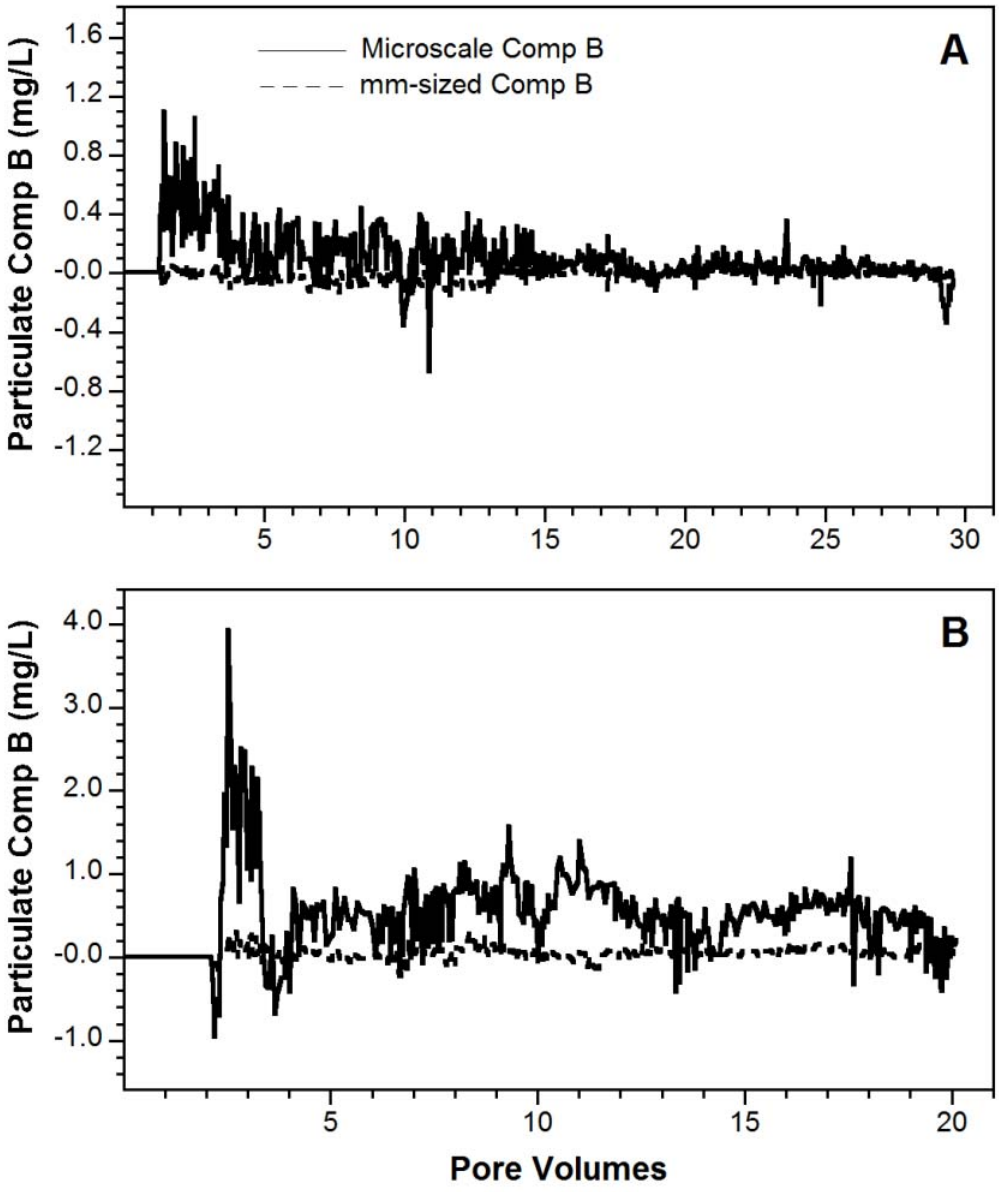

Table 2.3-2. Particulate Comp B detected in the effluent during two duplicate sand column experiments.

Residues were added to the first experiment at 2.1 pore volume and at 3.9 pore volumes for the second experiment.

between the microscale and mm-sized particles in each set of experiments. The intrinsic mass transfer coefficients for RDX were approximately 30-times greater for microscale particles compared to mm-sized particles in our previous studies. In our current work, the intrinsic mass transfer coefficient for RDX is approximately 130-times greater for microscale particles compared to mm-size particles. Similarly, for TNT, the intrinsic mass transfer coefficients for microscale particles previously were shown to be approximately 14-times greater than for mm-sized particles, while our current work shows that microscale particles have an intrinsic mass transfer coefficient that is 85-times greater than that measured for mm-sized particles.

One potential explanation for the enhancement in dissolution of the microscale Comp B relative to the mm-scale particles observed in this current study (i.e., an explanation for why the ratio of the intrinsic mass transfer coefficients for microscale:mm-scale particles was greater in our current study compared to our previous study)is that in the sand column experiments, colloidal microscale particles were able to migrate into the sand column (even if only a relatively short distance), thereby providing an extended zone of dissolution, and resulting in increased contact time between the flowing water and microscale particles. This ultimately increased dissolved concentrations of RDX and TNT relative to mm-sized sources, resulting in an increase in the observed intrinsic mass transfer coefficient. Migration of mm-sized particles into the sand would not occur (or, occur much less than the microscale particles), effectively limiting dissolution of the mm-sized particles to the surface of the sand column, with a much shorter contact time.

An examination of the HPLC data to detect putative particulate Comp B eluting from the columns was performed to assess potential impacts of microscale particle migration in the columns as a potential explanation of the differences described in the above paragraph. Particulate Comp B was defined as the difference between the total explosive concentration upon addition of acetonitrile to the sample and dissolved explosive concentration after passage of the sample through a 0.45 μm glass microfiber filter (to remove any particulates). Assessment of particulate Comp B concentrations emanating from the sand columns indicated that there was some colloidal migration through the columns, particularly for the columns to which microscale residues were applied (Figure 2.3-2). Most of the particulate Comp B elution was observed during the first 15 to 20 pore volumes. While there was considerable variability in the data, particulate Comp B contributed from <1% up to 20% of the total mass eluting in discrete fractions from the columns. For the replicate columns receiving microscale residues, the average total percent of the initial RDX and TNT applied to the column which eluted as particulates was 0.4% and 1.4%, respectively. The same values for the replicate columns that received mm-sized residues were <0.1% and 0.6%, respectively. These results clearly demonstrate that colloidal migration occurred in the experimental columns, particularly for the microscale particles. While the mass fraction of particulates relative to the total RDX and TNT mass that migrated through the column was small, it is plausible that the impacts of this particulate migration (due to potential retention in the sand column) could be responsible for the increased dissolution

observed for the microscale particles, as discussed in the previous paragraph. We note that further research is needed to assess the extent of particulate Comp B migration in complex soils in real environments.

While the data shown in Figure 2.3-2 demonstrate that colloidal Comp B mass exited the column, straining and/or filtration processes likely caused the retention of Comp B colloidal mass within the column. Data analysis performed to distinguish the proportion of the RDX and TNT mass retained in the column as particulates is shown in Figure 2.3-3. Results indicate that the column to which the microscale Comp B source was applied had particulate RDX and TNT through a considerable portion of the column (top 1/3 to 1/2 column length, or topmost 50 mm). The column which received the mm-sized Comp B exhibited much lower levels of particulate mass, but still indicated that a trace amount of colloidal Comp B was generated and transported during the application of ARW to the column. The concentration trends along the length of the column are slightly different for RDX and TNT. RDX, for both the microscale and mm-sized particles, shows a dip in particle concentration beyond 25 mm depth, then exhibits a slight increase with depth. TNT exhibits a more uniform trend across the depth of the column, at least beyond 25 mm. The reason for this difference in behavior between RDX and TNT is unclear, but may be due to preferential dissolution of RDX over TNT in trapped microscale particles within the column. Also, the original Comp B is not a fully homogeneous mixture of RDX and TNT at very small scales, but can be thought of as RDX crystals embedded in a TNT matrix (Dr. Susan Taylor, personal communication). This could result in the formation of very small particulates that are enriched in either TNT or RDX, as opposed to particles with the same TNT:RDX ratio of Comp B. Further study regarding the dissolution of microscale particles entrapped in porous media is required to attain improved insight into this process.

The mass of entrained colloidal particles below a depth of 25 mm in the sand column (i.e., a depth at which the data in Figure 3 is assumed to represent true colloidal mass and not mass from the original applied Comp B) as a percent of the applied mass was quite low (Table 2.3-1). However, the weathering and transport of the microscale Comp B resulted in roughly 10 times more colloidal Comp B mass entrained in the sand than the corresponding weathering and transport of the mm-sized Comp B.

These results are consistent with our effluent and residual explosives mass distribution discussed above. This finding also supports our hypothesis concerning the observed relative increase in RDX and TNT dissolution in the microscale Comp B compared to the mm-sized Comp B sources. RDX and TNT colloids present in the column are expected to serve as additional sources for dissolution as water percolated through the column, effectively increasing the contact time between particulate Comp B sources and infiltrating rain water. Thus, even limited migration of colloidal Comp B particles into the porous medium would likely result in increased aqueous phase TNT and RDX concentrations due to the higher mean surface area of these

colloidal residues, combined with a significant increase in contact time between the particles and infiltrating water. Additionally, as the colloidal particles are likely to migrate into preferential flow paths, the dissolved explosives are more likely to be rapidly transported to underlying groundwater.

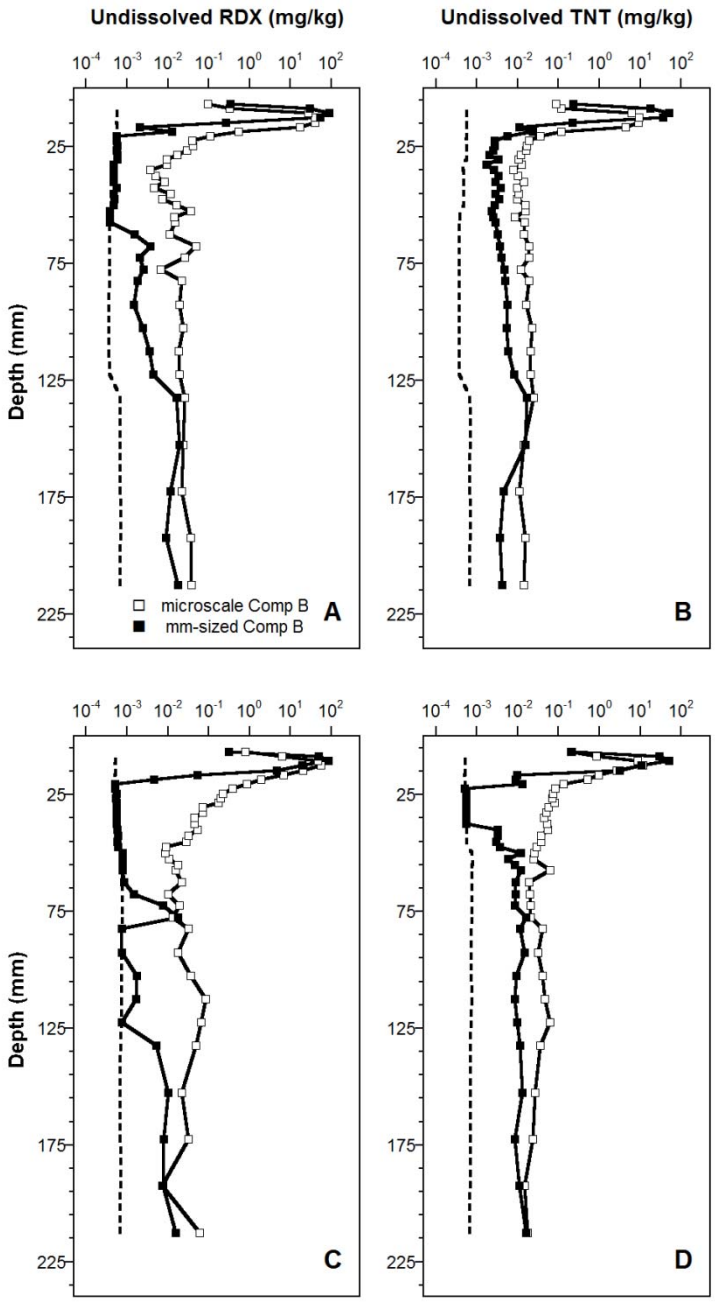

Figure 2.3-3. Particulate RDX (A, C) and TNT (B, D) as a function of depth during duplicate column experiments comparing microscale (G) and mm-sized (B) Comp B residues.

Detection limits are represented by dashed lines (---); datapoints less than the detection limit are plotted at the detection limit. NOTE: Log scale used on x-axis.

		20-45 µm				0.5-1.0 mm			
		HMX	**RDX**	**TNT**	**SUM**	**HMX**	**RDX**	**TNT**	**SUM**
Experiment 1	Mass applied (mg)	1.9	15.5	7.6	25.0	2.10	12.44	10.43	24.98
	Mass in sand (mg)	1.3	11.0	2.6	14.9	1.8	14.9	9.1	25.7
	Mass in effluent (mg)	0.3	3.3	4.8	8.4	0.0	0.3	0.9	1.1
	Mass recovered (mg)	1.5	14.4	7.4	23.3	1.8	15.1	9.9	26.8
	%Recovery	**82**	**93**	**98**	**93**	**84**	**121**	**95**	**107**
	Entrained colloidal mass[a] (% of applied mass)	0.22	0.26	0.49	0.96	0	0.05	0.03	0.09
Experiment 2	Mass applied (mg)	1.9	15.6	7.6	25.1	1.89	15.58	7.61	25.08
	Mass in sand (mg)	1.4	13.8	2.6	17.8	1.7	14.9	8.8	25.4
	Mass in effluent (mg)	0.1	2.0	3.2	5.4	0.0	0.1	0.5	0.6
	Mass recovered (mg)	1.6	15.8	5.9	23.2	1.7	15.0	9.3	26.0
	%Recovery	**84**	**101**	**77**	**93**	**88**	**96**	**122**	**104**
	Entrained colloidal mass[a] (% of applied mass)	0.72	1.19	2.97	4.88	0	0.07	0.39	0.46

[a]Cumulative colloidal explosive mass entrained in sand column from depth interval 25 mm to 225 mm. Estimated error in the values above, based on analytical and other measurement errors, are as follows: mass applied, 5%; mass in effluent, 11%; mass in sand, 17%; total mass recovered, 20%, entrained colloidal mass, 21%

Table 2.3-3. Mass balances of explosive compounds for the two column transport experiments.

2.3.4 Conclusions

The findings of this research have several implications for understanding the fate of energetic residues on DoD test and training ranges. First, the fact that particulate explosives were observed to migrate a moderate distance into the sand columns, and were also detected in the column effluent (although to a lesser degree), indicates that these small particles are likely mobile in soil. After their production, either at the time of detonation, or through weathering of larger residues, these particles likely disperse and create a larger source term for dissolved explosives in response to precipitation events or percolating rainwater. While these findings will assist with modeling efforts aimed at describing the behavior of explosives in the environment, more information is still needed regarding the production and movement of microscale residues under field conditions.

2.4 Task 4 – Precipitation-driven Production of Microscale Particles from Macroscopic Composition B Residues

The results summarized in this section here have been published:

> Fuller, M. E., C. E. Schaefer, C. Andaya, and S. Fallis. 2015. Production of particulate Composition B during simulated weathering of larger detonation residues. Journal of Hazardous Materials 283: 1-6.

2.4.1 Goal

The goal of this task was to examine the actual potential for the production of microscale particles of Comp B during the weathering of larger cm-sized residue chunks under realistic simulated precipitation.

2.4.2 Introduction

While the production of small residues during detonations has been documented by previous research (49) and during this project, no attempts to document production of miscroscale particles during aging of larger detonation residues have been reported. During simulated and outdoor weathering, larger residues have been observed to fragment or crumble (51, 52). The work performed during Task 1 of this project demonstrated that single Comp B particles can break into smaller and smaller pieces as the representative explosives progressively dissolve. Therefore, it is likely that both micro and macro desintigration of detonation residues occurs, resulting in the production of microscale particles during precipitation-driven weathering of larger residues. This task was designed to document this process both qualitatively and quantitatively under realistic simulated precipitation.

2.4.3 Methods

Energetic Residues. Sources of Comp B residues were as described in detail in Task 2.

Production of microscale particles during drip-wise weathering. A rain drop simulator was constructed as shown in Figure 2.4-1 to perform initial proof-of-concept screening experiments of Comp B weathering. A stainless steel screen filter unit (100 mesh size, 150 μm screen opening) was connected to the bottom of a length of clear plastic tube (polyethylene terephthalate (PETG), 1" OD x ¾" ID). Levels were fastened to the sides of the tube to ensure consistent drip placement from a drip generator (10 ml syringe with a 20 gauge needle) in the

Photograph of the Comp B residues on the support screen at the bottom of the drip-wise aging apparatus.

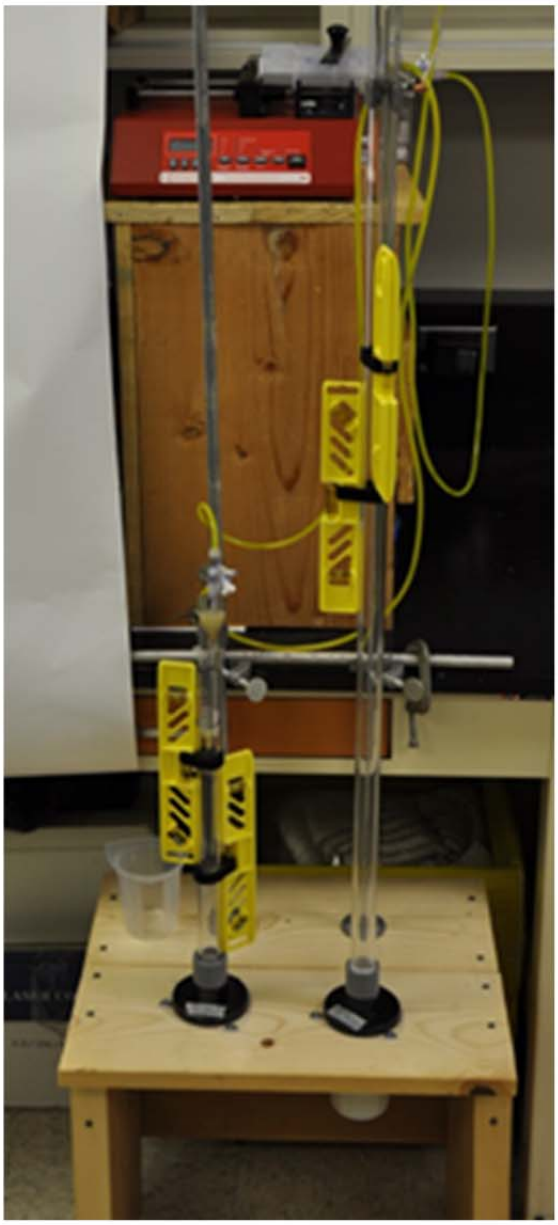

Photograph of the drip-wise aging apparatus, showing the 30 cm (left) and the 1 m (right) long tubes.

Figure 2.4-1. Photograph of the experimental setup for the drip-wise aging of Composition B residues.

middle of the plastic tube and onto the residues positioned in the center of the stainless steel screen filter unit. A programmable syringe pump (New Era Pump Systems, Model NE-1600, Wantagh, NY, USA) and a Norm-Ject 60 ml syringe (Air-Tite, Part No. AL50, Virginia Beach, VA, USA) was used to supply flow of ARW to the to the syringe through a length of Tygon tubing, which then dripped onto the residues via gravity. The drip mass was determined by collecting 20 drops into a tared pan, measuring the collected mass, and dividing by the number of drops, resulting in an average of 18.7 ± 0.3 mg (n = 5) per drop. Assuming drops were perfect spheres, the average drop diameter was 3.9 mm.

To begin the experiment, chunks of explosive residues were placed in the middle of the steel screen filter unit, and ARW was applied in 50 ml aliquots over a 20 min (actual application averaged 150 ml/h, equivalent to a rainfall rate of 29 cm h^{-1} (11 in h^{-1})). Composition B detonation residues from EODTECHDIV and China Lake (15) were examined during these experiments. The distance between the drip generator's needle and the residues ranged from 30 to 100 cm, resulting in calculated drop instantaneous velocities (v_i) of 2.4 and 4.4 m s^{-1}, respectively, according to Equation 1 (ignoring air resistance).

$$v_i = \sqrt{2\,g\,\mathrm{d}} \qquad (1)$$

where g is the acceleration due to gravity (9.8 m s^{-2}) and d is the distance traveled (in meters).

The effluent from the simulator was collected in 60 ml pre-rinsed jars (either glass or polypropylene) with white polypropylene caps (with and without Teflon liners) (SKS Bottle & Packaging, Watervliet, NY, USA). Each sample was labeled, and the weight was recorded in order to monitor effluent volume. Testing occurred for approximately 4 h each day, with samples remaining undisturbed in the testing apparatus without any ARW flow at night between workdays and over weekends.

Samples were analyzed to determine both total and dissolved explosives compound concentrations. Processing was done immediately after sample collection to minimize further dissolution of any particulates in the sample. Soluble concentrations were measured after passage through a 0.45 µm glass microfiber syringe filter, followed by HPLC analysis. Total concentrations were determined by mixing 500 µL of well-mixed, unfiltered sample with 500 µL of acetonitrile in an HPLC vial and shaking for at least 18 h at room temperature (125 rpm) prior to HPLC analysis. The particulate explosive concentration was calculated by subtracting the dissolved concentration from the total concentration. The remaining samples in the glass jars were then examined with a particle size analyzer. HPLC and particle analytical details are presented below in sections 2.4 and 2.5, respectively.

Production of microscale particles under artificial precipitation. Microscale particle formation during weathering was further examined using an apparatus that more closely simulated actual precipitation in terms of rainfall intensities, as well as drop size and drop

velocity. The rainfall simulator is shown in Figure 2.4-2. ARW was pumped through PVC tubing (Clearflex 70, ¾" OD x ½" ID, 1/8" wall, Finger Lakes Extrusion, Canandaigua, NY, USA) from a large reservoir through a centrifugal transfer pump (SHURflo Model 4UN55, Cypress, CA, USA) and then through a multi-stage booster pump (Model 5NYC0, Dayton Electric Manufacturing Co., Lake Forest, IL, USA) and back into the ARW reservoir. A tee and valve in the loop allowed the flow to be diverted through an in-line capsule filter (AquaPrep 600, 0.45 μm pore size, Pall Corporation, Port Washington, NY, USA), a pressure gauge, and a second in-line capsule filter before going through the spray nozzle and entering the testing chamber. Spray nozzles were purchased from Lechler (St. Charles, IL USA) and were selected to allow a range of precipitation intensities to be generated (see details in Table 2.4-1). The flow to the testing chamber was adjusted by opening or closing the valve until the pressure required for a given spray nozzle was achieved, based on information provided by the spray nozzle manufacturer (22).

The testing chamber consisted of a catchment basin (cut 55 gallon plastic drum) encircled by a plastic curtain and equipped with a drainage outlet and valve assembly. The spray nozzle was suspended on a ring stand inside the basin. Comp B residues were placed on stacked 4" (10 cm) diameter stainless steel screens (top: 30 mesh (600 μm opening); bottom: 100 mesh (150 μm opening) inside a 4" x 2.5" (10 cm x 6.4 cm) PVC reducing coupling. The spray nozzle was positioned 30 cm above the Comp B residues on the screens. ARW reaching the residues via the spray nozzle drained into 355 ml pre-rinsed glass jars, while overspray was directed into the basin and out to the drain. Comp B chunks (0.25- to 1-cm size range) were arranged on the screen with no contact between chunks (see representative arrangement in Figure 2.4-2). The Comp B mass and the area of the screen covered by the Comp B residues during duplicate spray experiments were 8.61 g / 16% and 8.68 g / 15%, respectively. Multiple applications of artificial precipitation were performed for each experiment (e.g., 1 application = 1 jar of collected effluent). Several precipitation intensities were examined (see Results), but the duplicated experiments were performed using the nozzle that delivered strong to very strong precipitation (defined by Lechler as a rainfall rate of 1.4-5.0 mm h^{-1} m^{-2}). Residues were allowed to drain and/or dry overnight and over weekends during a given experiment. The collected effluent was analyzed for dissolved and particulate explosives concentrations (triplicate subsamples per jar), as well as for particle size distribution, as described for the drip-wise weathering experiment in section 2.2 above.

Particle analysis. Particle size, counts and volume was determined using a Micromeritics, Elzone II 5390 particle analyzer (Norcross, GA, USA) A volume of concentrated NaCl solution (25%, w:v) was added to each sample to reach a solute concentration of ~2% (w:v), resulting in an average conductivity of 3.4 ± 0.2 S m^{-1}. Analysis for the majority of samples was performed for total particle counts versus particle size and total particle volume versus particle size using the Elzone's 30 μm orifice, which effectively allowed detection of particles in the size range

from 0.9 μm to around 25 μm. A few analyses were also performed using the Elzone's 380 μm orifice, which allowed detection of particles in the size range from 8 μm to 250 μm. Tests were run in triplicates, and samples were diluted with an ARW/NaCl solution and re-analyzed if coincidence levels exceeded 2.5%. Samples with very high particle concentrations were diluted into 2% NaCl solution saturated with Comp B (to prevent particle dissolution) prior to analysis. Elzone analysis of the incoming ARW was performed periodically to determine background particle counts and particle volume. For the drip-wise experiments, the average background values were $2.3 \pm 1.2 \times 10^4$ particles ml^{-1} and $4.8 \pm 2.4 \times 10^4$ total particle volume mL^{-1} (n=11). The corresponding values for the spray experiment were $6.2 \pm 4.5 \times 10^4$ particles ml^{-1} and $1.8 \pm 1.0 \times 10^5$ total particle volume mL^{-1} (n=40). Results reported here reflect sample data after the average background values were subtracted. The sampling and analytical error associated with the Elzone data was approximately 15%.

Photograph of the Comp B residues on the support screen in the spray aging apparatus.

Close-up of the spray chamber, showing the spray nozzle (blue, top) and the screen support holding the Comp B residues (bottom).

Figure 2.4-2. Photograph of the experimental setup for the spray aging of Composition B residues.

		Precipitation Simulation Parameters (based on radar and other field measurements)			Drop mass	Terminal Velocity	Impact Energy
		Intensity		Drop size			
Precipitation Class	Nozzle ID	mm/h*m^2	L/min*m^2	D_{V50}, mm	mg	m/s	µJ
Light to moderate	460.448.30.BA	1.5-3.9	0.025-0.065	1.2	4.2	9.9	205
Moderate to strong	422.566.5E.BC	3.9-14	0.065-0.230	1.5	22.4	12	751
Stong to very strong	460.688.30.BC	14-50	0.230-0.830	1.8	14.1	14	2200

Adapted from:

Keck, D., Kircher, D., Muff, P., 2005. Simulation of rainfall with nozzles by means of radar reflectivity. Lechler GmbH, Metzingen, Germany, p. 18.

van Mook, F.J.R., 2003. Driving Rain on Building Envelopes. Volume 69 in Bouwstenen series / Faculty of Architecture, Planning and Building. Technische Universiteit Eindhoven, Eindhoven, Netherlands.

Table 2.4-1. Drop size and drop velocity data used as a basis for selecting the nozzles for the spray aging experiments.

Explosives analysis. The concentrations of the explosives and their breakdown products were monitored during incubation using HPLC according to a modified EPA Method 8330 (www.epa.gov/epawaste/hazard/testmethods/sw846/pdfs/8330a.pdf) using a Dionex 3000 Ultimate HPLC with a Agilent Zorbax Bonus-RP column (4.6 x 75 mm, 3.5 µm particle diameter), variable wavelength detector (254 nm), and a photodiode array detector collecting peak spectral data. The mobile phase was 50:50 methanol:0.2% (v:v) trifluoroacetic acid in water at a flow rate of 1 mL min^{-1}. The column temperature was 33°C. The practical quantitation limit was approximately 10 µg L^{-1}. The combined sampling and analytical error associated with the HPLC data was approximately 15%.

2.4.4 Results and Discussion

Our previously published results provided indirect evidence that aqueous weathering of mm-sized Comp B residues in porous media resulted in the production and transport of microscale particles (14). Others have visually observed the breakdown and disintegration of cm-sized Comp B residues under simulated (52) or in situ precipitation (55), but the current results are the first time that production of microscale particles during simulated precipitation-driven weathering of Comp B residues has been directly quantified.

Production of particulates during drip-wise residue weathering. Figure 2.4-3 shows the concentration of particulate Comp B (mg/L) in the effluent of the raindrop simulator (total minus soluble explosives concentration) as a function of volume of ARW applied to detonation residues from EODTECHDIV. Figure 2.4-4 shows the total particle counts (upper graph) and the total

particle volume (lower graph) per milliliter of effluent from the same experiment. The dashed line represents when the drip distance was increased from 30 cm to 100 cm. Calculated particulate Comp B concentrations in the effluent based on total and soluble concentrations indicated several small peaks of eluting particles when the drop distance was 30 cm, and a marked increase in both the frequency and amount of particulate Comp B when the drop distance was increased to 100 cm (Figure 1). The particle concentration and total particle volume as measured by the Elzone instrument dramatically increased, decreased slightly to a constant value, then exhibited an uptick when the drip distance was increased (Figure 2.4-3). The mean particle diameter of Comp B detected in the samples during the drip experiments was 7.6 μm (n = 180, Figure 2.4-5). The mean particle diameter was based on data collected with the Elzone 30 μm orifice (0.9 to 25 μm detection range), and therefore does not take into account any larger particles than may have been produced. No analyses with the larger 380 μm orifice were performed for these drip experiments.

Results from a second experiment using detonation residues from China Lake are presented in Figures 2.4-6 and 2.4-7. The calculated particulate Comp B concentration showed a similar pattern as in the first experiment, except that the increase in the frequency and amount of particulates was delayed relative to the timing of the increase in drip distance (Figure 2.4-6). The number of particles and total particle volume exhibited a slow steady increase to an apparent plateau, with another steady increase followed by a slow decline and eventual plateau when the drip distance was increased (Figure 2.4-7).

These drip experiments provided proof-of-concept data that supported the idea that microscale particles could be produced by the impact of water on detonation residues. In both experiments, approximately 10% of the initial residue mass was recovered in the effluent, 30% of which was represented by particulate Comp B. Given the average drop mass 19 mg and the instantaneous velocity of drops originating from 0.3 m and 1 m right before impact of 2.4 and 4.4 m s^{-1}, respectively, the energy deposited by drop impacting the Comp B would range from 54 to 181 μJ (assuming no vertical movement of the particle in response to the drop). This increase in deposited energy corresponded to an observed increase in the particle production rate. For comparison, real world precipitation has been measured to have instantaneous (or terminal) velocities ranging from 10 to 14 m s^{-1}, and deposited energy of 305 μJ for light rain to 2200 μJ for heavy rain (Table 2.4-1).

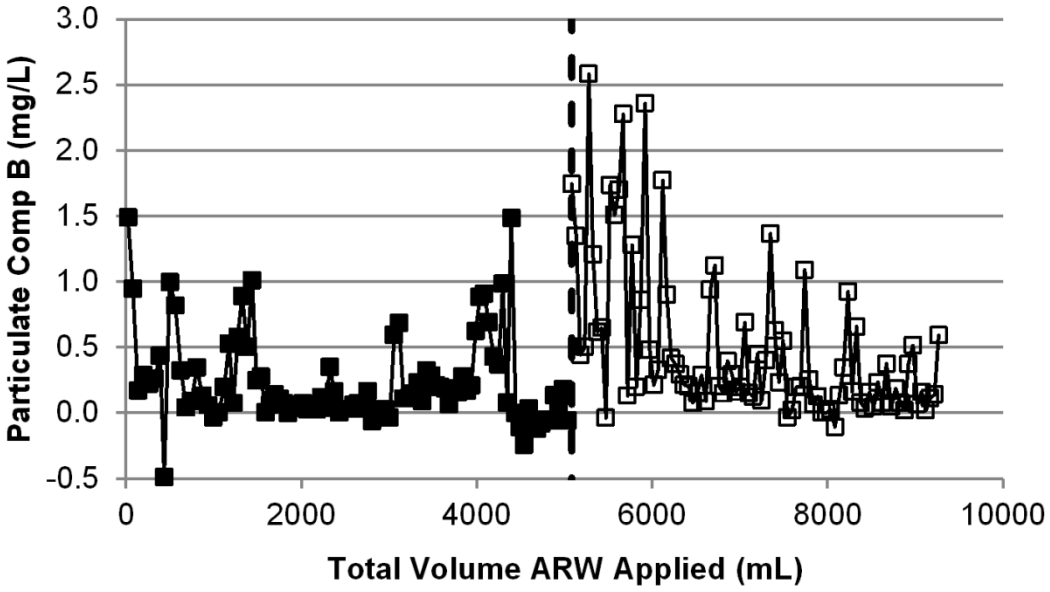

Figure 2.4-3. Particulate Comp B in effluent during drop-wise weathering of EODTECHDIV Comp B residues.

■, drip height 30 cm; □, drip height 100 cm. The dashed line indicates when the height of the dripping increased from 30 cm to 100 cm.

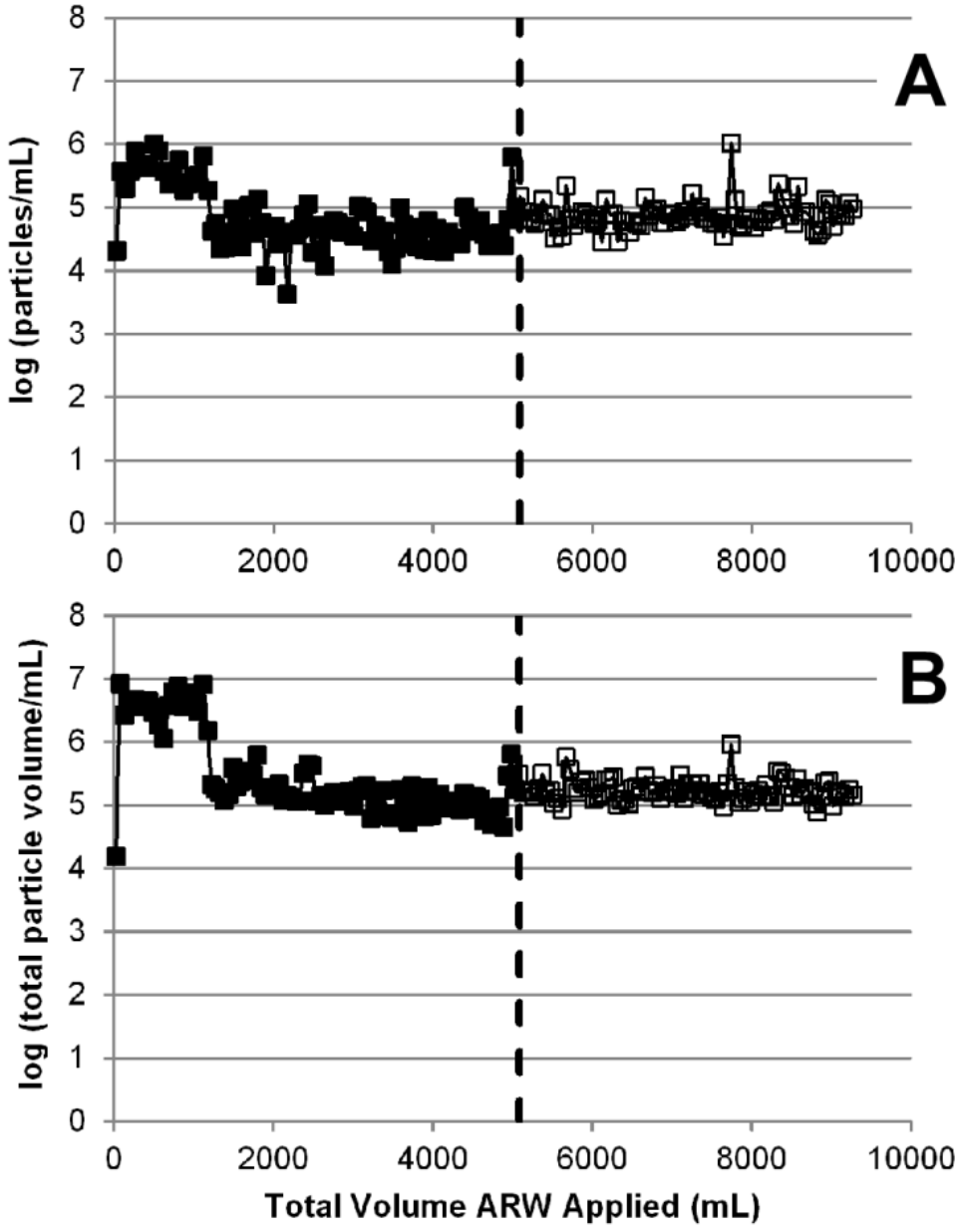

Figure 2.4-4. A) Total particle counts and B) total particle volumes in effluent during drop-wise weathering of Comp B residues.

■, drip height 30 cm; □, drip height 100 cm. The dashed line indicates when the height of the dripping increased from 30 cm to 100 cm.

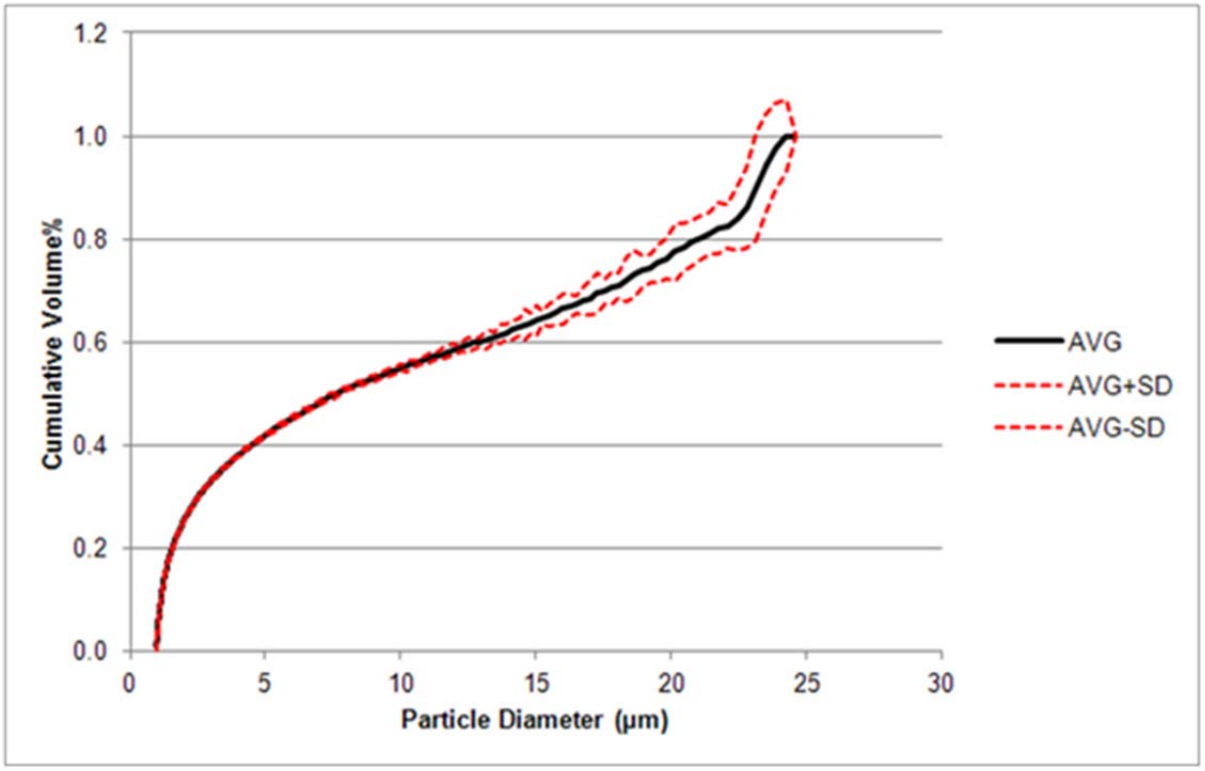

Figure 2.4-5. Cumulative volume percent vs. particle diameter of microscale Comp B particulates produced during drip-wise weathering experiments.
Average from 180 sample analyses shown in black, with standard deviation shown in red.

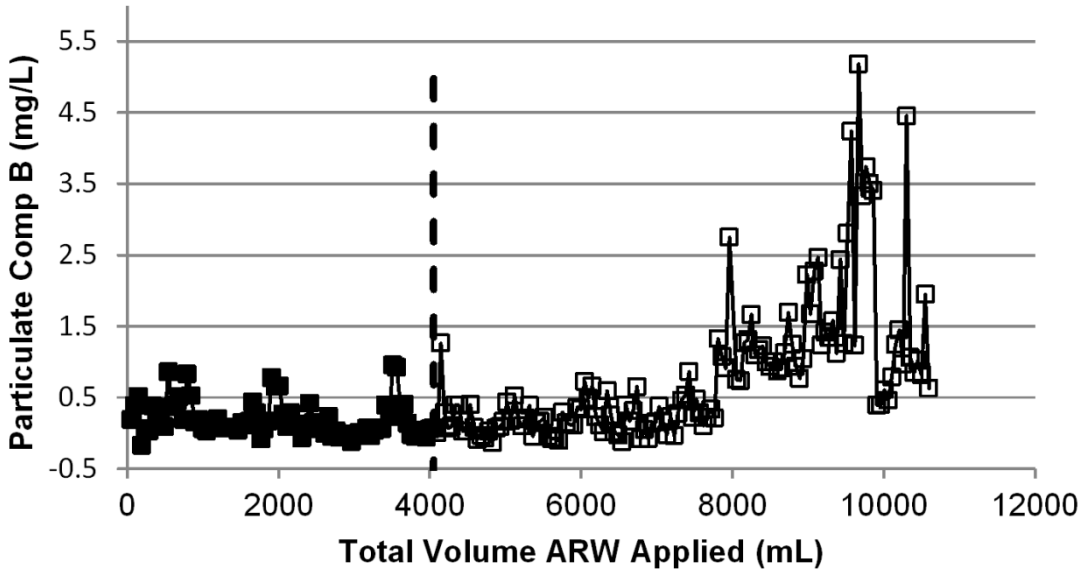

Figure 2.4-6. Particulate Comp B in effluent during drop-wise weathering of China Lake Comp B residues.

■, drip height 30 cm; □, drip height 100 cm. The dashed line indicates when the height of the dripping increased from 30 cm to 100 cm.

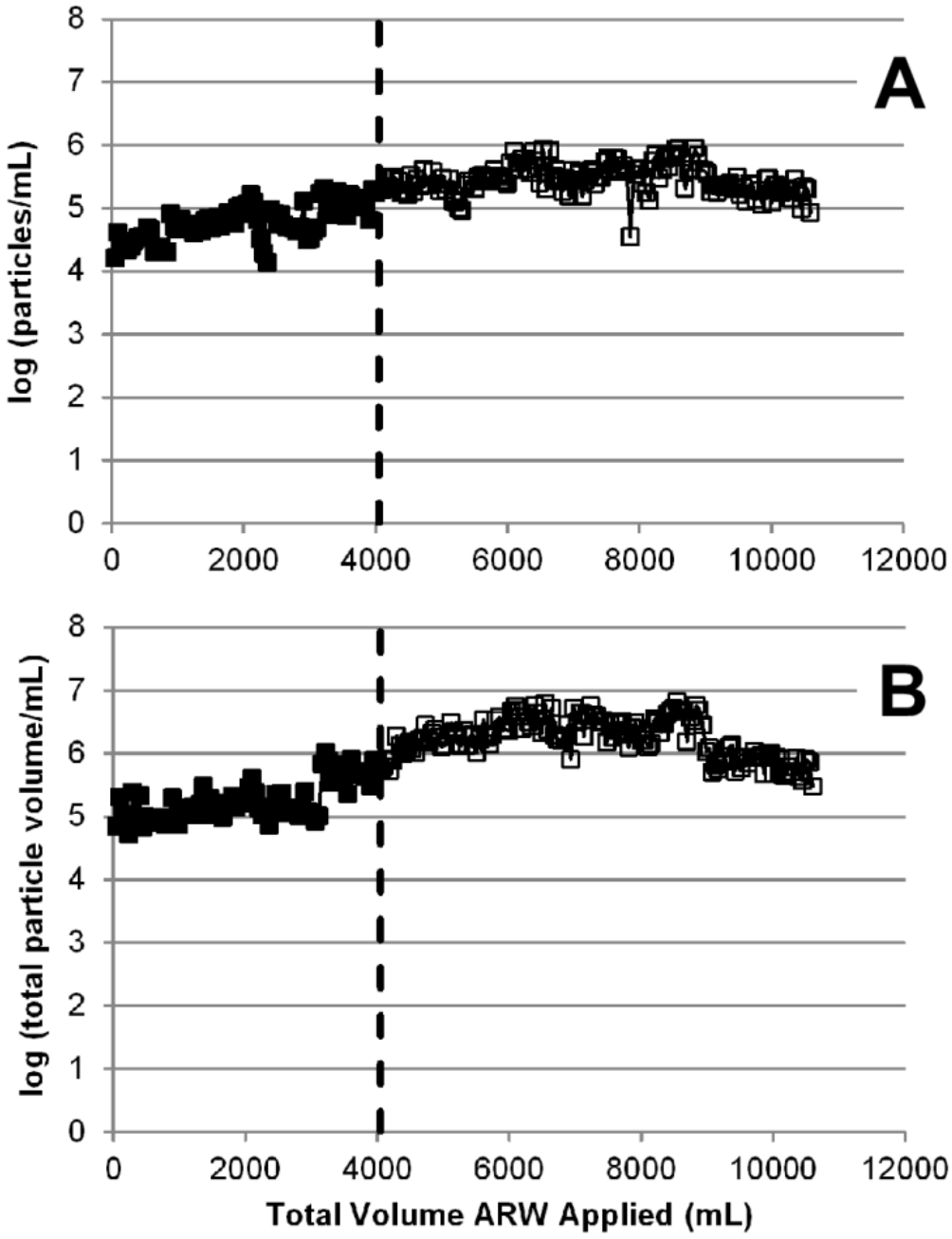

Figure 2.4-7. A) Total particle counts and B) total particle volumes in effluent during drop-wise weathering of China Lake Comp B residues.

■, drip height 30 cm; □, drip height 100 cm. The dashed line indicates when the height of the dripping increased from 30 cm to 100 cm.

Production of microscale particles during weathering under artificial precipitation. An initial screening run to test the spray experiment apparatus indicated that qualitative changes in particle production either by Elzone particle size analysis or by HPLC analysis were observed as the spray intensity changed (e.g., stronger simulated rain resulted in more intense peaks of particle formation compared to light or moderate simulated rain) (Figure 2.4-8). However, the particulate Comp B production rate (in units of mg min^{-1}) was quite variable over time, so statistically discernible differences between nozzles designated by Lechler as delivering different intensities of artificial precipitation could not be calculated (Figure 2.4-9). Therefore, subsequent experiments were performed using only the nozzle which produced strong to very strong precipitation (defined as 1.4 to 5.0 cm h^{-1} m^{-2}, Table S1). Thorough drying of the residues also did not appear to result in changes in particulate production from precipitation (Figure S4). Elzone analysis indicated that the mean particle diameter detected during the spray experiments in the samples was 9.8 μm (n = 160, Figure 2.4-10), which was similar to that observed during the drip experiments. A comparison of the concentration of Comp B particulates as measured by HPLC (as mg/L) and as calculated from the Elzone data (e.g., particle volume/L x Comp B density) indicated that the Elzone underestimated the particulate Comp B concentrations by about 40%. This could have been due to the Elzone's inability to detect larger (e.g., >25 μm) particles when using the 30 μm orifice. However, spot checks of a few samples with the larger 380 μm orifice (8 to 250 μm detection range) only detected a few larger diameter particles, and 90% of the particulates detected were still less than approximately 50 μm (particle volume basis). Even though the Elzone mixes the sample during analysis, it is possible that larger particles were not detected due to settling out. The Elzone also only measures a portion of any given sample, so larger particles present at very low concentrations have a statistically lower probability of being detected. A final possible explanation for the different in calculated particulate Comp B mass is that there was some dissolution of particulates in the samples before (or during) Elzone analysis, resulting in a lower measured total particulate volume. Based on these considerations, only HPLC data would be collected for subsequent spray experiments used for quantitative analyses.

In duplicate spray experiments, precipitation-driven aging resulted in a large initial flush of Comp B particles, followed by lower, but sustained particle generation (Figure 2.4-11). The flush likely reflects an initial "wash-off" of small Comp B particles loosely bound to the larger chunk, while the sustained particle detection at later times represent nascent formation of microscale Comp B due to a combination of dissolution and water drop impact. Small residues, mixed with and/or adhering to larger particles, have also been proposed to be responsible for the initial spike of dissolved explosives observed during leaching experiments (26, 38). Particulate Comp B as a percentage of the total explosive mass recovered during aging averaged about 10% to 20% over the duration of the experiments, although over 60% of eluting explosives were detected as particulate Comp B at early times (Figure 2.4-12). Total Comp B mass lost (both dissolved plus particulates) during the experiments averaged approximately 1% of the initial residue mass, of which 30% was represented by particulates (>0.45 μm). No pattern in particle

formation was observed when the residues were allowed to dry for a few days between applications of ARW, indicating that wet-dry cycles may not be a dominant factor in residue weathering.

Explosive residues on the soil surface present a rather unique type of contamination compared to most pollutants in the environment, in that the solid phase explosive can be dispersed from a single point source (e.g., chunk) as either dissolved or particulate contamination. Perhaps the only similar phenomena are colloid-facilitated transport in soil and aqueous systems of pollutants like metals, hydrophobic compounds, phosphorus, etc. (10, 23, 24), or the disintegration and dispersal of animal fecal pats (5, 11). However, the analogies with these processes breaks down when one considers that explosive compounds can actually exist as microscale particulates, as opposed to just being molecular-scale chemicals sorbed or otherwise associated with non-contaminant soil particles/colloids. Previous research in our laboratory has already demonstrated that microscale Comp B particles (mean particle size 50 μm) emplaced on sand exhibited a greater flux of dissolved explosives than mm-sized residues, and that microscale Comp B particulates actually migrated into the sand matrix (14). The increased flux was due to an increase in the effective contact time between infiltrating ARW and the Comp B because of migration of the microscale particles into the sand matrix (15). The time course of particulate formation observed during the spray experiments indicates that when larger detonation residues are produced in field, the first contact with precipitation would be expected to result in a large flush of particulates, with subsequent exposure producing a lower but sustained level of particles. This scenario would be expected to increase the footprint of the detonation residues as particulates move into and across the soil surface.

In situ weathering of Comp B detonation residues in a salt marsh environment was studied by Walsh et al. (2010) (55), who reported that the timeframe for complete disappearance of the residues (based on visual inspection) was shorter than predicted by a recent model developed by Lever et al. (2005) (25). Applying the results of this current research, one plausible explanation for this enhanced disappearance of residues is that the particulates produced by precipitation-driven (or even tidal flooding) weathering lead to faster disappearance of the larger detonation residues through the enhanced dissolution of microscale particles that was not accounted for in the model. Additionally, there was likely production and dispersal of microscale Comp B particulates generated during weathering by surface runoff. Combined, these findings indicate that the existing models could be improved by incorporating parameters for microscale particle generation and dissolution. Given that production of microscale particulates by precipitation-driven weathering of cm-sized Comp B residues has been documented, areas that warrant further investigation include surface runoff transport into aqueous receptors, as well as ecotoxicology of particulate energetics on soil mesofauna.

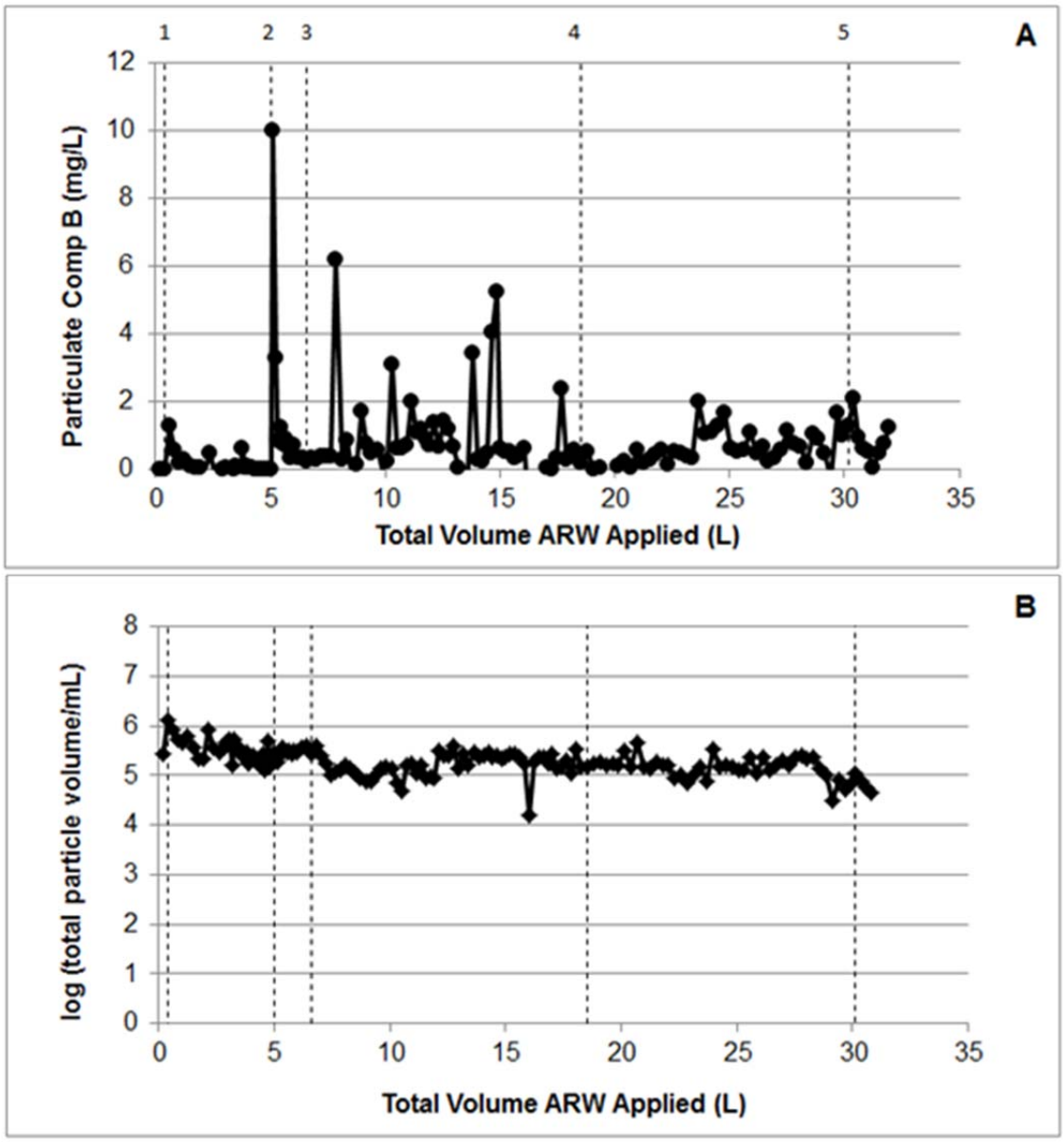

Figure 2.4-8. Detection of particles during an initial spray experiment based on (A) HPLC analysis and (B) Elzone analysis.

Changes in the simulated precipitation intensity and other key events are noted with numbered vertical dashed lines, and were as follows 1) moderate to strong; 2) strong to very strong; 3) dry residues, 3 d @ 40°C, then continue strong to very strong; 4) light to moderate; 5) strong to very strong..

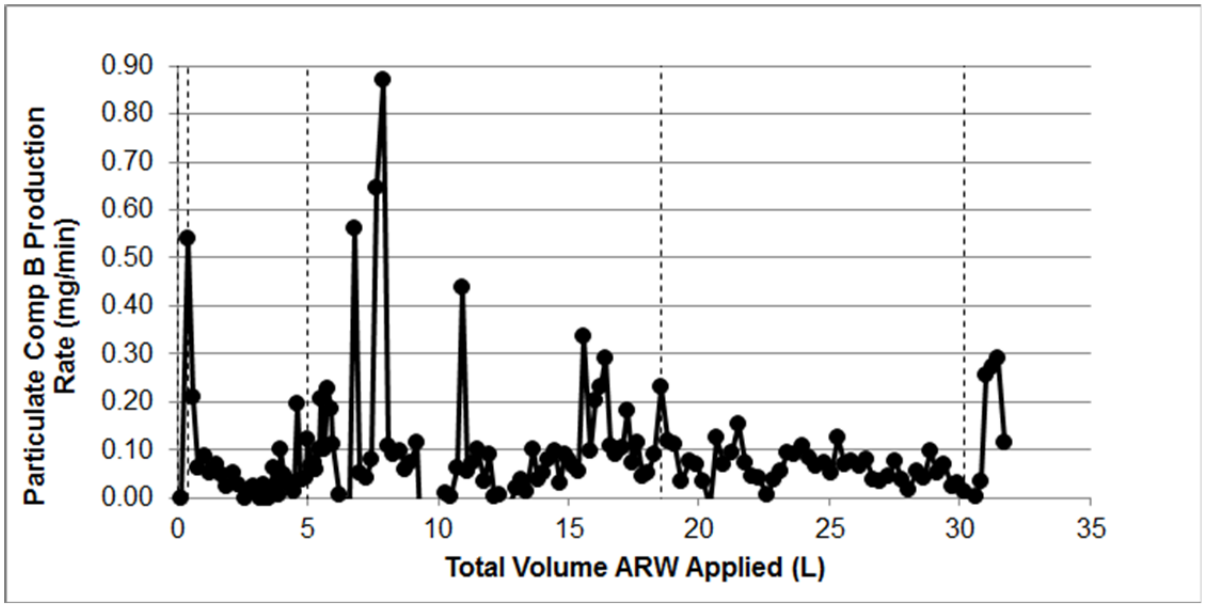

	Plot Interval		Volumetric Flow (measured) L/min		Particulate Comp B (HPLC, Total - Soluble) mg/min	
		n	AVG	SD	AVG	SD
Moderate to Strong	0 - 5	36	0.06	0.02	0.05	0.1
Strong to Very Strong	5 - 19	69	0.17	0.01	0.11	0.16
Light to Moderate	19 - 30	42	0.07	0	0.06	0.04
Strong to Very Strong	30 - 32	5	0.17	0	0.19	0.11

Figure 2.4-9. Particulate Comp B production rate during an initial spray experiment. Changes in the simulated precipitation intensity and other key events are noted with numbered vertical dashed lines, and were as follows 1) moderate to strong; 2) strong to very strong; 3) light to moderate; 4) strong to very strong.

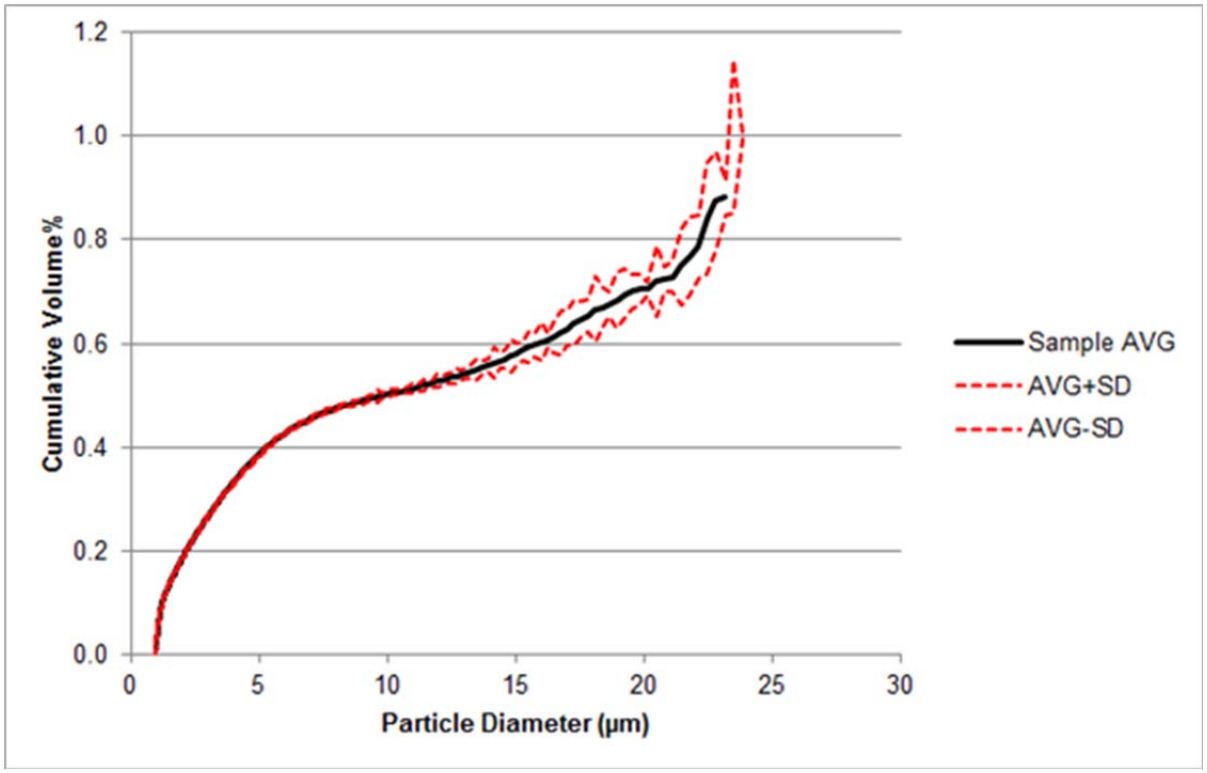

Figure 2.4-10. Cumulative volume percent vs. particle diameter of microscale Comp B particulates formed under artificial precipitation during spray experiments.
Average from 160 sample analyses shown in black, with standard deviation shown in red.

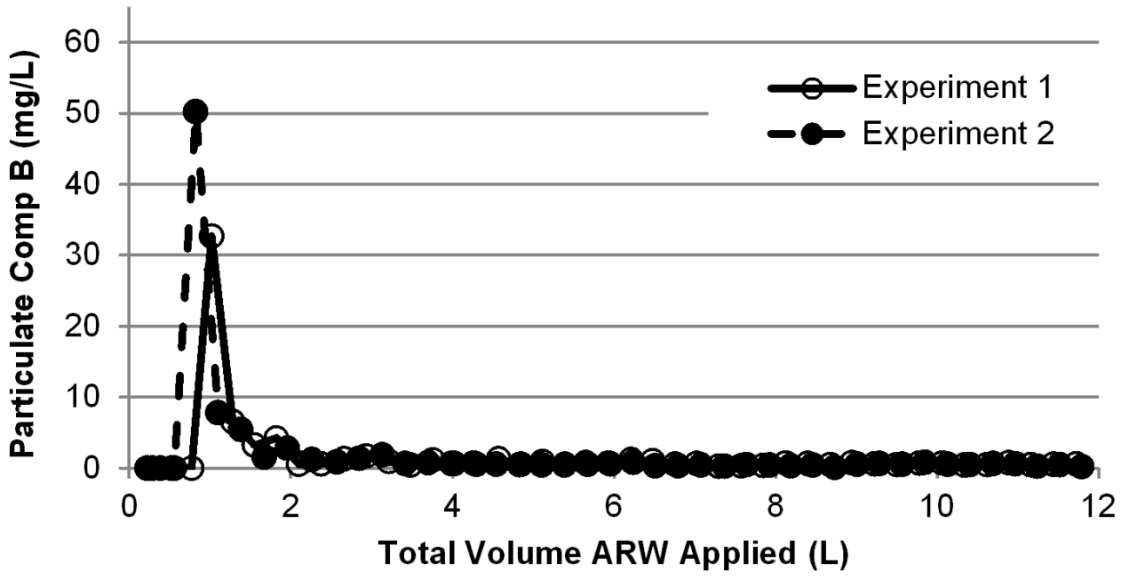

Figure 2.4-11. Particulate Comp B in effluent during duplicate experiments examining weathering of EODTECHDIV Comp B residues under simulated precipitation.

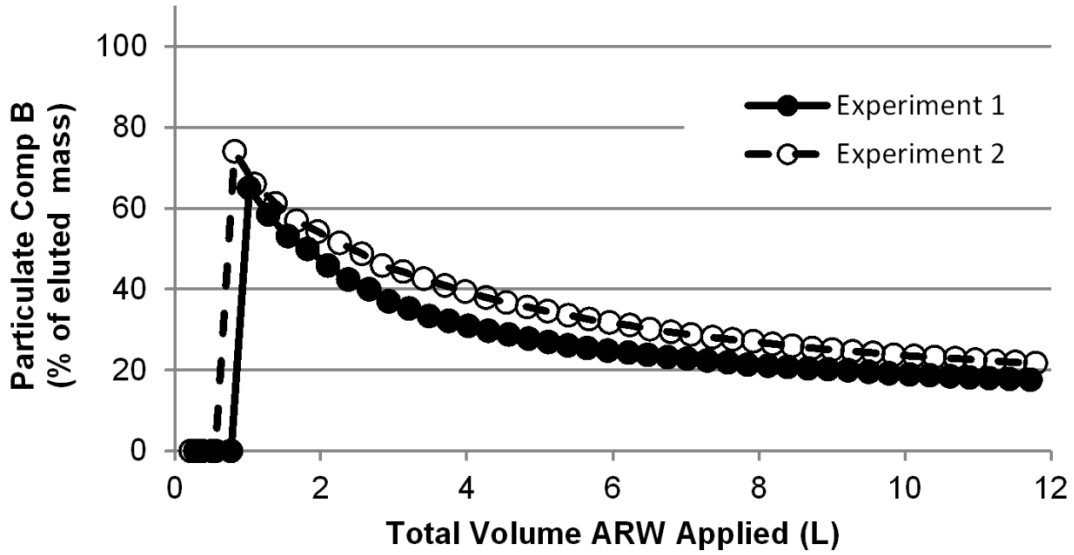

Figure 2.4-12. Percent of total recovered explosive mass recovered as particulate Comp B in effluent during duplicate experiments examining weathering of EODTECHDIV Comp B residues under simulated precipitation.

2.4.4 Conclusions

This research presents the first direct evidence demonstrating the production of microscale explosive particulates under realistic simulated precipitation. Upon application of precipitation to fresh Comp B detonation residues, and initial flush of microscale particulates was observed, followed by a lower, but sustained release of particulate Comp B (defined as >0.45 μm) that represented an average of 30% of the explosive mass released. Production of microscale particulates was generally proportional to precipitation intensity, although there was significant variability over time during Comp B aging. These results provide important insights into one of the initial steps controlling the fate of energetic residues in the environment, namely, the physical breakdown of macroscale residues into smaller particulates that can then further dissolve (15, 56, 57) or be transported into the soil (14). These data provide the basis for more comprehensive fate and transport modeling of these unique class of contaminants.

2.5 Task 5 – Evaluation of Dissolved and Particulate Explosives in Surface Runoff

2.5.1 Goal

The goal of this task was to assess whether microscale particulate explosives could be detected in periodic surface runoff from an active testign range.

2.5.2 Introduction

To our knowledge, there have been no published reports evaluating the extent to which explosives (dissolved or particulate) are detected in surface runoff at either closed or active ranges. However, based on the results from the previous tasks, it was concluded that microscale particulate explosives could be generated from weathering of larger residues, and that these microscale particulates would likely be mobilized during surface runoff. This work was therefore undertaken as a preliminary attempt to address this issue.

2.5.3 Methods

Surface water sampler emplacement. A photograph of the passive surface runoff sampler device (Nalgene™ Storm Water Sampler, Part Number 1100-1000) used is shown in Figure 2.5-1. The outer tube (Nalgene® Mounting Kit, Part Number 1230F21) was emplaced in a shallow hole and secured to a steel L-brace driven into the ground. A removable inner sampling collection device was then placed inside the buried tube. During a rain event, water enters holes in the wall of the outer tube and fill the inner sampling device. As water fills the sample bottle, a float ball in the inlet of the sampling device rises and prevents dilution of the sample once the bottle is filled. The removable inner sampler is then retrieved and sealed with a cap. For this application, the standard HDPE bottle was replaced with a polypropylene bottle to minimize sorption of explosives.

A total of six surface runoff samplers were installed at two locations at an east coast DoD facility. Locations were selected based on the current runoff infrastructure, which consists of a series of ditches and swales.

One sampler was placed in a stream channel leading from a swale to a marsh area. The channel has ongoing seepage just below the surface, and active flow during rain events. The intake level for B1, the depth at which the water in the channel must flow in order to get water into the sample bottle, is approximately 1.5". Photos of the emplaced B1 sampler are shown in Figure 2.5-2.

Five additional samplers were installed near the main detonation area over the course of several months. These were designated as A1 through A5, and all were within the catchment area that

drains into the nearby marshy area. Photos of the samplers after emplacement are presented in Figure 2.5-3.

Samplers A1, A3 and A5 were emplaced in the main drainage swale between a mowed and unvegetated area leading from the edge of the Arena circle. A1 and A3 were on opposite sides of hay bales meant to reduce sediment erosion from entering the marsh. A5 was placed a significant distance upgradient where water was expected to initially enter the ditch system.

Samplers A2 and A4 was emplaced in the ditch that drains a non-vegetated area on the southeast edge of the detonation area, each located on the opposite sides of hay bales meant to reduce sediment erosion.

Site personnel also provided data on the explosives that were detonated, as well as site (or nearby) weather data, so that any correlations between range activities or climatic events and detections of explosives in the surface runoff could be assessed.

Surface water sampling and analysis. A total of 11 sampling events occurred from October 2013 to June 2015. Samplers were deployed before expected significant precipitation events, and collected once filled as soon as practicable. Samplers were retrieved by site personnel and shipped to CB&I's Lawrenceville laboratory for processing, and usually arrived within 2 days of collection.

The initial five runoff samples were only analyzed for explosives, but all samples starting with those collected in July 2014 were analyzed for perchlorate and wet chemistry, as detailed in Table 2.5-1. Samples from location BM-1 were only collected in October 2013 and January 2014.

Sampling processing was as follows:
-Unfiltered, well mixed aliquots were removed for the wet chemistry analyses.

-Approximately two-thirds of the total, well mixed sample from each bottle was passed through a disposable plastic filter funnel holding a glass microfiber filter (Whatman 1823-047, 2.7 µm nominal pore size). Multiple filters were used as needed, and all filters were saved for analysis of collected solids

-Approximately one third of the filtrate was then passed through a glass microfiber syringe filter (Whatman 1618-1304, 25 mm, 0.45 µm pore size).

-The explosives in the unfiltered, 2.7 µm, and 0.45 µm filtrates were spiked with two recovery standards (3-nitrotoluene (3-NT) and 2,4-dinitroanisole (DNAN)) then passed through a pre-

conditioned Supelclean™ ENVI-Chrom P solid phase extraction (SPE) column (250 mg packing; Sigma-Aldrich, St. Louis, MO, USA). The analytes on the SPE column were eluted with acetonitrile, then the extract was evaporated to a volume of 1 ml, diluted 1:1 with deionized distilled water, and analyzed via HPLC.

-The solids collected on the 2.7 µm filters were dried at approximately 40°C. The filters were weighed, then extracted with acetonitrile in a water cooled sonicator for at least 48 hours. Extracts were removed and evaporated to 1 to 2 ml final volume, then analyzed via HPLC.

2.5.4 Results and Discussion

Precipitation data covering the period during which surface water sampling was performed are is shown in Figure 2.5-4, and followed the typical seasonal cycle.

Amounts of key energetics (e.g., HMX, RDX, perchlorate) detonated at the site based on information provided by site personnel, along with an indication of when energetic compounds were detected in the collected surface runoff, are presented in Figure 2.5-5.

The volumes of liquid and mass of collected solids extracted for analysis of explosives in each of the surface runoff samples is shown in Table 2.5-2. Surface runoff sample data are presented in Table 2.5-3 (HMX), Table 2.5-4 (RDX), and Table 2.5-5 (wet chemistry). A summary of energetics detected in the surface runoff over the duration of field sampling is shown in Table 2.5-6.

The surface runoff had an average pH of 5.9 ± 0.4 S.U. (n =29), and contained variable concentrations of organic carbon (18 ± 10 mg/L), nitrate (1.3 ± 2.0 mg/L), and sulfate (8.4 ± 6.9 mg/L). Most samples contained a reasonable amount of total solids and total volatile solids, and there was a slight trend that samples collected upgradient from the hay bales contained more solids than samples collected downgradient from the hay bales. The presence of soil particulates in the samples supports the assumption that explosive particulates, if present, would also have been captured during sampling.

For the five sample locations positioned near the main detonation area (A1-A5), perchlorate was detected in 24 out of 29 (83%) surface runoff samples, and ranged from a low of 0.2 µg/L to a high of 673 µg/L. HMX was detected in 15 out of 41 (37%) whole surface runoff samples, and ranged from a low of 0.4 µg/L to a high of 11.1 µg/L. RDX was detected in 20 out of 41 (50%)surface runoff samples, and ranged from a low of 0.1 µg/L to a high of 11.2 µg/L.

The ratio of explosives concentrations in unfiltered surface water with samples passed through a 0.45 µm filter did seem to indicate the presence of microscale particulates (or, at least, explosives

associated with solids) in some samples, e.g., the total explosive concentration of unfiltered samples was higher than in 0.45 μm filtered samples. Most of the ratios of unfiltered vs. filtered concentrations were only slightly greater than 1, indicating that on the order of 10 to 30% of the total explosives were particulate or particle associated. The few ratios that were less than 1 could be result of incomplete capture and extraction of the explosives during solid phase extraction. Ratios calculated for RDX and HMX were moderately correlated (r^2 = 0.55; excluding one extreme outlier from June 2015 sample set), adding additional support for the presence of particulate or particle-associated explosives. Analysis of total suspended solids in the surface water samples was too limited to allow any relationship between detection suspended solids and particulate explosives to be assessed.

The RDX breakdown product MNX was detected in a few samples from May 2014. Some RDX in the unfiltered sample may have partially degraded to MNX prior to SPE concentration, given that it was not preserved in any manner and there was organic matter (plant and soil detritus) present in the sample. Alternatively, the MNX may have been present in the sample from the time of collection as product of in situ biological or abiotic processes. In addition, the RDX breakdown product TNX was observed in some of the July 2014 samples. The presence of TNX may indicate additional degradative processes were occurring either on the soil surface or in the surface runoff. TNX is usually associated with anaerobic biological nitro-reduction, although abiotic processes can also produce TNX (e.g., reduction by reduced Fe species).

Based on these data, no temporal coincidence was observed between the timing of the detonation of a given energetic and the detection of that energetics in surface runoff. There also did not appear to be any direct relationship between the mass of energetic detonated and the concentration of energetics in the surface runoff. It is likely that the processes driving the appearance of energetics in the surface runoff is complex, including the random distribution of energetic residues created by a detonation, occurrence of high vs. low order detonations, the variation in runoff flow paths as a function of precipitation amounts and vegetation, etc.

RDX was detected in only 4 out of 41 (10%) of the surface runoff solids samples collected and extracted (Table 2.5-4). The lower detection of particulate (or particulate associated) explosives may reflect the inability of the passive surface runoff sampling process, e.g., the water is collected and sits in the sample bottle for hours to day before solids are collected, allowing any microscale particles to completely dissolve. A more active sampling procedure, in which surface runoff is collected and immediately filtered to collect particulate explosives, would be recommended.

2.5.4 Conclusions

The overall conclusion of this sampling effort was that energetic compounds, including HMX, RDX, and perchlorate, were present in surface runoff around an active detonation area at this site. A direct correlation or relationship between the types and amounts of energetics detonated could not be detected based on the limited data, but may be possible with a more intensive sampling at a number of types of active sites (e.g., firing ranges vs. testing ranges; mortar vs. rocket vs. grenade training areas, etc.).

Based on this limited field sampling effort, surface runoff is likely a small, but measurable and persistent, route of transport for energetic contaminants within and possibly offsite of DoD testing and training ranges.

Removable inner bottle

Outer tube (installed into ground)

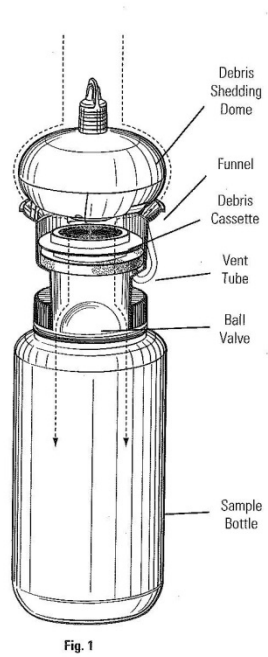

Fig. 1

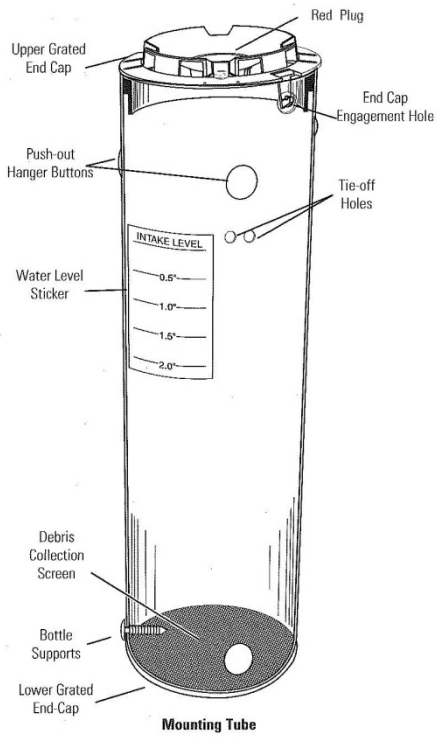

Mounting Tube

Figure 2.5-1. Photographs of the surface water samplers.


Inlet holes ~1.5" above ground surface

Figure 2.5-2. Photographs of the surface water sampler at location B1.

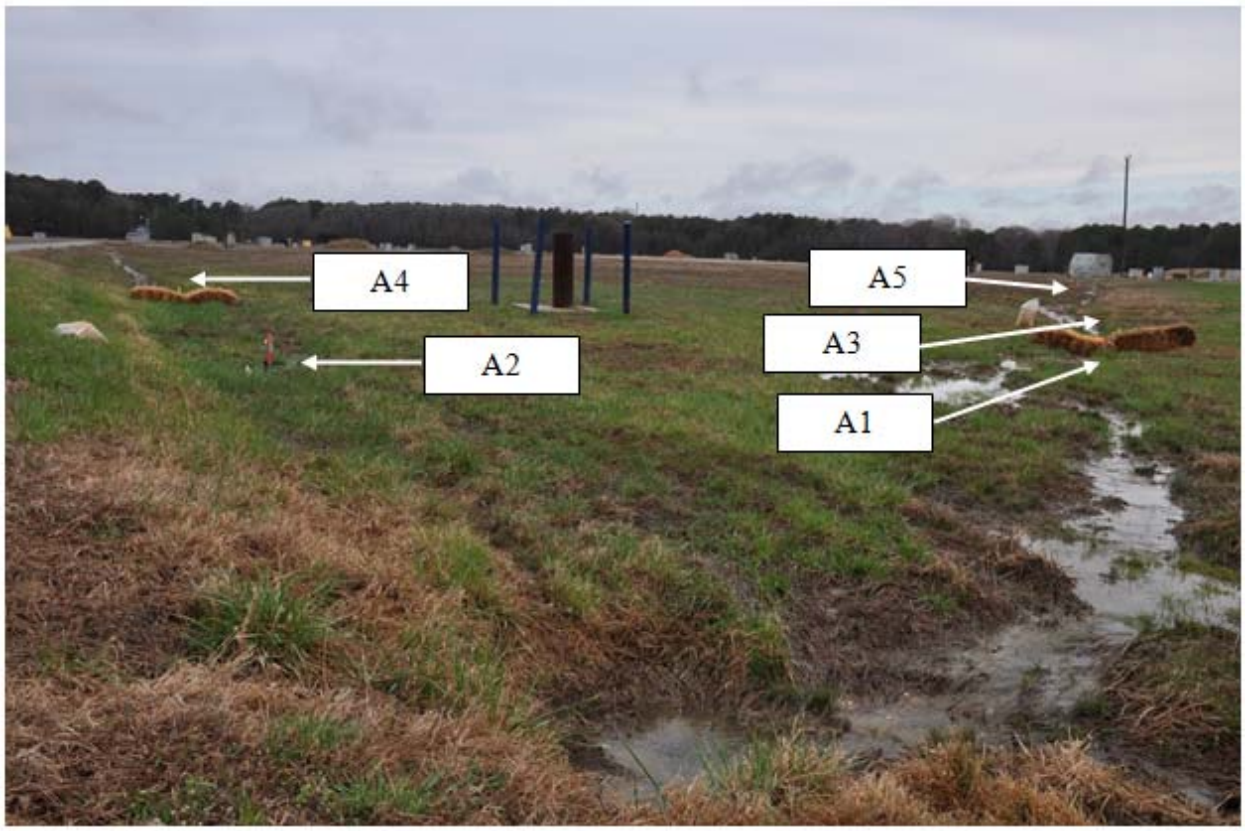

Figure 2.5-3. Photographs of the main detonation area surface water samplers.

A3 relative to Arena-1. General runoff flow is designated by white arrows. 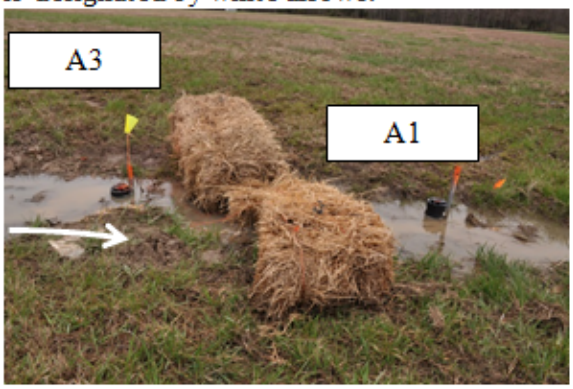 	A3 close-up. Finger is at inlet depth, flush with bottom of runoff channel 
A4 relative to A2. General runoff flow is designated by white arrows. 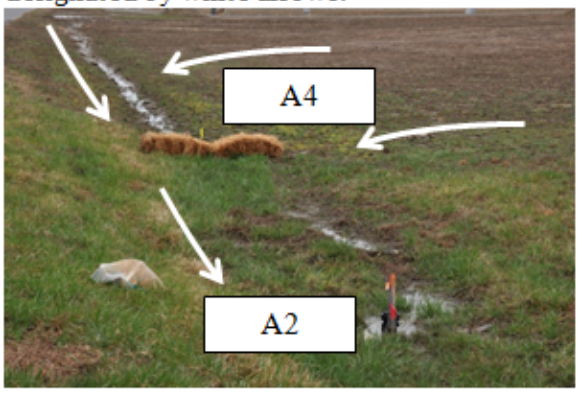 	A4 close-up. Finger is at inlet depth, flush with bottom of runoff channel 
A5. General runoff flow is designated by white arrows.  	A5 close-up. Finger is at inlet depth, flush with bottom of runoff channel 

Figure 2.5-3. (cont.).

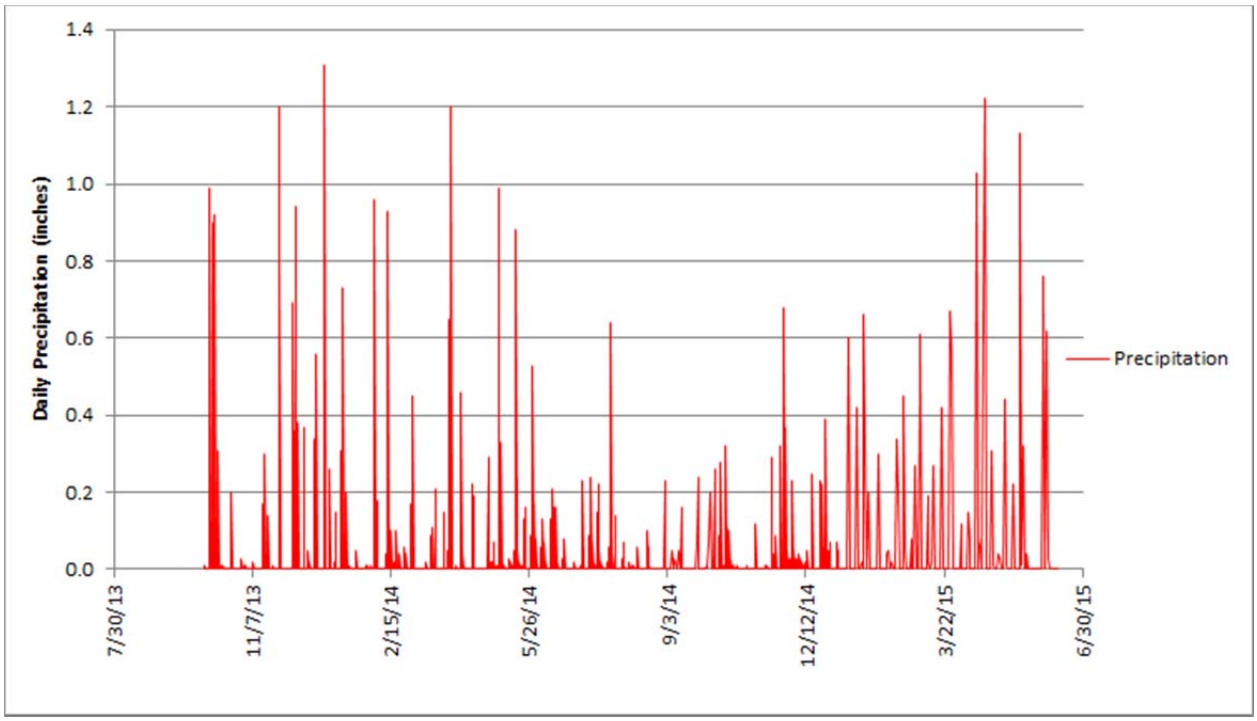

Figure 2.5-4. Plot of precipitation recorded at the site during the period of surface runoff sampling.

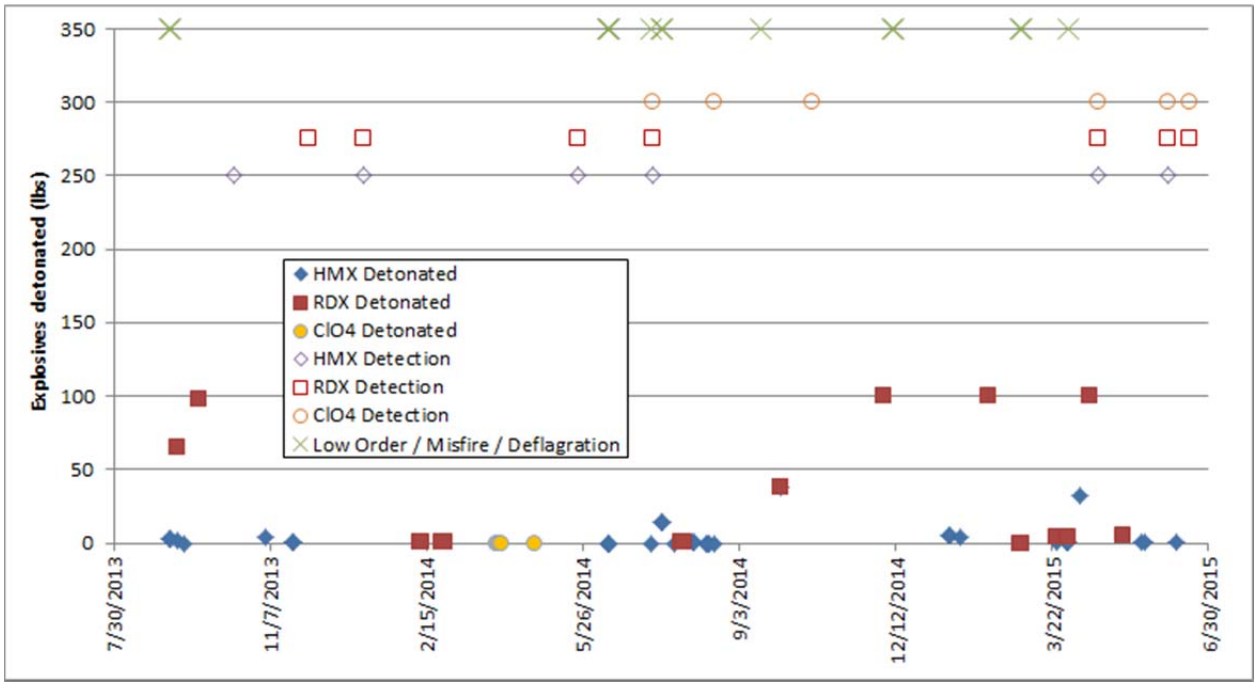

Figure 2.5-5. Mass of energetics detonated and indication of incomplete detonations, misfires, and deflagrations.

NOTE: Energetic detections are assigned arbitrary values of 250, 275, and 300 for HMX, RDX, and perchlorate, respectively, to allow plotting on same scale as mass detonated. See text and other figures and tables for actual energetic concentration data.

× = no detection above the detection limit

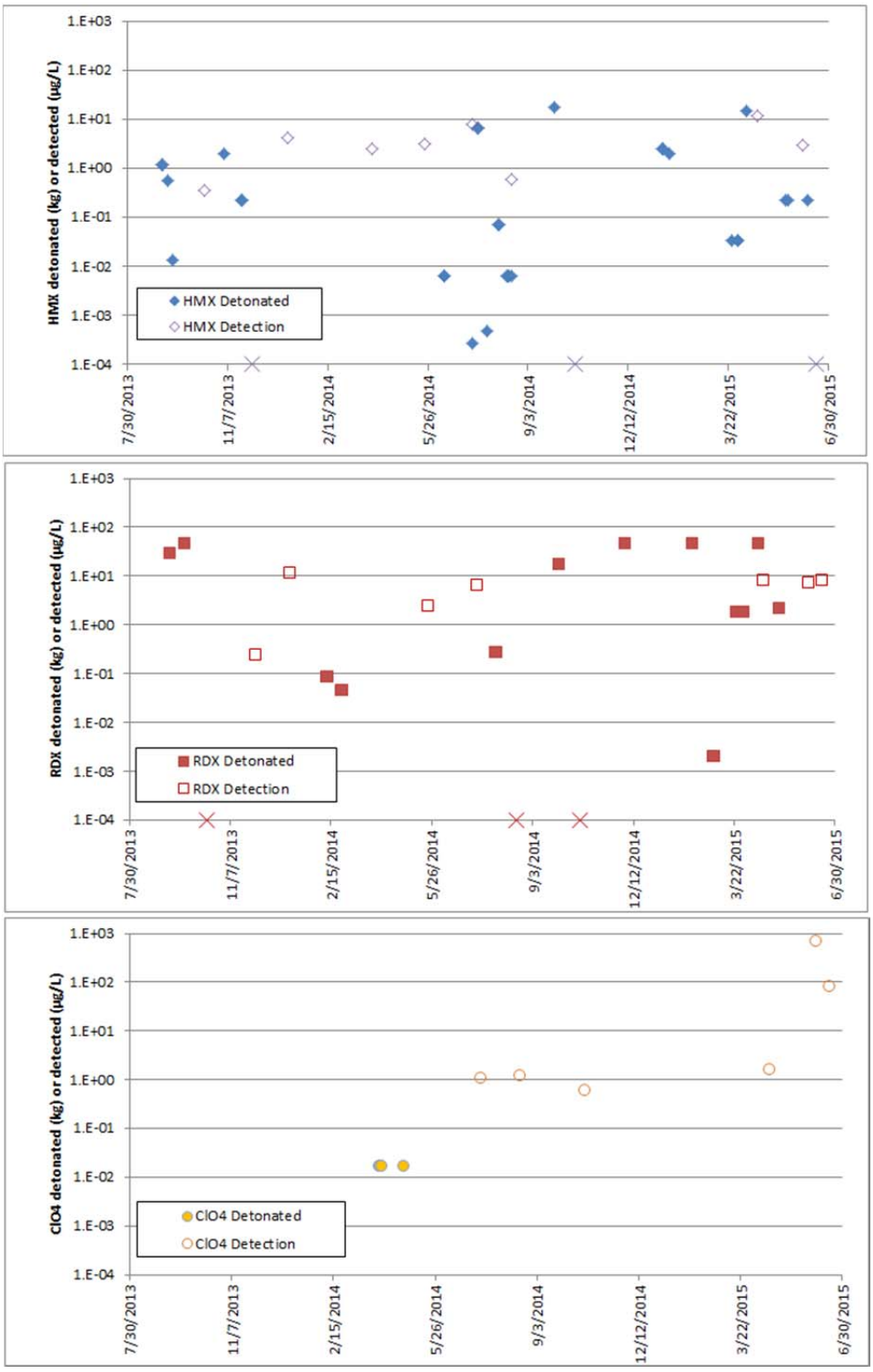

Figure 2.5-6. Masses of HMX, RDX, and perchlorate detonated at the site and maximum concentrations of energetic compounds detected in surface runoff.

Analyte	Method
pH	EPA Method 150.1
Conductivity	EPA Method 120.1
Total organic carbon (TOC)	EPA Method 415.1
Total volatile solids (TVS)	EPA Method 160.4
Total solids (TS)	EPA Method 160.3
Perchlorate	EPA Method 314.0
Anions	EPA Method 300.0
Explosives	modified EPA Method 8330

Table 2.5-1. Analytical suite for surface runoff samples.

Sample Loc:	Inlet height Inches above soil surface	October 2013 (10/15/13)				December 2013 (12/02/13)				January 2014 (01/06/14)			
		Aqueous (L concentrated)			Solids (g extracted)	Aqueous (L concentrated)			Solids (g extracted)	Aqueous (L concentrated)			Solids (g extracted)
		Unfiltered	< 2.7 µm	< 0.45 µm	> 2.7 µm	Unfiltered	< 2.7 µm	< 0.45 µm	> 2.7 µm	Unfiltered	< 2.7 µm	< 0.45 µm	> 2.7 µm
B1	1.5	ND	1.15	ND	0.48	--	--	--	--	0.39	0.34	0.35	0.69
A1	1	ND	1.1	ND	trace	--	--	--	--	0.33	0.35	0.42	0.35
A2	2	ND	1.18	ND	0.08	0.50	0.43	0.35	0.18	0.35	0.32	0.32	0.09
A3	0	--	--	--	--	--	--	--	--	--	--	--	--
A4	0	--	--	--	--	--	--	--	--	--	--	--	--
A5	0	--	--	--	--	--	--	--	--	--	--	--	--

Sample Location	Inlet height Inches above soil surface	March 2014 (03/31/14)				May 2014 (05/23/14)				July 2014 (07/10/14)			
		Aqueous (L concentrated)			Solids (g extracted)	Aqueous (L concentrated)			Solids (g extracted)	Aqueous (L concentrated)			Solids (g extracted)
		Unfiltered	< 2.7 µm	< 0.45 µm	> 2.7 µm	Unfiltered	< 2.7 µm	< 0.45 µm	> 2.7 µm	Unfiltered	< 2.7 µm	< 0.45 µm	> 2.7 µm
B1	1.5	--	--	--	--	--	--	--	--	--	--	--	--
A1	1				0.18	0.35	0.36	0.32	0.13	0.38	0.36	0.34	0.06
A2	2				0.16	0.40	0.39	0.32	0.29	0.37	0.35	0.39	0.09
A3	0	--	--	--	--	0.37	0.36	0.34	0.11	0.34	0.36	0.34	0.07
A4	0	--	--	--	--	0.35	0.37	0.33	1.09	0.33	0.36	0.39	0.16
A5	0	--	--	--	--	0.42	0.37	0.38	0.19	0.37	0.37	0.33	0.12

Sample Location	Inlet height Inches above soil surface	August 2014 (08/18/14)				October 2014 (10/20/14)				April 2015 (4/20/2015)			
		Aqueous (L concentrated)			Solids (g extracted)	Aqueous (L concentrated)			Solids (g extracted)	Aqueous (L concentrated)			Solids (g extracted)
		Unfiltered	< 2.7 µm	< 0.45 µm	> 2.7 µm	Unfiltered	< 2.7 µm	< 0.45 µm	> 2.7 µm	Unfiltered	< 2.7 µm	< 0.45 µm	> 2.7 µm
B1	1.5	--	--	--	--	--	--	--	--	--	--	--	--
A1	1	--	--	--	--	0.34	0.33	0.34	0.02	0.33	0.37	0.25	0.03
A2	2	0.30	0.34	0.36	0.01	0.33	0.35	0.35	0.01	0.30	0.37	0.37	0.18
A3	0	0.30	0.34	0.37	0.03	0.29	0.35	0.33	0.02	0.31	0.36	0.32	0.03
A4	0	0.29	0.35	0.34	0	0.33	0.36	0.34	0.01	0.32	0.37	0.30	0.03
A5	0	0.28	0.35	0.36	0.02	0.33	0.37	0.34	0.04	0.28	0.36	0.34	0.04

Sample Location	Inlet height Inches above soil surface	June 2015 (06/04/15 and 06/11/15)				June 2015 (06/18/15)			
		Aqueous (L concentrated)			Solids (g extracted)	Aqueous (L concentrated)			Solids (g extracted)
		Unfiltered	< 2.7 µm	< 0.45 µm	> 2.7 µm	Unfiltered	< 2.7 µm	< 0.45 µm	> 2.7 µm
B1	1.5	--	--	--	--	--	--	--	--
A1	1	0.24	0.35	0.34	0.08	0.28	0.34	0.45	0.06
A2	2	0.28	0.34	0.39	0.02	0.30	0.36	0.35	0.15
A3	0	0.30	0.35	0.38	0.01	0.25	0.35	0.38	0.01
A4	0	0.33	0.37	0.23	0	0.23	0.35	0.35	0.01
A5	0	0.25	0.37	0.30	0	0.32	0.35	0.33	0.04

Table 2.5-2. Volumes of liquid and mass of solids extracted for explosives analyses of surface runoff samples.

HMX		October 2013 (10/15/13)				December 2013 (12/02/13)				January 2014 (01/06/14)			
Sample Location	Inlet height Inches above soil surface	Aqueous (µg/L) Unfiltered	< 2.7 µm	< 0.45 µm	Solids (mg/kg) > 2.7 µm	Aqueous (µg/L) Unfiltered	< 2.7 µm	< 0.45 µm	Solids (mg/kg) > 2.7 µm	Aqueous (µg/L) Unfiltered	< 2.7 µm	< 0.45 µm	Solids (mg/kg) > 2.7 µm
B1	1.5	ND	BD	ND	BD	--	--	--	--	8.72	9.27	7.35	BD*
A1	1.0	ND	0.31	ND	BD	--	--	--	--	1.75	3.40	3.03	BD*
A2	2.0	ND	0.35	ND	BD	BD	BD	BD	BD*	4.30	1.13	1.28	BD*
A3	0.0	--	--	--	--	--	--	--	--	--	--	--	--
A4	0.0	--	--	--	--	--	--	--	--	--	--	--	--
A5	0.0	--	--	--	--	--	--	--	--	--	--	--	--
						*BD, <0.002 mg/kg				*BD, <0.001 mg/kg			
		March 2014 (03/31/14)				May 2014 (05/23/14)				July 2014 (07/10/14)			
Sample Lo	Inlet height Inches above soil surface	Aqueous (µg/L) Unfiltered	< 2.7 µm	< 0.45 µm	Solids (mg/kg) > 2.7 µm	Aqueous (µg/L) Unfiltered	< 2.7 µm	< 0.45 µm	Solids (mg/kg) > 2.7 µm	Aqueous (µg/L) Unfiltered	< 2.7 µm	< 0.45 µm	Solids (mg/kg) > 2.7 µm
B1	1.5	--	--	--	--	--	--	--	--	--	--	--	--
A1	1.0	0.42	BD	0.31	BD*	BD	BD	0.42	BD*	BD	BD	BD	BD*
A2	2.0	BD	1.51	2.48	BD*	2.41	2.67	2.65	BD*	7.90	5.79	4.78	BD*
A3	0.0	--	--	--	--	BD	BD	BD	BD*	BD	BD	BD	BD*
A4	0.0	--	--	--	--	3.24	1.75	1.50	BD*	8.07	6.75	7.69	BD*
A5	0.0	--	--	--	--	2.09	2.27	1.58	BD*	1.49	1.19	1.19	BD*
		*BD, <0.001 mg/kg											
		August (08/18/2014)				October 2014 (10/20/2014)				April 2015 (4/20/2015)			
Sample Lo	Inlet height Inches above soil surface	Aqueous (µg/L) Unfiltered	< 2.7 µm	< 0.45 µm	Solids (mg/kg) > 2.7 µm	Aqueous (µg/L) Unfiltered	< 2.7 µm	< 0.45 µm	Solids (mg/kg) > 2.7 µm	Aqueous (µg/L) Unfiltered	< 2.7 µm	< 0.45 µm	Solids (mg/kg) > 2.7 µm
B1	1.5	--	--	--	--	--	--	--	--	--	--	--	--
A1	1.0	--	--	--	--	BD	BD	BD	BD	BD	BD	BD	BD
A2	2.0	0.60	0.60	BD	BD	BD	BD	BD	BD	2.69	3.79	3.38	BD
A3	0.0	BD	BD	BD	BD	BD	BD	BD	BD	BD	BD	BD	BD
A4	0.0	BD	BD	BD	BD	BD	BD	BD	BD	3.19	2.91	2.39	BD
A5	0.0	BD	BD	BD	BD	BD	BD	BD	BD	11.13	12.07	11.91	BD
		June 2015 (06/04/15 and 06/11/15)				June 2015 (06/18/15)							
Sample Lo	Inlet height Inches above soil surface	Aqueous (µg/L) Unfiltered	< 2.7 µm	< 0.45 µm	Solids (mg/kg) > 2.7 µm	Aqueous (µg/L) Unfiltered	< 2.7 µm	< 0.45 µm	Solids (mg/kg) > 2.7 µm				
B1	1.5	--	--	--	--	--	--	--	--				
A1	1.0	BD	0.25	0.28	BD	BD	0.82	0.61	BD				
A2	2.0	0.89	0.39	0.28	BD	BD	BD	BD	BD				
A3	0.0	3.02	7.12	3.79	BD	BD	BD	BD	BD				
A4	0.0	BD	BD	BD	BD	BD	BD	BD	BD				
A5	0.0	BD	1.77	2.90	BD	BD	1.58	1.15	BD				

--, no sampler in place or no sample collected/analyzed
BD, below detection limits of 0.01 µg/L (accounting for SPE) or 0.01 mg/kg, unless otherwise noted
ND, not done

Table 2.5-3. Summary of HMX detections in surface runoff samples.

RDX		October 2013 (10/15/13)				December 2013 (12/02/13)				January 2014 (01/06/14)			
	Inlet height Inches above	Aqueous (µg/L)			Solids (mg/kg)	Aqueous (µg/L)			Solids (mg/kg)	Aqueous (µg/L)			Solids (mg/kg)
Sample Location	soil surface	Unfiltered	< 2.7 µm	< 0.45 µm	> 2.7 µm	Unfiltered	< 2.7 µm	< 0.45 µm	> 2.7 µm	Unfiltered	< 2.7 µm	< 0.45 µm	> 2.7 µm
B1	1.5	--	BD	--	BD	--	--	--		13.74	14.75	12.14	BD*
A1	1.0	ND	BD	ND	BD	--	--	--		3.81	8.72	7.98	BD*
A2	2.0	ND	BD	ND	BD	0.12	0.21	0.24	BD*	11.20	2.61	2.79	BD*
A3	0.0	--	--	--	--	--	--	--		--	--	--	--
A4	0.0	--	--	--	--	--	--	--		--	--	--	--
A5	0.0	--	--	--	--	--	--	--		--	--	--	--
						RDX spectra not exact match to standard				*BD, <0.001 mg/kg			
						*BD, <0.002 mg/kg							

		March 2014 (03/31/14)				May 2014 (05/23/14)				July 2014 (07/10/14)			
	Inlet height Inches above	Aqueous (µg/L)			Solids (mg/kg)	Aqueous (µg/L)			Solids (mg/kg)	Aqueous (µg/L)			Solids (mg/kg)
Sample Location	soil surface	Unfiltered	< 2.7 µm	< 0.45 µm	> 2.7 µm	Unfiltered	< 2.7 µm	< 0.45 µm	> 2.7 µm	Unfiltered	< 2.7 µm	< 0.45 µm	> 2.7 µm
B1	1.5	--	--	--	--	--	--	--	--	--	--	--	--
A1	1.0	N/A	N/A	N/A	BD*	BD	BD	BD	BD*	BD	BD	BD	BD*
A2	2.0	N/A	N/A	N/A	BD*	1.52	1.68	1.55	BD*	4.59	3.47	3.15	BD*
A3	0.0	--	--	--	--	BD	BD	BD	BD*	BD	BD	BD	BD*
A4	0.0	--	--	--	--	2.37	0.39	0.35	BD*	4.81	4.91	6.48	BD*
A5	0.0	--	--	--	--	0.68	1.51	1.12	BD*	BD	BD	BD	BD*
						MNX	17.53			TNX	0.20		
		*BD, <0.001 mg/kg								TNX	1.28		
		N/A, cross contamination detected								TNX	0.97		

		August (08/18/2014)				October 2014 (10/20/2014)				April 2015 (4/20/2015)			
	Inlet height Inches above	Aqueous (µg/L)			Solids (mg/kg)	Aqueous (µg/L)			Solids (mg/kg)	Aqueous (µg/L)			Solids (mg/kg)
Sample Location	soil surface	Unfiltered	< 2.7 µm	< 0.45 µm	> 2.7 µm	Unfiltered	< 2.7 µm	< 0.45 µm	> 2.7 µm	Unfiltered	< 2.7 µm	< 0.45 µm	> 2.7 µm
B1	1.5	--	--	--	--	--	--	--	--	--	--	--	--
A1	1.0	--	--	--	--	BD	BD	BD	BD	BD	BD	BD	1.20
A2	2.0	BD	BD	BD	BD	BD	BD	BD	BD	1.34	1.77	1.82	0.22
A3	0.0	BD	BD	BD	BD	BD	BD	BD	BD	0.36	0.48	0.55	1.02
A4	0.0	BD	BD	BD	BD	BD	BD	BD	BD	2.12	2.06	2.31	0.90
A5	0.0	BD	BD	BD	BD	BD	BD	BD	BD	7.13	8.08	8.06	BD
		*BD, <0.001 mg/kg											

		June 2015 (06/04/15 and 06/11/15)				June 2015 (06/18/15)			
	Inlet height Inches above	Aqueous (µg/L)			Solids (mg/kg)	Aqueous (µg/L)			Solids (mg/kg)
Sample Location	soil surface	Unfiltered	< 2.7 µm	< 0.45 µm	> 2.7 µm	Unfiltered	< 2.7 µm	< 0.45 µm	> 2.7 µm
B1	1.5	--	--	--	--	--	--	--	--
A1	1.0	1.40	0.47	0.62	BD	1.37	1.03	1.68	BD
A2	2.0	0.38	1.61	0.97	BD	BD	BD	BD	BD
A3	0.0	7.33	6.75	10.29	BD	0.74	0.74	1.01	BD
A4	0.0	BD	BD	BD	BD	0.74	BD	BD	BD
A5	0.0	3.20	1.85	3.37	BD	7.90	2.94	1.92	BD
		*BD, <0.001 mg/kg							

--, no sampler in place or no sample collected/analyzed
BD, below detection limits of 0.01 µg/L (accounting for SPE) or 0.01 mg/kg, unless otherwise noted
ND, not done

Table 2.5-4. Summary of RDX (and RDX metabolite) detections in surface runoff samples.

pH unfiltered S.U.			AVG SD n	5.9 0.4 29		MIN MAX	5.0 6.7						
Sample Location	Inlet height Inches above soil surface	S.U. 10/15/13	12/02/13	01/06/14	03/31/14	05/23/14	07/10/14	08/18/14	10/20/14	04/20/15	06/04/15	06/11/15	06/18/15
B1	1.5	-	-	-	-	-	-	-	-	-	-	-	-
A1	1.0	-	-	-	-	-	6.1	-	5.4	6.7	-	5.0	5.3
A2	2.0	-	-	-	-	-	6.1	5.9	5.9	6.3	-	5.5	5.3
A3	0.0	-	-	-	-	-	6.0	5.6	6.0	6.6	-	5.9	5.4
A4	0.0	-	-	-	-	-	6.3	5.7	6.0	6.4	6.0	-	5.3
A5	0.0	-	-	-	-	-	6.2	5.8	6.0	6.6	6.1	-	5.5
Conductivity unfiltered umhos/cm			**AVG SD n**	**90 46 29**		**MIN MAX**	**42 227**						
Sample Location	Inlet height Inches above soil surface	umhos/cm 10/15/13	12/02/13	01/06/14	03/31/14	05/23/14	07/10/14	08/18/14	10/20/14	04/20/15	06/04/15	06/11/15	06/18/15
B1	1.5	-	-	-	-	-	-	-	-	-	-	-	-
A1	1.0	-	-	-	-	-	140	-	92	52	-	113	187
A2	2.0	-	-	-	-	-	137	70	67	53	-	46	64
A3	0.0	-	-	-	-	-	155	63	70	73	-	123	74
A4	0.0	-	-	-	-	-	227	67	48	65	78	-	53
A5	0.0	-	-	-	-	-	42	70	72	88	162	-	64
Total Volatile Solids (TVS) unfiltered mg/L			**AVG SD n**	**301 485 25**		**MIN MAX**	**23 1380**						
Sample Location	Inlet height Inches above soil surface	mg/L 10/15/13	12/02/13	01/06/14	03/31/14	05/23/14	07/10/14	08/18/14	10/20/14	04/20/15	06/04/15	06/11/15	06/18/15
B1	1.5	-	-	-	-	-	-	-	-	-	-	-	-
A1	1.0	-	-	-	-	-	1230	-	37	101	-	116	190
A2	2.0	-	-	-	-	-	1320	-	84	98	-	57	57
A3	0.0	-	-	-	-	-	1380	-	58	36	-	37	37
A4	0.0	-	-	-	-	-	1270	-	48	77	77	-	23
A5	0.0	-	-	-	-	-	1010	-	38	76	47	-	23
Total Solids (TS) unfiltered mg/L			**AVG SD n**	**979 1598 25**		**MIN MAX**	**50 4250**						
Sample Location	Inlet height Inches above soil surface	mg/L 10/15/13	12/02/13	01/06/14	03/31/14	05/23/14	07/10/14	08/18/14	10/20/14	04/20/15	06/04/15	06/11/15	06/18/15
B1	1.5	-	-	-	-	-	-	-	-	-	-	-	-
A1	1.0	-	-	-	-	-	4106	-	133	233	-	370	376
A2	2.0	-	-	-	-	-	4093	-	146	561	-	203	420
A3	0.0	-	-	-	-	-	4157	-	137	140	-	140	100
A4	0.0	-	-	-	-	-	4250	-	96	139	140	-	50
A5	0.0	-	-	-	-	-	3895	-	116	242	160	-	63.3

Table 2.5-5. Summary of wet chemistry analyses of surface runoff samples.

Total Organic Carbon (TOC)			**AVG**	**18.1**		**MIN**	**2.0**						
unfiltered			**SD**	**10.1**		**MAX**	**56.2**						
mg/L			**n**	**29**									
	Inlet height												
	Inches above	mg/L											
Sample Location	soil surface	10/15/13	12/02/13	01/06/14	03/31/14	05/23/14	07/10/14	08/18/14	10/20/14	04/20/15	06/04/15	06/11/15	06/18/15
B1	1.5	-	-	-	-	-	-	-	-	-	-	-	-
A1	1.0	-	-	-	-	-	7.9	-	19.0	25.9	-	16.1	56.2
A2	2.0	-	-	-	-	-	5.3	16.9	17.4	18.9	-	21.9	18.4
A3	0.0	-	-	-	-	-	9.7	14.5	20.5	10.6	-	16.9	22.3
A4	0.0	-	-	-	-	-	8.3	16.6	29.6	27.1	30.5	-	19.3
A5	0.0	-	-	-	-	-	2.0	16.1	14.1	21.6	8.1	-	14.0

Perchlorate			**AVG**	**39.2**		**MIN**	**0.0**						
0.2 µm filtered sample			**SD**	**130.0**		**MAX**	**673.0**						
µg/L			**n**	**29**									
	Inlet height												
	Inches above	µg/L											
Sample Location	soil surface	10/15/13	12/02/13	01/06/14	03/31/14	05/23/14	07/10/14	08/18/14	10/20/14	04/20/15	06/04/15	06/11/15	06/18/15
B1	1.5	-	-	-	-	-	-	-	-	-	-	-	-
A1	1.0	-	-	-	-	-	0.0	-	0.5	0.4	-	122	81.5
A2	2.0	-	-	-	-	-	0.0	0.8	0.2	1.6	-	13	0.0
A3	0.0	-	-	-	-	-	0.0	0.4	0.5	1.4	-	673	7.4
A4	0.0	-	-	-	-	-	0.0	0.5	0.5	0.3	18.8	-	0.9
A5	0.0	-	-	-	-	-	1.1	1.2	0.6	0.8	207	-	2.4

Nitrate (as N)			**AVG**	**1.3**		**MIN**	**0.0**						
0.2 µm filtered			**SD**	**2.0**		**MAX**	**8.7**						
mg/L			**n**	**29**									
	Inlet height												
	Inches above	mg/L											
Sample Location	soil surface	10/15/13	12/02/13	01/06/14	03/31/14	05/23/14	07/10/14	08/18/14	10/20/14	04/20/15	06/04/15	06/11/15	06/18/15
B1	1.5	-	-	-	-	-	-	-	-	-	-	-	-
A1	1.0	-	-	-	-	-	0.0	-	0.8	0.1	-	6.0	8.7
A2	2.0	-	-	-	-	-	3.2	0.6	0.1	0.7	-	0.2	0.0
A3	0.0	-	-	-	-	-	0.1	0.6	0.7	0.1	-	1.0	0.0
A4	0.0	-	-	-	-	-	2.1	0.3	0.2	2.9	0.5	-	0.2
A5	0.0	-	-	-	-	-	0.5	0.1	1.2	3.5	1.9	-	0.0

Sulfate			**AVG**	**8.4**		**MIN**	**1.8**						
0.2 µm filtered			**SD**	**6.9**		**MAX**	**26.5**						
mg/L			**n**	**29**									
	Inlet height												
	Inches above	mg/L											
Sample Location	soil surface	10/15/13	12/02/13	01/06/14	03/31/14	05/23/14	07/10/14	08/18/14	10/20/14	04/20/15	06/04/15	06/11/15	06/18/15
B1	1.5	-	-	-	-	-	-	-	-	-	-	-	-
A1	1.0	-	-	-	-	-	13.5	-	9.1	4.8	-	10.5	7.5
A2	2.0	-	-	-	-	-	11.5	3.0	2.5	7.0	-	4.0	2.9
A3	0.0	-	-	-	-	-	16.5	4.9	6.1	8.5	-	26.5	5.8
A4	0.0	-	-	-	-	-	25.8	4.0	4.0	4.3	2.5	-	1.8
A5	0.0	-	-	-	-	-	4.48	4.6	10.9	6.2	24.3	-	6.8

Table 2.5-5. (cont.)

		Aqueous (µg/L)		
		Unfiltered	< 2.7 µm	< 0.45 µm
RDX				
	AVG	3.2	2.7	3.0
	SD	3.1	2.6	3.0
	n	20	19	19
	MIN	0.1	0.2	0.2
	MAX	11.2	8.7	10.3
	Unfiltered:Filtered ratio			
	AVG	1.49		
	SD	1.63		
	n	20		
	MIN	0.39		
	MAX	6.75		
HMX				
	AVG	3.5	2.8	2.7
	SD	3.1	3.0	2.8
	n	15	21	20
	MIN	0.4	0.2	0.3
	MAX	11.1	12.1	11.9
	Unfiltered:Filtered ratio			
	AVG	1.46		
	SD	0.83		
	n	15		
	MIN	0.58		
	MAX	3.37		
Perchlorate				
	AVG	39.2	ND	ND
	SD	130.0	ND	ND
	n	29	ND	ND
	MIN	0.2	ND	ND
	MAX	673.0	ND	ND
ND, not determined				

Table 2.5-6. Summary statistics for energetic compound detections in surface runoff samples.

3.0 CONCLUSIONS AND IMPLICATIONS FOR FUTURE RESEARCH

Laboratory experiments have simulated the likely processes that allow distribution of Comp B detonation residues on testing and training ranges. Macroscale residues (>0.5 cm) were shown to breakdown under realistic simulated precipitation, producing a flush of microscale particles (mean particle diameter ~10 μm), followed by a sustained release of particulates. The particulate mass released from Comp B residues averaged around 20% of the total explosives mass released during precipitation-driven weathering.

Microscale particles (20-45 μm diameter) of Comp B applied to the surface of sand columns were shown to migrate into the sand farther than mm-sized Comp B particles upon application of artificial rainwater. The migration of the microscale Comp B resulted in a larger effective contact time with the infiltrating rainwater, and increased dissolved concentrations of explosives in the column effluent when compared to the mm-sized particles.

When examined in flow-through dissolution chambers that did not allow for particle movement, the inherent mass transfer coefficients for microscale and mm-sized Comp B particles were similar on a surface area normalized basis, indicating that previous determination of mass transfer coefficients for a range of energetic compounds should be scalable. However, an inverse relationship was observed between the Comp B particle diameter and the RDX:TNT mass transfer rate coefficient ratio for dry-attritted particles, which suggests that RDX may be more readily dissolved (relative to TNT) in microscale particles compared to macroscale particles. Additionally, microscale Comp B particles that were produced by aqueous weathering exhibited mass transfer coefficients that were up to 20-fold higher than dry-attritted particles, indicating that once the inherent low-wettability (e.g., hydrophobicity) of Comp B particles is overcome, more rapid dissolution is possible. This may be of special concern in wet areas of ranges (e.g., marshes, swales, ditches).

This research has demonstrated that microscale particulates can be generated from larger Comp B detonation residues. These microscale particles can migrate into the soil profile, thereby increasing their contact with infiltrating rainwater, and giving rise to elevated dissolved explosives concentrations. While the surface area normalized mass transfer coefficients are comparable between microscale and mm-sized Comp B residues, there are indications that the mass transfer coefficient ratios for the components of Comp B vary with particle size. The environment and manner in which particles form (e.g., dry vs. wet attrition) also needs to be taken into consideration. This information should lead to better modeling of energetic compound fate and transport on testing and training ranges.

Finally, field sampling at an active DoD facility has confirmed that explosives are being transported in surface runoff from an area where explosives are being detonated. The presence

of actual microscale particulates in the surface runoff was not able to be confirmed due to the limited scope and type of sampling procedures employed. In addition to low, but measurable concentrations of HMX and RDX, multiple detections of perchlorate were also observed (some at the 100's of μg/L concentration level). These data clearly demonstrated the potential for horizontal distribution of explosives and other energetics by precipitation, which could lead to exposures of receiving bodies.

While this project has expanded the knowledge base concerning a basic understanding of microscale explosives generation and transport, further research is warranted in several areas, including:

1) To what degree are microscale particulates generated during detonations, and what is the loading rates of these particles on ranges?

2) How are these microscale explosives distributed in detonation plumes?

3) Can the presence of microscale particulates be documented in surface runoff from ranges, and what percentage of the total explosives mass in surface runoff do these particulates represent?

4) Is there a relationship between explosives loading in surface runoff and precipitation intensity?

4.0 REFERENCES CITED

1. **Abramoff, M. D., P. J. Magelhaes, and S. J. Ram**. 2004. Image processing with ImageJ. Biophotonics International **11:** 36-42.
2. **Bent, G. C., J. R. Gray, K. P. Smith, and G. D. Glysson**. 2001. A synopsis of technical issues for monitoring sediment in highway and urban runoff. U.S. Geological Survey / U.S. Department of the Interior. Report# Open-File Report 00-497.
3. **Borin, M., and E. Bigon**. 2002. Abatement of NO_3-N concentration in agricultural waters by narrow buffer strips. Environmental Pollution **117(1):** 165-168.
4. **Borst, M., and A. Selvakumar**. 2003. Particle-associated microorganims in stormwater runoff. Water Research **37(1):** 215-223.
5. **Cristescu, R. H., K. Goethals, P. B. Banks, F. N. Carrick, and C. Frère**. 2012. Experimental evaluation of koala scat persistence and detectability with implications for pellet-based fauna census. International Journal of Zoology **2012:** 12.
6. **Cussler, E. L.** 1984. Diffusion - mass transfer in fluid systems. Cambridge University Press, Cambridge, United Kingdom.
7. **Darnault, C. J. G., T. S. Steenhuis, P. Garnier, Y.-J. Kim, M. B. Jenkins, W. C. Ghiorse, P. C. Baveye, and J. Y. Parlange**. 2004. Preferential flow and transport of *Cryptosporidium parvum* oocysts through the vadose zone: Experiments and modeling. Vadose Zone J **3(1):** 262-270.
8. **Davis, A. P., M. Shokouhian, and S. Ni**. 2001. Loading estimates of lead, copper, cadmium, and zinc in urban runoff from specific sources. Chemosphere **44(5):** 997-1009.
9. **de Jonge, L. W., C. Kjaergaard, and P. Moldrup**. 2004. Colloids and colloid-facilitated transport of contaminants in soils: An introduction. Vadose Zone J **3(2):** 321-325.
10. **de Jonge, L. W., P. Moldrup, G. H. Rubæk, K. Schelde, and J. Djurhuus**. 2004. Particle leaching and particle-facilitated transport of phosphorus at field scale. Vadose Zone J. **3(2):** 462-470.
11. **Dickinson, C. H., V. S. H. Underhay, and V. Ross**. 1981. Effect of season, soil fauna and water content on the decomposition of cattle dung pats. New Phytologist **88(1):** 129-141.
12. **Dontsova, K., J. Šimůnek, J. Pennington, and C. Price**. 2007. Facilitated transport of high explosives in mineral soils. The ASA-CSSA-SSSA International Annual Meetings. New Orleans, LA, USA, November 4-8.
13. **Dontsova, K. M., S. L. Yost, J. Šimunek, J. C. Pennington, and C. W. Williford**. 2006. Dissolution and transport of TNT, RDX, and Composition B in saturated soil columns. Journal Of Environmental Quality **35:** 2043-2054.

14. **Fuller, M. E., C. E. Schaefer, C. Andaya, and S. Fallis**. 2014. Transport and dissolution of particulate Composition B through porous media. Chemosphere **107:** 400–406.
15. **Fuller, M. E., C. E. Schaefer, C. Andaya, V. Lazouskaya, S. Fallis, C. Wang, and Y. Jin**. 2012. Dissolution kinetics of sub-millimeter Composition B detonation residues: Role of particle size and surface wetting. Chemosphere **88(5):** 591-597.
16. **Furey, J. S., H. L. Fredrickson, M. J. Richmond, and M. Michel**. 2008. Effective elution of RDX and TNT from particles of Comp B in surface soil. Chemosphere **70(7):** 1175-1181.
17. **Gagliardi, J. V., and J. S. Karns**. 2000. Leaching of *Escherichia coli* O157:H7 in diverse soils under various agricultural management practices. Applied and Environmental Microbiology **66(9):** 4172-.
18. **Garn, H. S.** July 2002. Effects of lawn fertilizer on nutrient concentration in runoff from lakeshore lawns, Luaderdale Lakes, Wisconsin. U.S. Department of the Interior / U.S. Geological Survey. Report# USGS Water-Resources Investigations Report 02-4130.
19. **Hook, P. B.** 2003. Sediment retention in rangeland riparian buffers. Journal of Environmental Quality **32(3):** 1130-1137.
20. **Hunter, R. J.** 1981. Zeta Potential in Colloid Science: Principles and Applications. Academic Press, London, UK.
21. **Joly, L., C. Ybert, E. Trizac, and L. Bocquet**. 2004. Hydrodynamics within the electric double layer on slipping surfaces. Physical Review Letters **93(25):** 257805.
22. **Keck, D., D. Kircher, and P. Muff**. 2005. Technical Application Note : Simulation of rainfall with nozzles by means of radar reflectivity; Lechler GmbH. Lechler GmbH.
23. **Lægdsmand, M., K. G. Villholth, M. Ullum, and K. H. Jensen**. 1999. Processes of colloid mobilization and transport in macroporous soil monoliths. Geoderma **93(1–2):** 33-59.
24. **Lead, J. R., and K. J. Wilkinson**. 2006. Aquatic colloids and nanoparticles: Current knowledge and future trends. Environmental Chemistry **3(3):** 159-171.
25. **Lever, J. H., S. Taylor, L. Perovich, K. Bjella, and B. Packer**. 2005. Dissolution of Composition B detonation residuals. Environmental Science & Technology **39(22):** 8803-8811.
26. **Lewis, J., R. Martel, L. Trepanier, G. Ampleman, and S. Thiboutot**. 2009. Quantifying the transport of energetic materials in unsaturated sediments from cracked unexploded ordnance. Journal Of Environmental Quality **38(6):** 2229-2236.
27. **Lynch, J. C., J. M. Brannon, and J. J. Delfino**. 2002. Dissolution rates of three high explosive compounds: TNT, RDX, HMX. Chemosphere **47(7):** 725-734.
28. **Lynch, J. C., J. M. Brannon, and J. J. Delfino**. 2002. Effects of component interactions on the aqueous solubilities and dissolution rates of the explosive

formulations octol, composition B, and LX-14. Journal Of Chemical And Engineering Data **47(3):** 542-549.

29. **Lynch, J. C., J. M. Brannon, K. Hatfield, and J. J. Delfino**. 2003. An exploratory approach to modeling explosive compound persistence and flux using dissolution kinetics. Journal Of Contaminant Hydrology **66(3/4):** 147-159.
30. **Marinkas, P. L.** August 1975. Luminescence Properties of RDX and HMX. Picatinny Arsenal. Report# DTIC: ADA015538.
31. **McGee, E. A., D. D. Vohman, S. A. White, and T. L. Thompson**. 1999. Rapid method for fine grinding soils for organic nitrogen and ^{15}Nitrogen analysis. Communications in Soil Science and Plant Analysis **30(3-4):** 419-426.
32. **Meaney, M. S., and V. L. McGuffin**. 2008. Investigation of common fluorophores for the detection of nitrated explosives by fluorescence quenching. Analytica Chimica Acta **610(1):** 57-67.
33. **Monteil-Rivera, F., S. Deschamps, G. Ampleman, S. Thiboutot, and J. Hawari**. 2010. Dissolution of a new explosive formulation containing TNT and HMX: Comparison with octol. Journal Of Hazardous Materials **174(1-3):** 281-288.
34. **Morley, M. C., H. Yamamoto, G. E. Gerald E. Speitel, Jr., and J. Clausen**. 2006. Dissolution kinetics of high explosives particles in a saturated sandy soil. Journal Of Contaminant Hydrology **85(3-4):** 141-158.
35. **Muirhead, R. W., R. P. Collins, and P. J. Bremer**. 2006. Interaction of *Escherichia coli* and soil particles in runoff. Applied and Environmental Microbiology **72(5):** 3406-3411.
36. **Pantea, D., S. Brochu, S. Thiboutot, G. Ampleman, and G. Scholz**. 2006. A morphological investigation of soot produced by the detonation of munitions. Chemosphere **65(5):** 821-31.
37. **Perkin-Elmer**. Perkin-Elmer volocity user guide; http://www.cellularimaging.com/pdfs/manuals /VolocityUserGuide.pdf.
38. **Phelan, J. M., S. W. Webb, J. V. Romero, J. L. Barnett, F. Griffin, and M. Eliassi**. January 2003. Measurement and modeling of energetic material mass transfer to soil pore water – Project CP-1227 Annual Technical Report Sandia National Laboratories. Report# SAND2003-0153.
39. **Phifer, C. C., R. L. Schmitt, L. R. Thorne, P. Hargis, Jr.,, and J. E. Parmeter**. October 2006. Studies of the laser-induced fluorescence of explosives and explosive compositions. Sandia National Laboratories. Report# SAND2006-6697.
40. **Pitt, R., R. Field, M. Lalor, and M. Brown**. 1995. Urban stormwater toxic pollutants: Assessment, sources, and treatability. Water Environment Research **67(3):** 260-275.
41. **Pontier, H., J. R. Williams, and E. May**. 2004. Progressive changes in water and sediment quality in a wetland system for control of highway runoff. Science of the Total Environment **319(1-3):** 215-224.

42. **Potter, T. L., C. C. Truman, D. D. SBosch, and C. W. Bednarz**. 2003. Cotton defliant runoff as a function of active ingrediaent and tillage. Journal of Environmental Quality **32(6):** 2180-2188.
43. **Powelson, D. K., and A. L. Mills**. 2001. Transport of *Escherichia coli* in sand columns with constant and changing water contents. Journal of Environmental Quality **30(1):** 238-245.
44. **Russo, A. E., M. Narter, and M. L. Brusseau**. 2009. Characterizing pore-scale dissolution of organic immiscible liquid in a poorly-sorted natural porous medium. Environmental Science and Technology **43(15):** 5671-5678.
45. **Schnaar, G., and M. L. Brusseau**. 2006. Characterizing pore-scale dissolution of organic immiscible liquid in natural porous media using synchrotron X-ray microtomography. Environmental Science and Technology **40(21):** 6622-6629.
46. **Sen, T. K., and K. C. Khilar**. 2006. Review on subsurface colloids and colloid-associated contaminant transport in saturated porous media. Advances in Colloid and Interface Science **119(2-3):** 71-96.
47. **SERDP/ESTCP**. 2007. SERDP and ESTCP Technical Exchange Meeting on DoD Operational Range Assessment and Management Approaches. http://www.serdp.org/content/download/8237/101218/version/1/file/RAWorkshopRDTENeedsRpt.pdf.
48. **Tate, K. W., M. D. Pereira, and E. R. Atwill**. 2004. Efficacy of vegetated buffer strips for retaining *Cryptosporidium parvum*. Journal of Environmental Quality **33(6):** 2243-51.
49. **Taylor, S., E. Campbell, L. Perovich, J. Lever, and J. Pennington**. 2006. Characteristics of Composition B particles from blow-in-place detonations. Chemosphere **65(8):** 1405-13.
50. **Taylor, S., A. Hewitt, J. Lever, C. Hayes, L. Perovich, P. Thorne, and C. Daghlian**. 2004. TNT particle size distributions from detonated 155-mm howitzer rounds. Chemosphere **55(3):** 357-367.
51. **Taylor, S., J. H. Lever, J. Fadden, N. Perron, and B. Packer**. 2009. Outdoor weathering and dissolution of TNT and Tritonal Chemosphere **77(10):** 1338-1345
52. **Taylor, S., J. H. Lever, J. Fadden, N. Perron, and B. Packer**. 2009. Simulated rainfall-driven dissolution of TNT, Tritonal, Comp B and Octol particles. Chemosphere **75(8):** 1074-1081.
53. **Trask, J. R., P. K. Kalita, M. S. Kuhlenschmidt, R. D. Smith, and T. L. Funk**. 2004. Overland and near-surface transport of *Cryptosporidium parvum* from vegetated and nonvegetated surfaces. Journal of Environmental Quality **33(3):** 984-93.
54. **Vellidis, G., R. Lowrance, P. Gay, and R. D. Wauchope**. 2002. Herbicide transport in a restored riparian forest buffer system. Transactions of The ASAE **45(1):** 89-97.

55. **Walsh, M. E., S. Taylor, A. D. Hewitt, M. R. Walsh, C. A. Ramsey, and C. M. Collins**. 2010. Field observations of the persistence of Comp B explosives residues in a salt marsh impact area. Chemosphere **78(4):** 467-473.
56. **Wang, C., M. E. Fuller, V. Lazouskaya, J. Caplan, C. E. Schaefer, and Y. Jin**. 2011. Dissolution of microscale energetic residues in saturated porous media: Visualization and quantification at the pore-scale by spectral confocal microscopy. Environmental Science and Technology **49(19):** 8352–8358.
57. **Wang, C., M. E. Fuller, C. E. Schaefer, D. Fu, and Y. Jin**. 2012. Modeling the dissolution of various types of mixed energetic residues under different flow conditions. Journal Of Hazardous Materials **235-236:** 138-143.
58. **Webb, S. W., J. M. Phelan, T. Hadgu, J. S. Stein, and C. M. Sallaberry**. 2006. Measurement and Modeling of Energetic-Material Mass Transfer to Soil-Pore Water Sandia National Laboratories: Albuquerque, New Mexico and Livermore, California, USA. Report# for SERDP Project CP-1227 (https://www.serdp-estcp.org/content/download/4496/66564/file/CP-1227-FR.pdf).
59. **Wu, Q., G. Riise, and R. Kretzschmar**. 2003. Size distribution of organic matter and associated propiconazole in agricultural runoff material. Journal of Environmental Quality **32(6):** 2200-2206.
60. **Xu, W., K. E. Dana, and W. A. Mitch**. 2010. Black carbon-mediated destruction of nitroglycerin and RDX by hydrogen sulfide. Environmental Science & Technology **44(16):** 6409-6415.
61. **Zeiss**. Zeiss online tutorial - spectral imaging with linear unmixing; http://zeiss-campus.magnet.fsu.edu/tutorials/spectralimaging/linearunmixing/index.html.
62. **Zeiss**. Zeiss online tutorial - introduction to spectral imaging and linear unmixing; http://zeiss-campus.magnet.fsu.edu/articles/spectralimaging/introduction.html.
63. **Zimmermann, T., J. Rietdorf, and R. Pepperkok**. 2003. Spectral imaging and its applications in live cell microscopy. FEBS Letters **546(1):** 87-92.

5.0 APPENDICES

A. Other Supporting Data – N/A

B. List of Scientific/Technical Publications

Articles in peer-reviewed journals

1. **Fuller, M. E., C. E. Schaefer, C. Andaya, and S. Fallis**. 2015. Production of particulate Composition B during simulated weathering of larger detonation residues. Journal of Hazardous Materials **283:** 1-6.
2. **Fuller, M. E., C. E. Schaefer, C. Andaya, and S. Fallis**. 2014. Transport and dissolution of particulate Composition B through porous media. Chemosphere **107:** 400-406.
3. **Wang, C., M. E. Fuller, C. E. Schaefer, J. Caplan, and Y. Jin**. 2012. Dissolution of explosive compounds TNT, RDX, and HMX under continuous flow conditions. Journal of Hazardous Materials **217-218:** :187–193.
4. **Wang, C., M. E. Fuller, C. E. Schaefer, D. Fu, and Y. Jin**. 2012. Modeling the dissolution of various types of mixed energetic residues under different flow conditions. Journal of Hazardous Materials **235-236:** 138-143.
5. **Fuller, M. E., C. E. Schaefer, C. Andaya, V. Lazouskaya, S. Fallis, C. Wang, and Y. Jin**. 2012. Dissolution kinetics of sub-millimeter Composition B detonation residues: Role of particle size and surface wetting. Chemosphere **88(5):** 591-597.
6. **Wang, C., M. E. Fuller, V. Lazouskaya, J. Caplan, C. E. Schaefer, and Y. Jin**. 2011. Dissolution of microscale energetic residues in saturated porous media: Visualization and quantification at the pore-scale by spectral confocal microscopy. Environmental Science and Technology **49(19):** 8352–8358.

Conference or symposium abstracts

1. **Fuller, M. E., C. E. Schaefer, C. Andaya, and S. Fallis**. 2015. Production, Fate and Transport of Microscale Energetic Residues. Third International Symposium on Bioremediation and Sustainable Environmental Technologies. Miami, FL., USA, May 18-21.
2. **Fuller, M. E., C. E. Schaefer, C. Andaya, Y. Jin, C. Wang, and S. Fallis**. 2012. Occurrence and Fate of Energetic Residues on Training Ranges. The 2010 Partners in Environmental Technology Technical Symposium & Workshop. Washington, D.C., USA, December 1-3.
3. **Fuller, M. E., C. E. Schaefer, Y. Jin, C. Wang, S. Fallis, and J. Šimůnek**. 2011. Fate and Transport of Colloidal Energetic Residues. The 2010 Partners in Environmental Technology Technical Symposium & Workshop. Washington, D.C., USA, December 1-3.
4. **Wang, C., M. E. Fuller, V. Lazouskaya, C. Schaefer, J. L. Caplan, and Y. Jin**. 2011. Measure and Model the Dissolution of Explosive Compounds TNT, RDX, and HMX under Continuous Flow Conditions. ASA-CSSA-SSSA International Annual Meeting. San Antonio, TX, USA, October 16-19.

5. **Lazouskaya, V., C. Wang, M. Fuller, and Y. Jin**. 2010. Energetic colloids: generation, dissolution, and transport properties. 1st International Conference and Exploratory Workshop on Soil Architecture and Physico-Chemical Functions. Research Centre Foulum, Denmark, November 30 - December 3.

8. **Wang, C., V. Lazouskaya, M. E. Fuller, J. Caplan, K. Czymmek, C. Shen, and Y. Jin**. 2010. Retention and Dissolution of Small Energetic Residues in Porous Media: Pore-Scale Observation by Spectral Confocal Microscopy. 84th Colloid and Surface Science Symposium. Akron, OH, USA, June 20-23.

7. **Fuller, M. E., C. E. Schaefer, V. Lazouskaya, Y. Jin, and S. Fallis**. 2010. Fate and Transport of Colloidal Energetic Residues. Seventh International Conference on Remediation of Chlorinated and Recalcitrant Compounds. Monterey, CA, USA, May 24-27.

8. **Fuller, M. E., C. E. Schaefer, V. Lazouskaya, Y. Jin, C. Wang, S. Fallis, and J. Šimůnek**. 2010. Fate and Transport of Colloidal Energetic Residues. The 2010 Partners in Environmental Technology Technical Symposium & Workshop. Washington, D.C., USA, December 1-3.

9. **Fuller, M. E., C. E. Schaefer, V. Lazouskaya, and Y. Jin**. 2009. Fate and Transport of Colloidal Energetic Residues. The 2009 Partners in Environmental Technology Technical Symposium & Workshop. Washington, D.C., USA, December 1-3.